2022

Robot Assisted Shoulder Rehabilitation: Biomechanical Modelling, Design and Performance Evaluation

Aibek Niyetkaliyev

Robot Assisted Shoulder Rehabilitation: Biomechanical Modelling, Design and Performance Evaluation

Aibek Niyetkaliyev

Supervisors:
Prof. Gursel Alici
Dr. Emre Sariyildiz

This thesis is presented as part of the requirement for the conferral of the degree:
Doctor of Philosophy

University of Wollongong

School of Mechanical, Materials, Mechatronic and Biomedical Engineering

April 2022

Abstract

The upper limb rehabilitation robots have made it possible to improve the motor recovery in stroke survivors while reducing the burden on physical therapists. Compared to manual arm training, robot-supported training can be more intensive, of longer duration, repetitive and task-oriented. To be aligned with the most biomechanically complex joint of human body, the shoulder, specific considerations have to be made in the design of robotic shoulder exoskeletons. It is important to assist all shoulder degrees-of-freedom (DOFs) when implementing robotic exoskeletons for rehabilitation purposes to increase the range of motion (ROM) and avoid any joint axes misalignments between the robot and human's shoulder that cause undesirable interaction forces and discomfort to the user.

The main objective of this work is to design a safe and a robotic exoskeleton for shoulder rehabilitation with physiologically correct movements, lightweight modules, self-alignment characteristics and large workspace. To achieve this goal a comprehensive review of the existing shoulder rehabilitation exoskeletons is conducted first to outline their main advantages and disadvantages, drawbacks and limitations. The research has then focused on biomechanics of the human shoulder which is studied in detail using robotic analysis techniques, i.e. the human shoulder is modelled as a mechanism. The coupled constrained structure of the robotic exoskeleton connected to a human shoulder is considered as a hybrid human-robot mechanism to solve the problem of joint axes misalignments. Finally, a real-scale prototype of the robotic shoulder rehabilitation exoskeleton was built to test its operation and its ability for shoulder rehabilitation.

Acknowledgments

Firstly, I would like to sincerely thank and acknowledge my principal supervisor, Prof. Gursel Alici, for giving me an opportunity to do this research, for his support, encouragement, and continual guidance throughout my PhD candidature.

I also want to thank my co-supervisor, Dr. Emre Sariyildiz, for the valuable constructive feedback and concern, his time and help. I want to thank electric and machine workshop technicians, Douglas Henness and Christopher Wood, for their time and assistance in manufacturing and assembling the developed robotic prototype. I extend my gratitude to Dr. Tanju Yildirim for his help with the experimental trials. I also want to thank Dr. Shahid Hussain with whom I started this research journey.

Finally, I am very grateful for the encouragement and understandings from my family members, my wife and kids, my parents, which were translated into the strength and energy that I needed during my doctoral studies. This thesis was written during an uneasy time that our world has faced due to the unexpected global pandemic that took many lives around the globe and changed the way we live and work. Let me wish all of us to stay well and healthy.

Certification

I, Aibek Niyetkaliyev, declare that this thesis submitted in fulfilment of the requirements for the conferral of the degree Doctor of Philosophy, from the University of Wollongong, is wholly my own work unless otherwise referenced or acknowledged. This document has not been submitted for qualifications at any other academic institution.

Aibek Niyetkaliyev
April 2022

List of Names or Abbreviations

DOF	Degree Of Freedom
ROM	Range Of Motion
ADL	Activities of Daily Living
CAD	Computer Aided Drawing
3D	Three Dimensional
HRM	Human-Robot-Mechanism
SRE	Shoulder Rehabilitation Exoskeleton
CDPM	Cable-Driven Parallel Mechanism
cPM	Constrained Parallel Manipulator
ISB	International Society of Biomechanics
UL	Upper Limb
SG	Shoulder Girdle
GH	Glenohumeral (shoulder joint)
CGH	Center of Glenohumeral joint
ST	Scapulothoracic joint (shoulder girdle joint)
SC	Sternoclavicular joint (shoulder girdle joint)
AC	Acromioclavicular joint (shoulder girdle joint)
HH	Humeral Head
SH	Scapulohumeral rhythm
F/E	Flexion/Extension (shoulder joint movements)
A/A	Abduction/Adduction (shoulder joint movements)
IR/ER	Internal/External Rotation (shoulder joint movements)
E/D	Elevation/Depression (shoulder girdle movements)
P/R	Protraction/Retraction (shoulder girdle movements)
PAM	Pneumatic Artificial Muscles

SEA	Series Elastic Actuation
FK	Forward Kinematics
IK	Inverse Kinematics
ID	Inverse Dynamics
CS	Coordinate System
SGM	Shoulder Girdle Module
L	Link
S	Spherical joint
U	Universal joint
UPS	universal-prismatic-spherical
E	End-effector point
$\mathbf{R}_1^0$	Rotation matrix of frame CS_1 w.r.t frame CS_0
$\mathbf{J}$	Jacobian matrix
$\boldsymbol{q}$	Joint space vector
BP	Base platform
MP	Moving platform
m	Number of cables
n	Number of DOFs
l	Cable length
TF	Tension Factor
LP	Linear Program
PID	Proportional-Integral-Derivative
PC	Position Control
PIC	Position-based Impedance Control
IMU	Inertial Measurement Unit
AAN	Assist-As-Needed

Table of Contents

List of Tables, Figures and Illustrations

Chapter 1

Introduction

1.1 Motivation

Stroke is the leading cause of disability in the United States [1] and a high prevalence of stroke has been estimated and reported in the Australian population. There were more than 475,000 people in Australia [2] with the effects of stroke in 2017 and this is predicted to increase to 1 million by 2050. In 2020, the total financial costs of stroke in Australia have exceed $6.2 billion [3]. The weakness and loss of upper limb motor control is a common neurological impairment arising from stroke with up to 77.4% [4] of stroke patients suffering from upper limb disability, which makes it the most common stroke-induced impairment. This condition must be treated by regular sessions with a dedicated physical therapist in order to regain motor function. These exhausting and laborious conventional physical therapies are initiated in clinics to maximize potential for motor recovery [5-6]. However, the use of therapists who can only work with a limited number of patients is expensive, in high demand, and requires frequent visits to a rehabilitation clinic. Moreover, the quality of manually assisted training is dependent on therapist's experience and judgment which varies widely amongst therapists resulting in inconsistency in treatment and therapeutic subjectivity. In addition, the conventional training sessions are short due to physical therapist's fatigue and economic burdens, and do not have precise quantification of patient's sensorimotor performance during exercises. Automated rehabilitation solutions are researched lately to overcome above mentioned shortcomings of manual physical therapy.

Recent developments in technology enabled robotic devices to assist stroke patients with upper limb disabilities. These robotic devices can provide task oriented, prolonged, accessible, repetitive and intensive physical therapy [7-10]. With the use of robots in rehabilitation clinics, physical efforts and involvement of therapists become less intensive. As the robotic devices are equipped with various sensors, an extensive data related to the therapy can also be obtained and processed for further evaluation. Therefore, these upper limb rehabilitation robots have made it possible to improve the motor recovery in stroke survivors while reducing the burden on physical therapists.

Upper limb rehabilitation robots [11-17] can be divided into two types: *exoskeletons* or orthotic systems where the robot's joints are designed to correspond with the human joints and *end-effector based* devices that are connected to the arm segment at one point with the axes that are usually not aligned with the joints of the subject. The robotic exoskeleton is an outer mechanism attached to the human arm at multiple connection points to operate parallel to the human movement. The exoskeletons are more advanced robots as they assist not only the end-effector of the human limb but also provide single-joint robotic assistance during the arm motion, so they are more functional and specially designed to subject's needs. Therefore, such a robotic device can provide independent joint control tailoring to specific tasks. As there is a close physical interaction between the human and the robotic exoskeleton, the distinctive aspect of robotic design is that its kinematic chain must correspond to the human anatomical joints. In this regard, compared with end-effector based robots, exoskeletons are more complex in terms of mechanism design and actuation as well as control.

The main challenges are that such robotic exoskeletons should be accurately aligned with the human joints, safely adjusted to match different individuals' sizes and provide naturalistic complex arm movements. This is a challenging task to achieve for one of the most biomechanically complex parts of human body, i.e., the multi degree-of-freedom (DOF) human shoulder, which consists of the 3-DOFs *spherical shoulder joint* and the 2-DOFs inner part of the human shoulder, called the *shoulder girdle*. As the center of rotation of the spherical joint is floating during the integrated motion of the human shoulder, the *joint axes misalignments* that can occur between the robotic exoskeleton and human body will lead to undesirable interaction torques and painful discomfort to the user. This is usually the case when robotic shoulder exoskeletons take into consideration only three rotational shoulder DOFs. Therefore, it is important to also assist the shoulder girdle's DOFs to avoid unwanted interaction forces during the coupled shoulder motion, provide larger range of motion (ROM) and perform independent shoulder girdle motions to increase the effectiveness of the rehabilitation therapy.

Despite the rapid progress in robotic upper limb rehabilitation devices over the last decade, during which numerous groups of researchers have designed and built different robotic devices with various mechanical advancements for shoulder complex rehabilitation, still much remains to be done in this exciting area of research [18].

1.2 Research Questions

The main objective of this work is to design and develop a safe and lightweight, robotic exoskeleton for shoulder rehabilitation with physiologically correct movements, self-alignment characteristics and large workspace. This is a challenging task that requires a thorough knowledge of multi-disciplinary research fields. While design, actuation and control issues should be examined, more emphasis should be given to the mechanism design aspects of exoskeleton due its considerable importance since exoskeletons are meant to act in symbiosis with the human limbs.

Essentially, the shoulder exoskeleton should be accurately designed from a biomechanics point of view. Thus, prior to the mechanism design stage of the robotic shoulder rehabilitation exoskeletons, one of the most essential steps is to study the anatomy and biomechanics of the human shoulder. It is important to thoroughly study the movement characteristics of the shoulder, its external and internal configuration, determine the number of DOFs, structure of the bones and articulations, muscle functions and their points of attachments so that the robotic exoskeleton would be able to stimulate the natural movements of the shoulder complex. Therefore, the ergonomic design of the robotic exoskeleton should be enhanced by using biomechanical principles of human motion.

The kinematic parameters of the robotic shoulder exoskeleton have to be selected such that its workspace and ROM will match the motion of a user's shoulder while also avoiding collisions, mechanical interference between the links and parts of the human body, singular configurations and misalignments between the robot and human joint axes. In order to maintain the kinematic compatibility during the shoulder motions a developed robotic exoskeleton must comply with the complex anatomy of human shoulder. Kinematics plays a key role in shoulder exoskeletons. Since the human shoulder and robotic exoskeleton are not kinematically compatible, these misalignments will result in undesired interaction forces as both structures are connected to each other. The user should not experience any constraints to their natural arm motion pattern when the shoulder exoskeleton is superimposed on a human body. As the users present a wide variety of upper arm dimensions, it is important that the exoskeleton can also adapt to different arm sizes and take into consideration the whole weight of the human arm.

To accomplish primary research objectives of this thesis, the following main research questions have been considered:

- How can the analysis approaches developed for robotic manipulators be applied to the shoulder musculoskeletal system to have a greater understanding of its internal biomechanics? How can the human shoulder be modelled as a mechanism?
- Can the combined human-robot interactive structure be considered as a constrained robotic mechanism with a hybrid structure to solve the kinematic compatibility issue between the user and the robot joints? How can analysis techniques developed for constrained robotic mechanisms be applied to such coupled human-robot mechanisms?
- How to develop and build a safe, lightweight, actuated robotic shoulder rehabilitation exoskeleton capable of covering all shoulder DOFs and workspace without any joint axes (human-robot) misalignments, equip it with proper sensors and perform its experimental evaluation?

1.3 Contributions and Outcomes of the Thesis

Towards the development of robotic shoulder rehabilitation exoskeleton (**SRE**) and responding to the research questions, the main contributions made by this thesis are as follows:

- A comprehensive review of the existing shoulder rehabilitation exoskeletons was conducted. The detailed review covers the recent advancements in the mechanism design, control strategies and clinical studies. It outlines the advantages and disadvantages of major developments, limitations and current challenges in the field of robotic shoulder rehabilitation exoskeletons. This review resulted in a published journal paper [18].
- The human shoulder was considered as a mechanism where a 6-4 parallel mechanism was proposed to model the complex articulation of the human shoulder girdle. As a result, a methodology to model the shoulder kinematics with a minimum number of parameters is set forward to facilitate the shoulder

motion planning, provide additional perspectives on the study of shoulder motion. This methodology is beneficial for applications that require simulation of upper body motions, including examination of motion impairment and rehabilitation robotics. This methodology was published as a journal paper [19].

- In order to solve the kinematic compatibility problem of the human-robot interaction in shoulder rehabilitation exoskeletons, a novel bio-inspired 5-DOFs human-robot mechanism (*HRM*), based on constrained mechanism with hybrid structure, was proposed for the first time as an outcome of the present research. It combines serial and parallel manipulators with rigid and cable links enabling a match between human and exoskeleton joint axes, covering the whole range of motion of the human shoulder with the workspace free of singularities. The numerical and simulation results from CAD model of the mechanism and a fabricated 3D printed prototype were presented to validate the kinematic model and its overall advantages. This work resulted in a journal publication [20].
- An exoskeleton for shoulder rehabilitation, named HYBRID-SRE with a large workspace, reduced weight and self-alignment characteristics was developed. Its distinctive feature of matching the coupled motion of the human shoulder, including the shoulder girdle, and its hybrid mechanism design make it the first of its category. Compared to other existing shoulder exoskeletons, for the first time, the shoulder cuff of HYBRID-SRE is equipped with the force sensors and can be actuated to follow the shifts of the shoulder joint. The ability to cover the large workspace, close to the maximum reachable workspace of the healthy human shoulder, was experimentally evaluated with Xsens technology. Trajectory tracking experiments were conducted to evaluate the control hardware and software of the developed exoskeleton. The primary aspects of the proposed exoskeleton design were presented at the international conference [21].

The overall structure of HYBRID-SRE and a user wearing it at an initial pose are shown in Figure 1-1. The contributions of this thesis can be applied in the study of biomechanics and robotic exoskeletons.

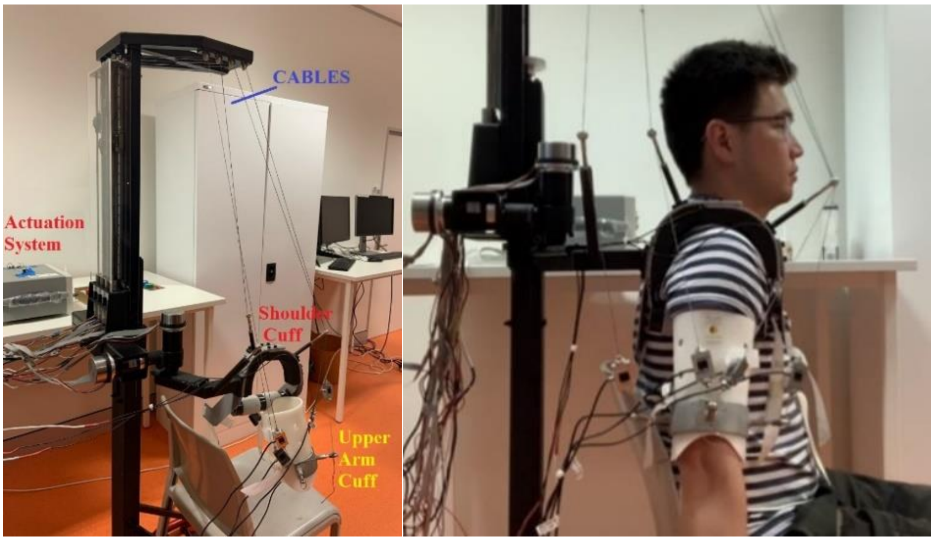

Figure 1-1: The overall structure of HYBRID-SRE exoskeleton with a user wearing it at its initial pose.

In the field of biomechanics, the proposed point-contact model between scapula bone and thorax can be adapted to improve the existing biomechanical shoulder models used in computer simulation, e.g. in AnyBody and/or OpenSim software.

In the field of robotic exoskeletons, the proposed hybrid *HRM* or its decoupled modules can also further be applied not only to the shoulder complex but to other multi-DOF human limbs as well. The human limbs should be regarded as the inner passive restrained links when analyzing such hybrid constrained anthropomorphic mechanisms. Moreover, this kind of *HRM*s can be built as test beds to experimentally evaluate the kinematic and dynamic characteristics of the designed rehabilitation exoskeletons during the prototype development stage. As the human limb is an integral part of the exoskeleton, it is a bio-inspired robotic mechanism. Therefore, the cable-driven parallel mechanism for the shoulder joint is selected, similar to the parallel actuation of the human muscles.

By adapting the 3-DOFs cable-driven module for the shoulder joint and placing all the actuators on the fixed support, the weight of the developed HYBRID-SRE is greatly reduced. The 2-DOF shoulder cuff mechanism equipped with force sensors can provide both actuated and passive motions to demonstrate its ability to follow the coupled movements of the human shoulder girdle. This is a highly important concern in robotic rehabilitation practices. The use of various sensors also made the whole experimental set up a measurement tool. The measured forces, ROM of the joints and Xsens data obtained during the experiments can be used for evaluation and comparison purposes. For instance, based on the Xsens data from the workspace evaluation trials, it can be claimed that the exoskeleton's workspace is sufficient to perform the shoulder motions related to the activities of daily living (*ADL*) and the physical rehabilitation therapies (e.g. after stroke).

It is worth mentioning here that the developed HYBRID-SRE went through the *Risk Assessment* approved by the University of Wollongong. Also, to experimentally evaluate the shoulder exoskeleton with healthy participants, a written informed consent was obtained from all participants, and an official *Ethical Approval* was obtained from the Human Research Ethics Committee, University of Wollongong.

1.4 Related Publications

The outcomes of this study have resulted in the following publications:

<u>Journal articles:</u>

- A. S. Niyetkaliyev, Shahid Hussain, Mergen H. Ghayesh, Gursel Alici, "Review on Design and Control Aspects of Robotic Shoulder Rehabilitation Orthoses", *IEEE Transactions on Human-Machine Systems*, vol. 47(6), pp.1134-1145, 2017 [18].
- A. S. Niyetkaliyev, S. Hussain, P. K. Jamwal, and G. Alici, "Modelling of the human shoulder girdle as a 6-4 parallel mechanism with a moving scapulothoracic joint", *Mechanism and Machine Theory*, vol. 118, pp. 219-230, 2017 [19].
- A. S. Niyetkaliyev, E. Sariyildiz, G. Alici, "Kinematic Modeling and Analysis of a Novel Bio-Inspired and Cable-Driven Hybrid Shoulder Mechanism", *ASME. J. Mechanisms Robotics. February 2021; 13(1): 011008.* [20].

<u>Conferences:</u>

- A. S. Niyetkaliyev, E. Sariyildiz, G. Alici, "A Hybrid Multi-Joint Robotic Shoulder Exoskeleton for Stroke Rehabilitation", *The IEEE/ASME International Conference on Advanced Intelligent Mechatronics* (AIM 2018), pp. 857–862. Auckland, New Zealand, July 2018 [21].
- A. S. Niyetkaliyev, E. Sariyildiz, G. Alici, "Avoiding Joint Axes Misalignments in Robotic Shoulder Rehabilitation Exoskeleton", *13th international*

Convention on Rehabilitation Engineering and Assistive Technology, 26-29 August, Canberra, Australia. 2019.

1.5 Structure of the Thesis

The thesis is organized as follows:

Chapter 1 – Introduction: As presented so far, this chapter reports on the motivation for this study, defines research framework and questions, lists the main research contributions and outcomes and provides an outline of the thesis.

Chapter 2 includes an introduction to the field of rehabilitation robots and presents a comprehensive review of the shoulder rehabilitation exoskeletons, mainly focusing on mechanism design, control aspects and experimental clinical trials.

Chapter 3 is concerned with the complex biomechanics of the human shoulder which is analyzed as a robotic mechanism. This chapter presents the proposed mechanism followed with a numerical case study.

Chapter 4 presents kinematic modelling of a novel bio-inspired and cable-driven hybrid shoulder mechanism, including singularity and workspace analyses combined with numerical simulations.

Chapter 5 presents an overview of the developed robotic shoulder exoskeleton, including the descriptions of its structural components, actuation systems and control hardware.

Chapter 6 reports on the performance evaluation of the developed exoskeleton, mainly containing experimental results for trajectory tracking, workspace evaluation and basic control trials.

Chapter 7 presents conclusions and recommendations for future research.

Chapter 2

Robotic Shoulder Exoskeletons

2.1 Introduction

This chapter presents the area of rehabilitation robots, briefly describes the structure of the human shoulder and provides the design, control and clinical trial aspects of existing robotic exoskeletons for shoulder rehabilitation, summarizing their limitations, and discussing research gaps and areas for future development. As the main objective of this work is to develop a robotic shoulder exoskeleton for rehabilitation after stroke, the scope of a comprehensive review of the shoulder rehabilitation devices presented in this chapter does not cover the passive robotic shoulder exoskeletons and the end-effector-based robotic devices developed for shoulder rehabilitation.

2.2 Robot Assisted Upper Limb Rehabilitation

As the intended use of HYBRID-SRE is for stroke rehabilitation, it is worth mentioning the main post-stroke stages classified in the literature [22]:

- *Acute phase*: less than 3 months post-stroke;
- *Sub-acute phase*: the period between 3 and 6 months post-stroke;
- *Chronic phase*: more than 6 months post-stroke up to 2 years, after which the recovery is usually slow and rehabilitation techniques become less effective.

The interaction between the patient and the rehabilitation robot during the therapy is referred as the interaction modalities, or *training modes*. The existing literature [23] usually categorizes them into three main modes: *passive, active*, and *assistive*. They are further divided into eight modalities:

- *Passive*: the robotic system implements the motion without any assistance from the patient;

- *Passive-mirrored (bilateral method)*: a bilateral configuration where the motion of the unaffected (healthy) limb is used as an input to guide the motion of the impaired limb;

- *Path-guidance*: the robot assists the motion along the desired trajectory by executing alterations when the motion is deviated;

- *Active*: the robot doesn't provide any forces upon the patient but works as a measurement device;

- *Active-assistive (triggered assistance)*: the robot assists the motion only when the patient is not capable to complete the task, switching to the passive mode;
- *Corrective*: the motion of the patient is stopped when the error of the deviation from the given task exceeds the defined threshold, switching to the active mode afterwards;
- *Resistive*: the resistive forces/torques are applied against the desired motion.
- *Assistive*: the voluntary movement of the patient is required during the motion. The robot can help the patient to perform the task by applying the needed forces.

The existing rehabilitation robotic devices used in clinical settings can provide one, more or a combination of the above listed training modes. It can depend on several factors: the recovery stage of the patient, the type of physical therapy practiced by the therapist, the control strategy of the exoskeleton, its structure, actuation system, etc. In fact, none of these training modalities seem as the most preferable as the choice of the suitable physical therapy largely depends on the therapist's recovery program and the patient progress, which varies greatly on the individual basis. Still, most of the rehabilitation robotic systems that are used in clinical settings implement active, active-assisted, passive and resistive modes [23]. Also, when analyzed based on the patient phases of recovery, the following trainings modalities demonstrated better results during rehabilitation therapies [24]:

- Acute patients: active, assistive, active-assistive and passive modes.
- Chronic patients: passive-mirrored, resistive and path guidance modes.

2.3 Human Shoulder

The description of the human shoulder is briefly presented in this section to introduce the main anatomical and biomechanical terms of the shoulder complex. The knowledge of the shoulder structure and movement characteristics is an essential step towards the development of robotic shoulder rehabilitation devices.

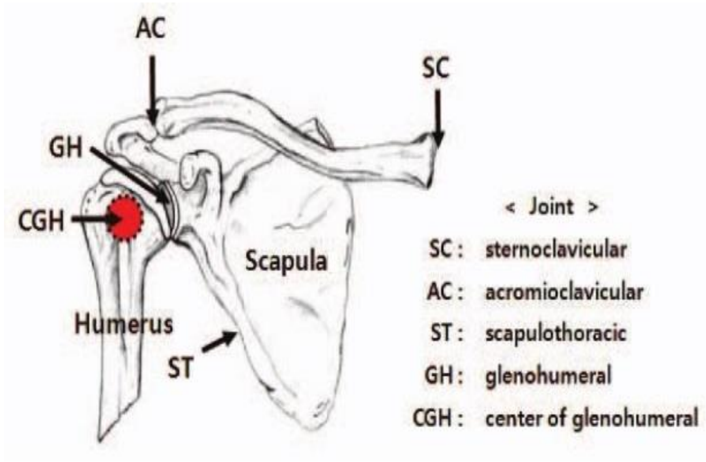

Figure 2-1: Structure of shoulder complex [25].

The human shoulder shown in Figure 2-1 is an integrated complex with three bones (clavicle, scapula and humerus) and four independent joints. The sternoclavicular (SC) joint connects the clavicle to the thorax, the acromioclavicular (AC) joint connects the scapula to the clavicle, the scapulothoracic (ST) articulation describes scapula motion over the thorax and the glenohumeral (GH) joint, also referred as shoulder joint, connects the humerus to the scapula. The former three joints compose the closed-kinematic chain called shoulder girdle. The GH joint is commonly oversimplified as a “ball and socket type” joint with three DOFs. It is formed by the “socket” of the female part of the scapula, also called glenoid cavity, and the upper part of the humerus, named humeral head (HH).

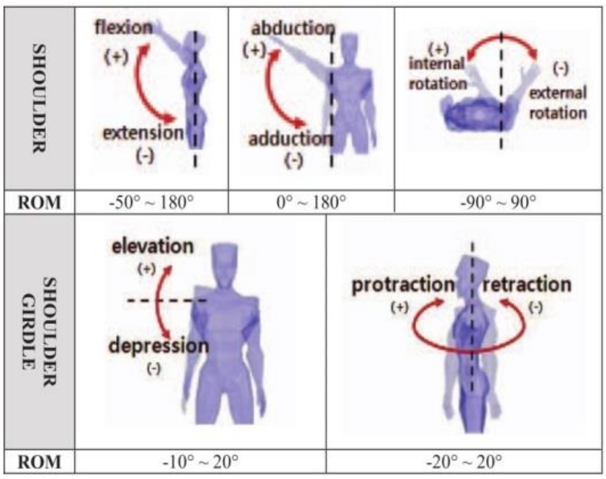

Figure 2-2: Movements of shoulder complex [25].

The three rotational movements of the shoulder, shown in the upper part of Figure 2-2, can be described with the following terms: flexion/extension (F/E), abduction/adduction (A/A) and internal/external rotation (IR/ER). The shoulder girdle’s motion has 4-DOFs overall but is generally described by two translational movements [25] as shown in the lower part of Figure 2-2: elevation/depression (E/D) and protraction/retraction (P/R). Hence, with three rotational and two translational, the simplified model of the shoulder complex has 5-DOFs.

The integrated motion between ST and GH joints, which results in the displacement of the humerus, is usually referred as scapulohumeral (SH) rhythm or shoulder rhythm [26, 27]. Therefore, the position of the center of glenohumeral (CGH) joint, also referred as instantaneous center of rotation (ICR) of the shoulder joint, is dynamic and it shifts due to interactions with the shoulder girdle [28]. Moreover, there are also inevitable individual differences in anatomical characteristics and joint kinematics.

2.4 Existing Robotic Shoulder Exoskeletons

During the last two decades, a large number of robotic shoulder rehabilitation exoskeletons have been developed to assist people with upper-limb disability and extensive research efforts have been dedicated to advancing their mechanical designs, control strategies and experimental evaluations. It is useful to analyze, assess and integrate improvements in mechanical mechanisms, control systems and clinical trials of existing devices during the design stage of shoulder exoskeletons. This aids in developing a standardized rehabilitation framework for the robot assisted shoulder physical therapy.

2.4.1 Mechanism Design

Since the human shoulder complex is biomechanically ingenious, specific design considerations have to be made when developing robotic shoulder exoskeletons. In this sub-section, a brief review of the state-of-the-art robotic shoulder rehabilitation exoskeletons with their mechanism design, number of DOFs for shoulder and actuation types are presented.

2.4.1.1 Robotic Shoulder Exoskeletons Powered by Electric Actuators

A robotic exoskeleton ARMin III (Figure 2-3(a)) has been developed at the ETH Zurich for upper limb rehabilitation from its previous versions ARMin I [29] and ARMin II [30]. It was the first exoskeleton robot to be commercially available, now known as Armeo Power (Hocoma product), which has been used in several hospitals in Europe and US [31]. ARMin III exoskeleton has 6-DOFs with 3 actuated DOFs for shoulder. The joints (revolute and prismatic) of this heavy back-drivable robotic device with rigid links are actuated by DC motors with harmonic drive (HD) gearbox. The mechanical end stops, spring and laser pointers are used to increase the safety, compensate the weight and ease the patient-positioning, respectively. Furthermore, this robotic device can be easily adjusted from left to right side which makes it operationally efficient in clinics. However, the prismatic joint that lifts the whole structure takes a lot of space and complicates the actuation of the robot. The vertical motion of CGH, which is modeled as a rotational movement without any horizontal translation, is only achievable along with the arm elevation which limits training of some shoulder movements and causes misalignments between the patient and robot axes [32].

On the other hand, the specific shoulder motions in vertical translational direction, limited with ARMin III, can be trained with another 6-DOFs robotic shoulder exoskeleton called Maryland-Georgetown-Army (MGA) exoskeleton, shown in Figure 2-3(b) [33]. The shoulder complex in this robotic device is enclosed with circular rigid links with three revolute joints modelling a "ball-and-socket" joint. Moreover, this exoskeleton is among the first to take scapula motion into account considering shoulder girdle's elevation and depression [34]. However, the use of the additional motor (mounted as other motors directly on joint) that lifts the mechanism upwards could lead to joint axes misalignments and make this non-back-drivable robot more expensive and hazardous.

A robotic 7-DOFs cable-actuated anthropomorphic exoskeleton CADEN-7, shown in Figure 2-3(c), has been developed for upper extremities rehabilitation with 3-DOFs for GH joint in the University of Washington, Seattle [35]. The advantages of this device are low inertia, negligible backlash, high stiffness links, mechanical stops, emergency switches and driven pulleys that make it possible to distantly locate the actuators reducing the torques on the robot framework. The drawback of this actuation system is that it constraints the transportability and adjustability of the exoskeleton. Moreover, the electric motors used to actuate this high power robotic device are heavy. The succeeding two-arm exoskeleton system of CADEN-7 is named EXO-UL7 (developed in USCS) [36].

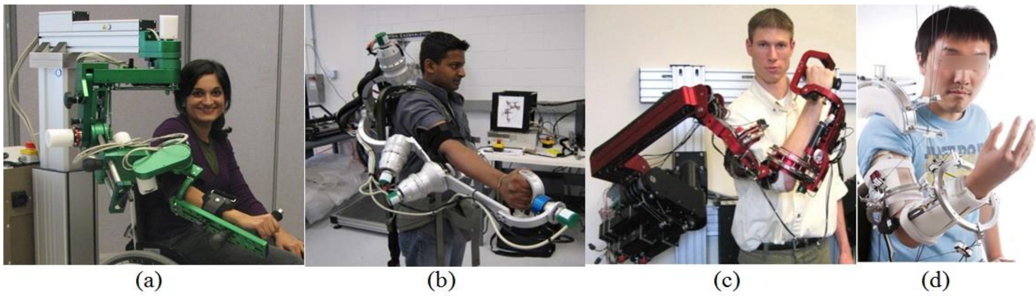

Figure 2-3: (a) ARMin III [32], (b) MGA [34], (c) CADEN-7 [37], (d) CAREX [38].

Another 5-DOFs robotic exoskeleton developed for upper arm rehabilitation is called Cable-driven ARm EXoskeleton (CAREX) (Figure 2-3(d)) [37]. Instead of the rigid links, this robotic exoskeleton has three lightweight cuffs attached around the shoulder, the upper arm and the forearm, respectively. The limb parts are moved by cables passing through the cuffs that are driven by motors. Four such cables are used for three rotational DOFs of shoulder joint. Due to the use of these cables, the motors are placed away from the human body. This actuation concept was adopted from the wearable haptic device on a human arm [38]. The rotary encoder and sensors in CAREX are used to determine the orientation of GH joint. The major advantages of this device include a reduced overall weight (1.55 kg) and loads on arm segments. The exoskeleton is not required to be aligned with human joint axes since there are no joints and links. The cables go from one segment of the arm to another without the need for independent sets of cables and there are no restrictions on natural arm movements [39]. An approach for real-time measurement of CGH with CAREX was presented in [40]. Nonetheless, more accurate estimation of the CGH and workspace analysis are still required to establish proper kinematic model. Moreover, the shoulder girdle DOFs are not assisted as the shoulder cuff remains fixed reducing the overall workspace.

The IntelliArm is a robotic exoskeleton that has more DOFs (7 active (i.e. actuated) and 2 passive) than most of the exoskeletons for upper limb rehabilitation and can independently and synchronically control the shoulder, elbow, and wrist [41]. In this exoskeleton, all 3-DOFs of shoulder joint and the vertical shift of GH joint are provided with four active DOFs whereas two passive DOF are used for anteroposterior and mediolateral displacement of GH joint. Altogether the use of these active/passive joints can thoroughly replicate the shoulder movements, and the exoskeleton’s rotation axes can be aligned with the patient’s shoulder taking into account scapular and body movements [42]. Shoulder's reaction torques and forces are measured using a torque/force sensor fixed to the shoulder. The actuation is provided through cable transmission by motors placed remotely from the patient's head. A circular guide and a cable mechanism are used for shoulder's twisting joint (internal/external rotation). Even though this exoskeleton is closely aligned with the shoulder, the heavy and expensive high-torque motors hinder its use in clinical settings [43]. A similar mechanism design with active shoulder girdle control was proposed in [25].

The National Taiwan University Hospital-ARM (NTUH-ARM) is an orthosis with seven actuated DOFs, six of which (1 prismatic and 5 rotational) account for the shoulder. This redundantly actuated robotic exoskeleton is powered by using brushed DC motors and assists all five shoulder DOFs [44]. Another electrically actuated compatible 3-DOFs shoulder exoskeleton translates two axes of shoulder joint to adapt the CGH position describing its mechanical motion using the sagittal, frontal, transverse, and rotation (SFTR) system [45].

One of the most advanced mechanism designs for shoulder rehabilitation is presented in MEDARM exoskeleton that fully covers all shoulder rotational and translational motions [46]. However, according to the authors' knowledge, no real prototype of this robotic rehabilitation device with proposed electrical type of actuation system is built. ASSISTON-SE is another proposed exoskeleton for shoulder rehabilitation that has five active DOFs and a passive slider to fully assist all shoulder motions [47]. Another recent exoskeleton with three parallel linear electric actuators (3-DOFs) for the shoulder joint and a passive slip interface (2-DOFs) for the shoulder girdle is developed in the Arizona State University [48].

Some other robotic shoulder rehabilitation exoskeletons powered by electromagnetic actuators are L-EXOS [49], SUEFUL-7 [50], ALEx (commercial product developed at PERCRO lab) [51], KINARM (BKIN Technologies) [52], ETS-MARSE [53], ARAMIS [54], ARMOR [55], IKO (hybrid actuation with electric motors for shoulder) [56], mobile 3-DOFs motion assist exoskeleton [57], 5-DOFs robotic exoskeleton in SCUT lab [58], Sensoric Arm Master (SAM) [59], Shoulder Rehabilitation Robot (SRR) [60], ABLE [61] and MULOS [62].

2.4.1.2 Shoulder Exoskeletons Powered by Pneumatic Actuators

A pneumatically actuated lightweight exoskeleton, called Robotic Upper Extremity Repetitive Therapy (RUPERT), was developed for use in physical therapy by researchers at Arizona State University [63]. The latest version of this wearable 5-DOFs robotic orthosis named RUPERT IV (Figure 2-4(a)) had gone through several improvements over almost ten-year period [64]. This portable back-drivable robot is driven by unpaired compliant pneumatic artificial muscles (PAMs) with a high power to weight ratio, also referred as McKibben muscles. PAMs can contract or extend using the compressed air. Compared to the previous designs, RUPERT IV has added 1-DOF for shoulder joint providing shoulder external rotation and elevation [65]. Larger torques can be achieved at shoulder joint by increasing the pressure or the diameter of air muscles [66]. Composite materials are used to reduce the overall weight of this rehabilitation robot that can be worn while standing or sitting. Another important design characteristic of this exoskeleton with adjustable lengths of arm segments is that it was developed without gravity compensation promoting practices in a natural setting [63]. However, PAMs for each joint can only provide unidirectional actuation. Moreover, the restrictions at shoulder joint in this device limit the full range of motion of the human arm.

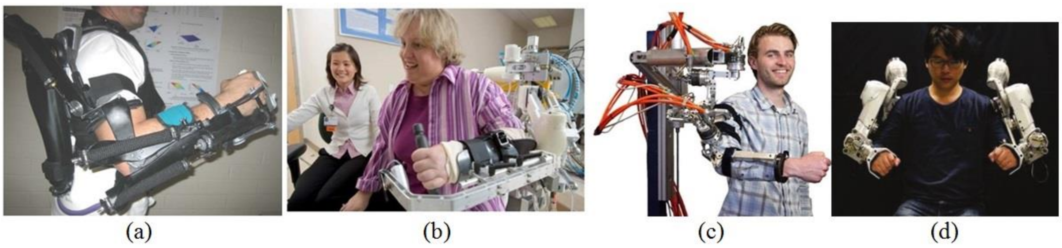

Figure 2-4: (a) RUPERT IV [65], (b) Pneu-WREX [69], (c) LIMPACT [80], (d) HARMONY [82]

Pneu-WREX (Figure 2-4(b)) developed at the University of California [67] based on passive exoskeleton T-WREX [68] is a lightweight pneumatically driven robotic orthosis for physical therapy of the upper limb. Pneu-WREX, using pneumatic actuators and a spring to balance its own weight, generates a wide range of active forces to provide naturalistic arm movements and includes a number of safety features [69]. Four out of five DOFs of this device are designed for shoulder complex. Each of these DOFs is actuated by a low-friction pneumatic cylinder.

Biomimetic Orthosis for the Neurorehabilitation of Elbow and Shoulder (BONES) based on a parallel mechanism is a pneumatically actuated exoskeleton with 3-DOFs for shoulder motion [70]. A humanlike musculoskeletal shoulder robot actuated by the pneumatic artificial muscles, assembled like natural human muscles, to replicate complex shoulder movements is developed by the researchers from Osaka University [71. Some other robotic shoulder rehabilitation orthoses powered by pneumatic actuators are SRE (using PAM) [72], “Muscle Suit” (McKibben muscles) [73], ZJUESA [74], KIST (pneumatic and electric brake actuators) [75], 7-DOFs wearable robotic arm [76] and an exoskeleton for shoulder elevation [77].

2.4.1.3 Shoulder Exoskeletons Powered by Hydraulic Actuators and Series Elastic Actuation (SEA)

A compliantly actuated robotic exoskeleton LIMPACT (see Figure 2-4(c)) has been developed for use in stroke therapy which consists of four rotational series elastic hydraulic motors and torsion springs [78]. The mechanical design of this robotic exoskeleton with 3-DOFs (actuated) at the shoulder joint is based on a passive exoskeleton called Dampace [79], the predecessor of LIMPACT, in which the Bowden cables and disk brakes were used instead of hydro-elastic actuation. The model of LIMPACT exoskeleton is divided into four sub-models with a total of 18 rigid parts combined by 20 revolute joints [80]. Both Dampace and the LIMPACT have passive self-aligning shoulder mechanisms and take into account the translational DOFs in the shoulder. Also, LIMPACT is able to align the shoulder without a controller, and a motor passively balancing the system with gravity compensation [80]. However, such passive aligning mechanisms are confined in supporting patients during GH mobilization trainings [47]. Moreover, this robotic device currently can only be used in research facilities due to the expensive installation of its actuation system which has a large and unsafe hydraulic pump [80]. Another example of a hydraulically actuated upper limb exoskeleton with 3-DOFs for shoulder is called Sarcos Master Arm [81].

A two-armed exoskeleton called HARMONY (Figure 2-4(d)) with SEAs at every joint has been developed at the ReNeu Robotics Lab, University of Texas [82]. It provides 5-DOFs (active) for each shoulder: 3-DOFs rotations at the GH joint and 2-DOFs for the shoulder girdle movement. The developed shoulder girdle mechanism is able to change circular motions in different directions with the designed parallelogram and rotary joint. HARMONY is a stationary upper limb exoskeleton that connects to human body at three places on each side and can be adjusted to fit various body sizes. However, it could still be considered as a heavy and large robotic exoskeleton with complex configuration.

Another device designed for post-stroke shoulder rehabilitation with series elastic actuation is a wearable cable-driven compliant shoulder brace [83]. It is a deformable and lightweight elastic device with two Bowden cables used for power transmission. Encoders and inertial measurement unit (IMU) sensors are used to measure cable lengths and orientation offsets in real time, respectively. However, this soft orthosis has a very limited mobility with just 1-DOF for shoulder A/A movement. Some other robotic shoulder rehabilitation orthoses with series elastic actuation or elastic elements found in the literature are intrinsically compliant continuum shoulder exoskeleton [84], wearable shoulder exoskeleton [85] and MUNDUS [86].

2.4.2 Control Strategies

Control strategies for the robotic upper limb rehabilitation exoskeletons are developed to repetitively guide the patients' limbs on anatomically and ergonomically feasible trajectories so that the patients can regain muscular strength. Development of these control strategies has also been an important area of research in the robot upper limb rehabilitation [44, 58, 87-91].

The control strategies for upper-limb rehabilitation robots can be classified in different ways. In one of the recent reviews on upper-limb exoskeletons, the authors categorized control methods based on input information (human biological signal, non-biological signal, platform independent method), output of the controller and controller architecture [10]. In [12], the authors considered "high-level" (assistive control, challenge-based control, haptic stimulation and non-contacting coaching) and "low-level" (impedance control and admittance control) control algorithms used by robotic devices in upper-limb rehabilitation, following the terminology proposed in [87]. In short, the former control strategies are directly intended to raise motor unit plasticity while the later regulate parameters such as impedance, admittance, force and position [12]. In [91], the exoskeleton control systems were classified based on the model (dynamic and muscle), the hierarchy (task, high and low levels), the physical parameters (position, torque/force and force interaction) and the usage (virtual reality, teleoperation and gait).

Assist-as-Needed (AAN) control is an active assisting training paradigm in recent rehabilitation practices supporting patient's motion with the minimal amount of assistance. The concept behind the development of AAN algorithms is to modify the robotic assistance according to the disability level and effort put by the patients during the rehabilitation process. If the patients show some progress and recovery by incorporating their muscular strength, the robotic assistance is reduced and vice versa. This control strategy, in which robotic device does not need to operate for the full duration of the motion, increases the patient's muscle activity being one of the promising control technique in recovery. Commonly, such control algorithms incorporate the desired trajectory with a resistance field that estimates the required supportive action. Therefore, impedance schemes and adaptive controllers are usually applied within AAN control paradigm [92]. A number of AAN control strategies has been developed and implemented for shoulder rehabilitation robots as follows.

Adaptive "assist-as-needed" and force field control methods have been used for CAREX exoskeleton to control the cable tension [39]. An "assistance-as-needed" controller that can be adapted during the action was developed for Pneu-WREX exoskeleton with non-linear force controller for pneumatic actuators [69]. An active assisted mode has also been realized in LIMPACT exoskeleton. Its overall control architecture consists of a torque and an impedance controller. The inner-loop torque controller includes a Smith predictor with a lead-lag filter and the outer-loop impedance controller incorporates a gravitation vector with a state feedback controller [80]. An assistive control system has been developed for NTUH-ARM exoskeleton based on the human arm dynamics obtained with a pair of 6-axis force/torque sensors and gravity compensation [44]. To ensure the efficacy of the proposed control strategy, the authors made the Lyapunov stability analysis prior to its experimental evaluation [44].

Most of the shoulder robots (L-EXOS, MGA, SRE to name a few) use impedance or/and admittance control schemes with joint angles and torques as control inputs to govern robotic assistance. All axes in ARMin III can be controlled with an impedance scheme in addition to computed torque (CT) control and proportional derivative (PD) control [32]. The EXO-UL7 exoskeleton system has been controlled with a linear proportional–integral–derivative (PID) controller and a PID admittance controller [93]. The control scheme that considers shoulder's scapulohumeral rhythm with coupling torque based on impedance has been developed for HARMONY exoskeleton [82]. The impedance control with ongoing feedback and a band-pass filter has been implemented in SRR exoskeleton [60]. The safety-improved nonlinear adaptive controller has been implemented in 5-DOFs upper-limb rehabilitation exoskeleton [88]. In [94], the trajectory control strategy has been presented based on human arm movements. A Lyapunov-based control strategy implemented on the shoulder robot design is presented in [95].

For RUPERT IV, a closed-loop adaptive controller has been designed for passive task training with each DOF controlled by a PID feedback controller [65]. In addition, the shoulder controller also has an Iterative Learning Controller (ILC) which can learn from the preceding estimation on individual basis and update a suitable feedforward command. A total of 13 fuzzy rules were selected to deal with the nonlinearities caused by pneumatic actuation in RUPERT IV [65]. The detailed description of implemented adaptive active-assist and cooperative modes using the controllers in RUPERT IV is given in [96].

The impedance (IMP) or admittance (ADM) control methods are usually developed without considerations of user's intention or physical condition which might be done by implementing control systems based on the electromyographic (EMG) signals [90]. The impedance control based on surface EMG signals has been implemented in shoulder robots such as ETS-MARSE [97], SUEFUL-7 [50], motion assist robots [57], MUNDUS [86], musculoskeletal robot arm [71] and 5-DOFs exoskeleton in SCUT lab [58].

2.4.3 Experimental Clinical Trials

Substantial work has been done in order to advance the mechanism design and some control aspects of robotic shoulder rehabilitation exoskeletons. However, a few attempts have been made to test the actual performance of these exoskeletons in clinical settings. Nevertheless, during the last decade, the robotic shoulder exoskeletons are gradually moving from research facilities to rehabilitation settings in order to provide physical therapy to patients with stroke-induced impairments, spinal cord injuries (SCI), multiple sclerosis (MS) and cerebral palsy.

ARMin II and ARMin III have been experimentally evaluated and used in clinics more than any other robotic shoulder rehabilitation exoskeletons. Four chronic stroke patients (in this case more than 12 months post stroke) participated in 3-4 one hour sessions per week for 8 weeks in robot-aided therapy with ARMin II exoskeleton [98]. The main measure of treatment results was Fugl-Meyer Score of the upper extremity Assessment (FMA-UE), whereas changes in evaluations such as Wolf Motor Function Test (WMFT), Catherine Bergego Scale (CBS), Maximal Voluntary Torques (MVTs) and some questionnaire were secondary outcome measures. The experimental data showed significant positive progress of arm motor function in three out of four enrolled subjects. This formed the ground for future robot-assisted clinical studies.

A large parallel-group randomized trial was conducted in four clinical centers in Switzerland with chronic stroke patients (more than 6 months) to compare the effects of conventional therapy in neurorehabilitation and the training with robotic exoskeleton (ARMin III) [99]. After the initial surveying, eligibility assessment, randomization and exclusions, 35 subjects were assigned to conventional and 38 to robot-assisted therapies. Both groups received 45 minutes training sessions 3 times per week for duration of 8 weeks. The primary evaluation tool (FMA-UE) was tested at different periods of the clinical trial. The findings showed that subjects who received robot-aided therapy had much greater advancements in affected arm's motor function consequently leading to a conclusion that exercises with a robotic device can more effectively increase the motor function in stroke patients than traditional manual physical therapy. Another recent clinical study with ArmeoPower exoskeleton involved 35 stroke patients with hemiplegia who received 40 one hour sessions 5 times a week for 8 weeks and were assessed on FMA and Modified Ashworth (MA) scales [100]. The outcomes of this trial also indicated that use of the robotic exoskeleton can enhance motor function in upper limb rehabilitation.

Twenty chronic stroke subjects used BONES exoskeleton receiving single joint and multi-joint therapies 3 times per week for a duration of 4 weeks [101]. Box and Block Test (BBT) was the main assessment measure, while secondary outcome variables were FMA, WMFT, Motor Activity Log (MAL) and some tests on shoulder strength and speed. The findings suggest that use of a robotic device increased the motor function of patients but no major differences were reported in the outcome of multi-joint and single-joint trainings. The AAN control strategy developed in [69] has been employed in this study.

L-EXOS exoskeleton was evaluated with 9 chronic stroke subjects for 6 weeks. Clinical study with kinesiology assessment based on EMG analysis has been conducted and evaluation measures such as FMA and MA has been performed [102]. As a result, the statistical improvements of measured variables (shoulder motion parameters) with some correlations are reported. The favorable results were attained with the NTUH-ARM exoskeleton in clinical trials with six stroke patients verifying the effectiveness of the AAN control [44]. Fourteen stroke subjects with hemispheric lesions were enrolled in clinical study with 6-DOFs dual exoskeleton robot ARAMIS in 50 minute sessions 5 times a week for a duration of 7 weeks [103]. The FMA scores significantly increased for all patients at the end of training process.

RUPERT IV exoskeleton has been tested in two feasibility studies using reaching-out tasks in a 3D virtual reality environment to validate the effectiveness of a task based robot-assisted repetitive therapy [104]. Six stroke patients were involved in the first study to receive 4 weeks (one-hour session 3 times per week) clinic based robot-assisted therapy and two other patients used this wearable device for the same period on a daily basis at home. The clinical results showed that only few of the involved patients demonstrated improvements and statistical evaluations have shown that only half of the patients trained in clinic had some functional improvement. Both subjects who used RUPERT IV in a home setting showed significant advancements in their performance. However, there is inconsistency in the given results and mainly it is because of the small number of patients involved with a significant variance between their disability levels. Moreover, the duration of these studies might be not long enough to achieve a proper conclusion [104].

There are also other chronic/stroke patient (c/sp) interaction studies reported in the literature with robotic shoulder rehabilitation exoskeletons such as Pneu-WREX (23 csp) [105], ARMOR (8 sp) [56], ABLE (7 sp) [106], EXO-UL7 (10sp) [107], IntelliArm (3 sp) [42] and MUNDUS (3 SCI and 2 MS) [86].

CAREX has been tested with healthy subjects and one stroke patient. However, more experiments are still needed in order to test larger ranges of GH joint motions [38]. Experimental evaluations with the HARMONY exoskeleton have demonstrated that the controller produced correct movement for SH rhythm and also induced gentle forces when the shoulder exhibited an abnormal rhythmic motion. Some of the other experimental evaluations with healthy subjects (hs) were performed with the following shoulder robotic exoskeletons: ALEx (6-hs) [51], "Muscle Suit" (5-hs) [73], SUEFUL-7 (2-hs) [50], motion assist robot (2-hs) [57], CADEN-7 (1-hs) [35] and MULOS (1-hs) [62].

2.5 Summary and Conclusion

In addition to assisting the spherical shoulder joint, some of the above reviewed robotic shoulder exoskeletons also consider translational motions of the shoulder girdle by translating one (ARMin II-III) or two (3-DOFs compatible exoskeleton [45]) axes of the shoulder joint with coupling mechanism or by designing a special mechanical linkage [57]. The shoulder girdle movements can also be assisted using one (MGA, Pneu-WREX, exoskeleton in [108]) or more (MEDARM, NTUH-ARM, HARMONY, musculoskeletal shoulder [71]) additional active DOFs, passive self-alignment (Limpact, SUEFUL-7) or with the use of both active and passive DOFs (IntelliArm, IKO, ASSISTON-SE). It may be argued that the costs, weight and control complexity of such mechanical advancements are not worth the benefits obtained with them during the physical therapy [109]. For example, in exoskeletons such as CADEN-7, L-EXOS and CAREX, these translational shoulder movements are compensated by body movements with fixed CGH.

Apart from the consideration of the shoulder girdle movement, some other advantages of the main existing robotic shoulder exoskeletons are reduced weight (CAREX, RUPERT IV), availability for both arms (ARMin III, EXO-UL7, IntelliArm, HARMONY) and gravity compensation (e.g. Pneu-WREX, LIMPACT, L-EXOS, MGA). Singular positions (singularities) that can occur in the mechanisms during the movement of robotic structures is another important consideration taken into account in CADEN-7, L-EXOS, MGA and exoskeleton in [108] (by tilting the position of the motors), BONES (by restricting the workspace), NTUH-ARM (by adding extra DOF) and MEDARM (designed so that singularities occur further from the normal workspace). In mechanisms with a passive self-alignment, singularities can occur within the workspace [109]. The majority of the existing shoulder rehabilitation devices have been actuated with conventional bulky motors due to the ease of their control, availability and low cost. In others, cables and pulleys are used for power transmission to locate the heavy motors away from a human body. On the other hand, lightweight PAMs have a higher power to weight and power to volume ratios but are more difficult to control due to the structured nonlinearities in their dynamic model. The hydraulic actuators have even a higher power to weight ratio than PAMs but their installation in most cases is problematic and raises health and safety problems due to the nature of liquids used. In addition, compliant actuators with series elastic elements, other deformable, combined types of actuation with improved functional capabilities and back-drivable transmissions can be developed to deliver more efficient and comfortable use of robotic shoulder exoskeletons.

The control algorithms used influence the performance characteristics and efficiency of the robotic shoulder rehabilitation devices. Robust and non-linear control algorithms must be developed and implemented for the new generation of robotic shoulder rehabilitation exoskeletons powered by intrinsically compliant actuators. With the technological developments in the brain machine interfaces, new control systems able to identify subject's intention should be considered. Advanced AAN training strategies need to be developed and the already existing AAN strategies should be clinically evaluated to provide benchmarks in the level of assistance provided to neurologically impaired patients. There are also different ways how the developed robotic shoulder exoskeletons could be controlled: with the mind, control panel, joystick or other interfaces.

Several clinical trials with stroke patients have been conducted using different shoulder exoskeletons. The recent findings of such evaluations have showed some motor function improvements in subjects' upper limb. Moreover, modern technologies like human-robot interfaces with a virtual reality environment, different games and functional exercises boost the intensity of training process, increasing the efficiency of such robotic devices in upper limb rehabilitation. However, more studies with various shoulder exoskeletons are needed involving larger groups of patients with different levels of neurological impairments to confirm their effective physical therapy outcomes. Furthermore, only a few of the existing robotic shoulder orthoses can be tested at home based settings. Even though the same assessment measures are mostly used in these trials, the direct comparison is difficult due to differences in patients' disability levels, age and initial evaluation scores, duration of the therapies, study protocols and types of training sessions. Table 2-1 shows the clinical outcomes of various selected studies with the developed shoulder robotic exoskeletons, their number of DOFs for shoulder and implemented control strategies.

Table 2-1. Shoulder exoskeletons used in clinical studies.

Device	**Shoulder DOF**	**Control method**	**Patient #**	**Clinical Outcome**
ARMin III	3 active	IMP, PD, CT	38 cs	↑FMA
ArmeoPower	3 active	IMP, PD, CT	35 s	↑FMA ↑MA
Pneu-WREX	4 active	IMP, PD, AAN	23 cs	↑FMA ↑BBT
BONES	3 active	AAN	20 cs	↑BBT ↑FMA
EXO-UL7	3 active	PID, ADM, EMG	10 s	↑ROM
L-EXOS	3 active	IMP, PD	9 cs	↑FMA ↑MA
NTUH-ARM	6 active	AAN	6 s	↑FMA
c(s) – chronic (stroke); ROM – ranges of motion, # - number				

The summary of the main existing robotic shoulder exoskeletons with their advantages and disadvantages is provided in Table 2-2 which was tabulated based on upper arm segments, number of DOFs, shoulder girdle assistance, types of actuation, control methods and clinical studies.

To conclude, it is hard to identify a common specific limitation of the existing shoulder exoskeletons as they all have their own advantages and disadvantages when compared with each other, as shown in Table 2-2. For instance, the exoskeletons that can actively assist the shoulder girdle, which is an important feature to consider in shoulder rehabilitation, are equipped with heavy and bulky motors in series with the human limb increasing the overall weight on the arm. On the other hand, the exoskeletons that place the actuation system away from the human body do not assist all DOFs of the human shoulder. Also, the most suitable exoskeleton for rehabilitation with cable-driven module, which is very lightweight and avoids the joint axes misalignments around the spherical shoulder joint, has a fixed shoulder cuff that decreases its overall workspace and does not assist the shoulder girdle motions.

As a result, the design of the developed HYBRID-SRE in this work aims to incorporate these features: independent assistance to all shoulder DOFs including the shoulder girdle to have a larger workspace, parallel structure around the shoulder joint to avoid the joint axes misalignment issues, placement of the actuation system on the fixed support and use of the cable-driven module to adopt its superior properties (less mechanical interference, lower inertia, less restriction to “free” movements, flexibility, elimination of mechanical joints) and to make the overall structure lightweight. Therefore, to achieve this goal, the mechanism design of the developed shoulder exoskeleton in this work consists of rigid and cable links, active and passive joints, serial and parallel modules, redundant actuation with rotational and linear drives, which all makes it a “hybrid” exoskeleton, from which its name is derived.

Table 2-2. Summary Table of Existing Robotic Shoulder Rehabilitation Exoskeletons.

Device *(based on)*	**UL segment**	**DOF Total/Shoulder**	**SG motion**	**Type**	**Control method**	**Advantages**	**Disadvantages**	**Clinical Study (sp)**
ARMin III* *ArmeoPower*	S+E+(W)	6a/3a	E/D - c	e	IMP, PD, CT	Back-drivable, available for both arms, no extra actuators for SG aligning	High inertia, simple model of (limited) shoulder motion	yes
EXO-UL7 *(CADEN-7)**	S+E+W	7a/3a	no	e/c-d	PID, ADM, EMG	Low inertia, negligible backlash, high stiffness links, mechanical stops, emergency switches and driven pulleys, available for both arms, KS considered	Constrained in the transportability and adjustability, motors are heavy and big	yes
IntelliArm*	S+E+W	7a/(4a + 2p)	E/D - 1a, P/R - 2p	e/c-d	VR	Self-alignment (no additional adjustment required), accurate SG motion, available for both arms	Motors are heavy, no actuation for P/R, singularities occur	no
CAREX*	S+E	5a/3a	no	e/c-d	IMP, AAN	Lightweight, push/pull forces without rigid links and joints, actuators remotely located	Stationary, no shoulder girdle control	no
RUPERT IV*	S+E+W	5a/2a	no	PAM	FFC, PID	Lightweight, easily wearable, back-drivable	Limited shoulder movements, slow motion only	yes
Pneu-WREX* *(T-WREX)*	S+E	5a/4a	P/R – 1a	p	IMP, PD, AAN	Gravity compensated, control safety systems, visual and audio feedback	Only slow limited movements	yes
LIMPACT * *(Dampace)*	S+E	4a/(3a + 2p)	passive	rHEAs	IMP	Self-alignment, gravity compensated	Expensive installation of its actuation system, singularities occur	no
L-EXOS*	S+E+W	5a/3a	no	e/c-d	SMC, IMP PD	Gravity compensation, low impedance, high payload, actuators remotely located, improved stiffness	Heavy, expensive to manufacture and maintain	yes
BONES *	S+E+W	6a/3a	no	p	AAN	Parallel structure, allows forearm rotation without the use of a ring bearing, allows use of large actuators (need not to be moved), KS considered	Reduced workspace, no SG control	yes
NTUH-ARM *	S+E	7a/6a	E/D - 1a, P/R – 1a	e	AAN, IMP, EMG	Adjustable to various lengths of arm, no circular guide for shoulder motion, full SG control, two 6-DOF force/torque sensors, safety issues, KS considered	Heavy, redundant design	yes
<u>MEDARM</u>	S+E	6a/5a	E/D - 1a, P/R – 1a	e/c-d	-	Independent monitoring and control of all 5-DOFs of the shoulder complex	Complex structure, circular approximation of CGH motion (misalignment occurs), no real prototype (only Planar 3DOF)	no
IKO*	S+E+(W)	5a/(3a + 3p)	passive	hybrid	PI	Self-alignment	Singularities occur	no
<u>MGA</u>	S+E+(W)	5a/4a	E/D - 1a	e	IMP, ADM, PD	Gravity compensation, allows high humerus elevation (147°)	Additional motor, high inertia, not back-drivable, no actuation for P/R (misalignment occurs)	no
ASSISTON-SE	S+E	6a/(5a + 1p)	E/D - 1a, P/R – 1a	e/SEA	-	Back-driveable, both passive (slider) and active shoulder girdle control	Mechanism dimensions and transmission ratios are not optimized, proposed actuation is not implemented	no

UL – upper limb; S – shoulder; E – elbow; W – wrist; E/D - elevation/depression; P/R - protraction/retraction; SG – shoulder girdle; PAM - pneumatic artificial muscles; rHEAs - rotational hydro-elastic actuators; SEA – series elastic actuation; IMP – impedance, PD – proportional derivative; PID - proportional–integral–derivative; CT – computed torque; ADM – admittance; VR – virtual reality based; FFC – feed forward control; EMG – electromyogram based; SMC – sliding mode control; c - coupling; a – active; p –passive, e – electric; c-d – cable-driven, p – pneumatic; KS – kinematic singularities; sp – stroke patient.

*Journal Publication, <u>Highly cited Conference Paper</u> (>80)

Chapter 3

Biomechanical Modelling of the Human Shoulder

3.1 Introduction

This chapter contributes to the research in biomechanical modelling of the human shoulder and is organized as follows. Section 3.2 introduces the proposed model of the human shoulder with the modified parallel shoulder girdle mechanism along with a kinematic model of the shoulder with a minimum number of parameters. Section 3.3 describes the kinematic model of the human shoulder based on the other models from the literature. Section 3.4 presents the parallel mechanism based model of the human shoulder girdle with its detailed kinematic analysis. In Section 3.5, a case study with the proposed shoulder parallel mechanism is presented where the minimal coordinates have been used to plan the abduction of the arm in the scapular plane. Finally, Section 3.6 presents a discussion on the results and limitations of the proposed model.

3.2 Background

There is a constant need for an improved biomechanical model of the shoulder that can appropriately simulate complicated upper limb movement patterns. A demand for a proper biomechanical model of the shoulder comes from the applications such as examination of motion impairment, tendon-transfer surgeries, simulation of human postures and movements in digital environments, assessment of muscle strengths and metabolic values, design of robotic rehabilitation exoskeletons and other areas that require shoulder motion planning [110]. Despite the considerable amount of research that has been done on this topic, the complete analysis of the intricate kinematics of the human shoulder remains a challenging task. In this work, the analysis techniques used in robotics fields are applied on musculoskeletal shoulder complex to model the shoulder as a mechanism.

To date, only a few musculoskeletal models for the shoulder and upper limb have been developed that are most commonly used for a variety of purposes [110]: Swedish Shoulder Model [111, 112], Delft shoulder and elbow model (DSEM) [113, 114], Newcastle shoulder model (NSM) [115], Holzbaur's upper extremity model (HM) [116], Anybody model [117], Garner's model [118] and Dickerson's model [119]. Owing to the increasing interest of researchers in kinematic properties of the human shoulder, a number of different shoulder models based on open-loop [120-124] and closed-loop kinematic chains [123, 125-130] have been developed. Characteristically, the open-loop chain shoulder models have rather basic structures which simplify the kinematic and dynamic analyses. However, most of them do not consider the gliding motion of the scapula over the thorax. On the contrary, the closed-loop chain models with higher precision and load carrying capacity can have singular points within their limited workspace.

The human shoulder can be considered as a parallel-serial mechanism whereby the shoulder girdle (thorax, clavicle and scapula) is a positioning and orienting parallel mechanism for the humerus which is serially connected through the GH joint. Generally, the SC joint that connects the clavicle to the thorax, the AC joint that connects the scapula to the clavicle and the GH joint are modelled as ideal three degrees of freedom (3-DOFs) ball-and-socket joints. However, a sphere-on-sphere model [131] and deformable joint [132] have also been proposed to model the GH joint.

The scapulothoracic (ST) articulation makes the shoulder girdle a closed kinematic chain constraining the scapula to move over the thorax and reduces the overall DOFs of the shoulder. Therefore, the gliding motion of the scapula bone is usually modelled using geometrical constraints: a contact between one [129, 131], two or three [114, 128, 133, 134] fixed points belonging to the scapula with an ellipsoid (or cone [126]) representing the thorax. In fact, physiologically, this contact point is not fixed on the scapula bone during the shoulder movements [135]. Therefore, the shoulder models with fixed ST contact points may lead to nonphysical scapula movements [129]. The models that have a tangential ST constraint [136, 137] (the scapula plane to be normal to the ellipsoid) result in a more physiological ST model [138]. In contrast to rigidly constrained scapula models, the integrated kinematic interaction between the scapula and the humerus, usually referred as scapulohumeral (SH) rhythm or shoulder rhythm, leads to another approach with regression equations where the scapula and clavicle joint angles have been defined as a function of the humeral angles [112, 139-142]. However, the drawbacks of these regression models are that they do not respect the ST constraints, cannot describe the independent scapula and humerus motions and cannot distinguish pathological shoulder. In [131], it has been argued that the introduction of the kinematic constraints is more pertinent than the use of couplings between the shoulder joints' coordinates. Further, in order to obtain an adequately modelled shoulder kinematics, the contact constraints have been added to the shoulder rhythm model in [143]. A recently developed OpenSim biomechanical model of the ST joint, based on an internal coordinate joint formulation (ellipsoid mobilizer), enforces the motion of the scapula without kinematic surface constraints and describes the scapular kinematics with 4-DOFs [137].

In [128], the human shoulder girdle structure has been modelled as a 2-3 (number of base-top joints) parallel mechanism with the thorax as a base and scapula as a moving platform where the scapula-thorax two holonomic constraints have been replaced with two UPS (universal-prismatic-spherical) kinematic chains with passive prismatic pairs. In comparison to the joint angle-description of shoulder kinematics, by modelling the shoulder girdle as a parallel mechanism, a set of independent parameters equal to the number of DOFs were introduced and referred as *minimal coordinates*. The minimal coordinates that have the advantage of being independent incorporate the constraints. The use of such minimal coordinates considerably facilitates the kinematic motion planning procedure given their independence. A kinematic analysis of the parallel model in [128] led to the construction of three alternative forward kinematic maps and three minimal sets of independent coordinates. However, constructing a dynamic model using these coordinates is somewhat problematic as these coordinate sets need to be mapped back to the joint angle parameterization and they do not have an immediate physiological implication.

In the light of the above, this chapter presents a kinematic model of the human shoulder with the modified parallel shoulder girdle mechanism. First, the ST articulation is modelled with only one scapula point constrained to move on the surface of the thorax (ellipsoid) which leads to 8-DOFs for the shoulder complex: nine kinematic coordinates subject to one constraint. Then, this contact constraint is replaced with the equivalent UPS kinematic chain with passive prismatic joint which leads to only one additional forward kinematic map. Finally, by introducing four additional UPS links with active prismatic joints, which do not alter the number of DOFs, the human shoulder girdle is modelled as a 6-4 parallel mechanism. The configuration of the 4-DOFs scapula is then parameterized in terms of four active link lengths. This has resulted in a set of minimal independent parameters that can all have a direct geometrical significance and can be easily used in the dynamic analysis of the human shoulder. Subsequently, the forward kinematic modelling of the proposed parallel mechanism is derived in a way such that the ST contact point can move on the scapula plane during the given shoulder motion. In addition, the proposed model can also be adapted for pathological shoulder cases. Using the proposed kinematic model, a feasible parallel mechanism can be designed to have equivalent kinematic properties to those of a human shoulder girdle.

3.3 A kinematic model of the human shoulder

The geometric model of the shoulder and the bony landmarks used in this work are based on recommendations of the International Society of Biomechanics (ISB) [144]. The kinematic model parameterizes the movement of each of the three bones in the shoulder relative to the thorax which is fixed. Each bone is represented by the following bony landmarks shown in Figure 3-1: thorax (IJ, PX, T8, C7), clavicle (SC, AC), scapula (AA, TS, AI) and humerus (GH, HU).

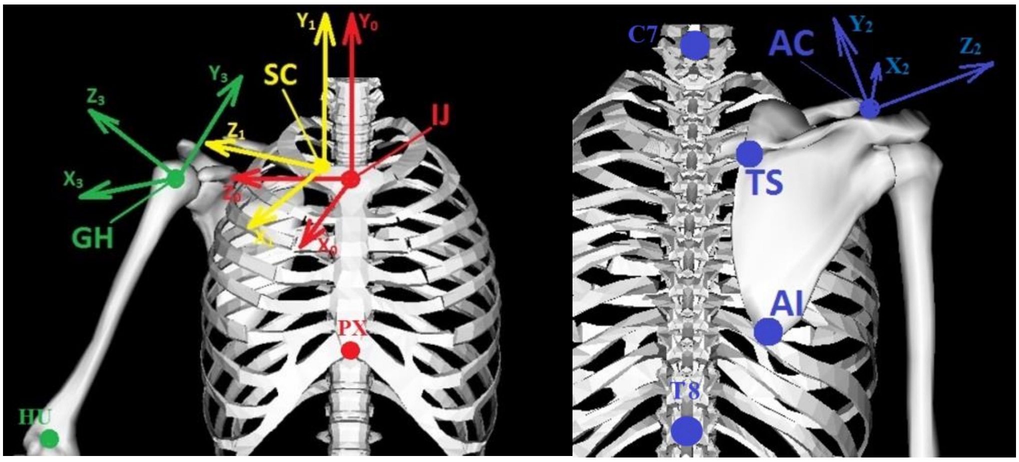

Figure 3-1: The shoulder bony landmarks and coordinate systems (0 – thorax, 1 – clavicle, 2 – scapula, 3 – humerus). Images are created using OpenSim model [145].

The local coordinate systems (clavicular, scapular and humeral) are centered at the joints around which the corresponding shoulder bones rotate: the clavicle around the SC joint, the scapula around the AC joint and the humerus around the GH joint. These reference systems are constructed following the guidelines set by ISB. A subindex is attributed to each reference frame shown in Figure 3-1. The thorax is defined as the carrier body and is attributed to the subindex 0.

The SC, AC and GH joints are modelled as ideal ball and socket joints and parameterized using the sets (ξ) of Euler angles.

$$\xi_i = (\delta_i \ v_i \ \varphi_i)^T \qquad i = 1, 2, 3 \tag{3-1}$$

The Euler angles ($\delta_i \ v_i \ \varphi_i$) are all equal to zero when the corresponding coordinate system is aligned with the initial reference system (attached to the thorax at IJ). The rotation sequences for the SC and AC joints are defined as Y-X-Z. The rotation sequence for the GH joint is defined as Y-X-Y. These angles and sequences are based on the ISB guidelines. Thus, the shoulder's configuration is parameterized by a vector of nine joint angles.

The coordinate transformations between the frames are defined as follows:

$$P_{0,1} = \mathbf{R}_1 P^1 + P_1^0 \tag{3-2}$$

$$P_{0,2} = \mathbf{R}_2 P^2 + P_2^0 = \mathbf{R}_2 P^2 + \mathbf{R}_1 P_2^1 + P_1^0 \tag{3-3}$$

$$P_{0,3} = \mathbf{R}_3 P^3 + P_3^0 = \mathbf{R}_3 P^3 + \mathbf{R}_2 P_3^2 + \mathbf{R}_1 P_2^1 + P_1^0 \tag{3-4}$$

$$\mathbf{R}_{\boldsymbol{i}} = \mathbf{R}(\mathrm{z}, \varphi_i)\mathbf{R}(x, v_i)\mathbf{R}(\mathrm{y}, \delta_i) \qquad i = 1, 2 \tag{3-5.1}$$

$$\mathbf{R}_{\mathbf{3}} = \mathbf{R}(\mathrm{y}, \varphi_3)\mathbf{R}(x, v_3)\mathbf{R}(y, \delta_3) \tag{3-5.2}$$

Here P^i and $P^0{}_i$ represent the vector expressed in the i^{th} frame (i = 0, 1, 2, 3) and the vector from the origin to the i^{th} frame, respectively. $\mathbf{R}_{\boldsymbol{i}}$ represents the rotation matrix obtained from the product of the basic rotation matrices, such as **R**(axis of rotation, angle of rotation).

The ST contact is the contact between the scapula and thorax. The scapula plane can be defined by three bony landmarks TS, AI and AC (Figure 3-1). The thorax is modelled as an ellipsoid with half-axis dimensions a, b, and c [128, 134, 146]. An additional coordinate frame is attached to the center of the ellipsoid E with the half-axis dimensions being aligned with the orthogonal axes of the frame. It is known that the intersection of an ellipsoid and a plane is an ellipse (Figure 3-2(a)). In the current model, the center of this small intersection ellipse is considered as the ST contact point. The one ST contact holonomic constraint can be written in the following form:

$$\Phi_{ST}(\xi_1, \xi_2) = \frac{(x_{ST}-x_E)^2}{a^2} + \frac{(y_{ST}-y_E)^2}{b^2} + \frac{(z_{ST}-z_E)^2}{c^2} - 1 = 0 \tag{3-6}$$

Here (x_{ST}, y_{ST}, z_{ST}) and (x_E, y_E, z_E) are the Cartesian coordinates (vectors $P^0{}_{\mathrm{ST}}$ and $P^0{}_{\mathrm{E}}$) of ST point and the center of ellipsoid E, respectively.

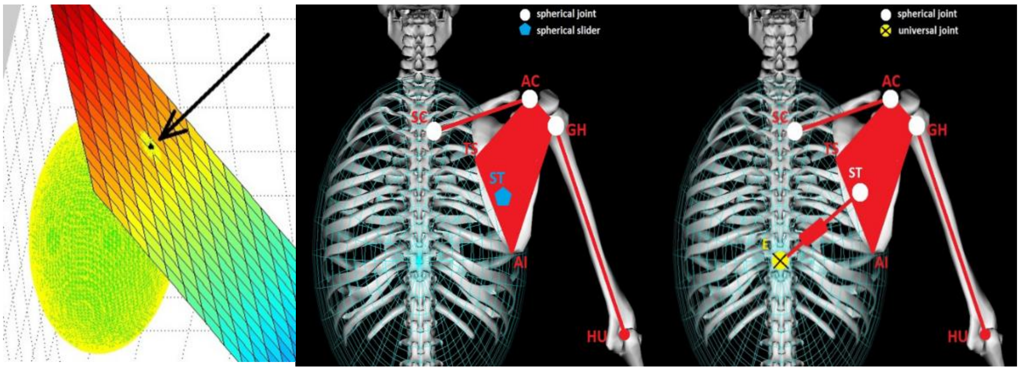

Figure 3-2: (a) The ellipsoid and plane intersection. (b) The ST point contact in the kinematic shoulder model. (c) The ST contact constraint is replaced by UPS link with passive prismatic joint. Images (b) and (c) were created using OpenSim model.

The forward kinematic analysis of the shoulder model provides a mapping between the nine Euler angles (ξ_1, ξ_2, ξ_3) at three joints SC, AC and GH and the pose of the end-effecter $P^0{}_{\mathrm{HU}}$ (the HU joint in Figure 3-2(b)) subject to one ST contact constraint. Applying the Grubler-Kutzbach criterion [147], the kinematic shoulder model, shown in Figure 3-2(b), has 8-DOFs.

$$n = 6(M - J - 1) + \sum_i F_i = 6 \cdot (4 - 4 - 1) + 3 \cdot 3 + 5 = 8 \qquad (3\text{-}7)$$

Here M is the number of links including the fixed base, J is the number of joints and F_i is their associated DOFs. There are three spherical ball-and-socket joints with 3-DOFs each and there is one constraint, defining the spherical slider joint with 5-DOFs. The self-rotations of the links SC-AC and GH-HU due to spherical joints at both ends introduce two redundant DOFs, called *passive DOFs*. Hence, the configuration of the end effector (HU joint) is defined by 6-DOFs. The shoulder kinematic model is redundant since the position of HU joint can be reached with more than one configuration of the shoulder bones. Note that, the axial rotation of the humerus is considered passive as the present work is focused only on the shoulder movement. The orientation of the humerus must be considered when modelling the elbow (hinge joint).

Further, the ST contact constraint can be replaced with an equivalent kinematic chain [128] comprising of universal joint at the center of the thorax ellipsoid E connected with the passive prismatic joint to a ball-and-socket joint at the ST point.

This additional kinematic chain (ST leg) provides an alternative method for construction of a forward kinematic map. As a result, there are two equivalent kinematic maps: one through the AC joint with ST contact (ellipsoid) constraint and one through ST joint with AC contact (spherical) constraint. For the alternative parallel kinematic map (through ST joint), additional sets of three Euler angles and two spherical angles are defined for the spherical joint at ST (δ_{ST}, υ_{ST}, φ_{ST}) and for the superimposed universal joint at E (α_{ST},β_{ST}) respectively. To parameterize the final configuration of the humerus (HU joint), two alternative sets of joint coordinates, AC map (natural) and ST map (parallel), can be used:

$$q_{AC} = (\xi_1^T\ \xi_2^T\ \xi_3^T)^T = (\delta_1\ \upsilon_1\ \varphi_1\ \delta_2\ \upsilon_2\ \varphi_2\ \delta_3\ \upsilon_3\ \varphi_3)^T \quad (3\text{-}8)$$

$$q_{ST} = (\xi_1(1)\ \alpha_{ST}\ \beta_{ST}\ \xi_{ST}^T\ \xi_3^T\ )^T = (\delta_1\ \alpha_{ST}\ \beta_{ST}\ \delta_{ST}\ \upsilon_{ST}\ \varphi_{ST}\ \delta_3\ \upsilon_3\ \varphi_3)^T \quad (3\text{-}9)$$

Four of the nine joint angles $(\varphi_1, \delta_3, \upsilon_3, \varphi_3)$ appear in both (3-8)-(3-9), the clavicle's axial rotation and three humeral Euler angles, that are unconstrained and mutually independent. The remaining two distinct sets of five joint coordinates correspond to the configuration of the scapula.

Consequently, the shoulder girdle can be represented as a 2-2 parallel mechanism, as shown in Figure 3-3, with the moving platform (scapula) supported by two spherical joints over two legs, one of which is of constant length (clavicle). The scapula is gliding on two surfaces, a sphere and an ellipsoid, through two point contacts: AC and ST. The Grubler-Kutzbach criterion states that the shoulder girdle, without the passive DOF associated with the clavicle's self-rotation, has 4-DOFs (3-10).

$$n = 6(M - J - 1) + \textstyle\sum_i F_i = 6 \cdot (4 - 4 - 1) + 3 \cdot 3 + 1 \cdot 2 - 1 = 4 \quad (3\text{-}10)$$

For the parallel shoulder girdle, there are two 3-DOFs spherical ball-and-socket joints on the top and one on the base, and there is one 2-DOFs universal base joint superimposed at the ellipsoid's center E. The prismatic joint in the introduced UPS kinematic chain (ST leg) is not considered as it depends on the universal joint's movement and cannot be actuated separately [128]. The 4-DOFs of the parallel platform correspond to two translational and two rotational DOFs of the scapula, namely: elevation/depression, abduction/adduction, upward/downward rotation and anterior/posterior tilting. The outer link (humerus bone) is serially connected on top of the moving platform through the ball-and-socket GH joint (as shown in

Figure 3-3) and its motion is described in terms of three Euler angles $(\delta_3, \nu_3, \varphi_3)^{\mathrm{T}}$. Now, the human shoulder can be represented as a hybrid mechanism consisting of a parallel shoulder girdle mechanism which orients and positions the serially connected humerus link.

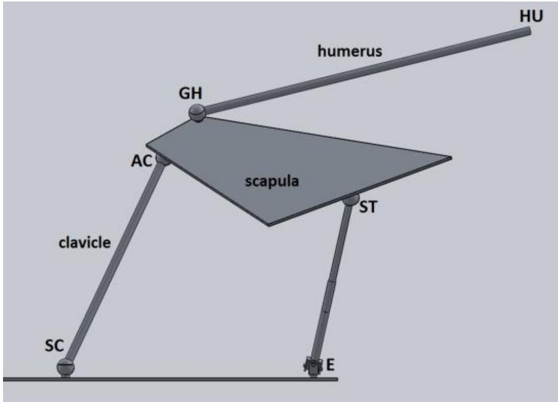

Figure 3-3: CAD design of the hybrid shoulder mechanism.

3.4 Modelling the human shoulder girdle as a 6-4 parallel mechanism

3.4.1 Minimal kinematic parameterization

In the previous section, similar to the model in [128], the scapula is parameterized by two alternative sets of five coordinates: (δ_1, ν_1, δ_2, ν_2, φ_2) and (α_{ST}, β_{ST}, δ_{ST}, ν_{ST}, φ_{ST}). However, as the shoulder girdle has 4-DOFs in the described model, four independent parameters or inputs are needed to fully express the configuration (position and orientation) of scapula. In order to obtain four independent variables to construct a minimal set of parameters, four additional UPS links with active prismatic joints are added to the shoulder girdle parallel platform, as shown in Figure 3-4. The new mechanism consists of 12 links: fixed base (thorax), moving platform (scapula), clavicle link, ST leg and 4 additional limbs consisting of two links each (due to the active prismatic joints). There are 16 joints in total: 6 spherical joints on the moving platform, 5 universal joints and 1 spherical joint on the base, and 4 prismatic joints in the added limbs. In fact, adding an additional UPS link does not alter the total number of DOFs of the spatial manipulator because each UPS link is a complete set of 6-DOFs. It can be verified using the mobility formula (3-11) as follows:

$$n = 6(M - J - 1) + \sum_i F_i = 6 \cdot (12 - 16 - 1) + 7 \cdot 3 + 5 \cdot 2 + 4 - 1 = 4 \qquad (3\text{-}11)$$

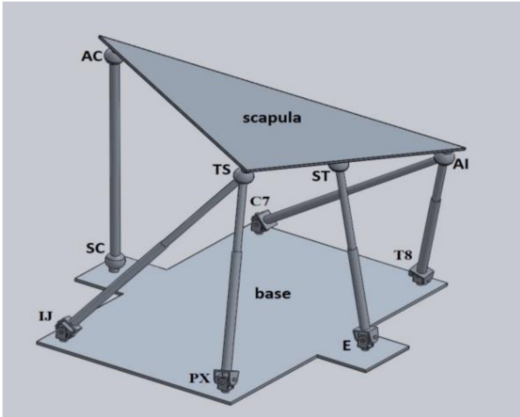

Figure 3-4: The human shoulder girdle modelled as a 6-4 parallel mechanism.

Thus, the modified parallel mechanism still possesses only 4-DOFs. In contrast, an additional universal-spherical (US) link which has 5-DOFs will reduce the total number of DOFs of the mechanism by one. Note that, as in the previous Section, the passive DOF associated with the clavicle's self-rotation is subtracted and passive prismatic joint in the ST leg is not considered. Moreover, it is also apparent that newly added UPS limbs can be also replaced by SPS limbs without compromising the overall DOFs of the mechanism as the passive DOFs associated with SPS limbs will also be subtracted from the DOF equation. The modified parallel mechanism describing shoulder girdle movement is now modelled as a 6-4 parallel mechanism. Two additional UPS links meet at concentric spherical joints on the mobile platform (scapula) at the bony landmark TS and the other two additional UPS links meet the same way at the scapula landmark AI. The four additional active limbs provide us with four independent inputs in terms of the lengths *d* of these links. The four links' offsets can be varied independently and are equal to the number of the DOFs of the model.

Due to a special variation of this parallel mechanism, like having constrained links and concentric spherical joints on the top platform, once the lengths of the four additional UPS links are given ($\mathrm{d}_1\ \mathrm{d}_2\ \mathrm{d}_3\ \mathrm{d}_4$), the configuration of the moving platform can be found through the forward kinematics analysis as shown further in this Section.

Consequently, both forward kinematic maps (natural and parallel) described in Section 3.2 can be parameterized in terms of the following vector of eight minimal coordinates:

$$q_{min} = \left(\xi_1(1)\ \mathrm{d}_1\ \mathrm{d}_2\ \mathrm{d}_3\ \mathrm{d}_4\ {\xi_3}^T\right)^T = \ (\delta_1\ \mathrm{d}_1\ \mathrm{d}_2\ \mathrm{d}_3\ \mathrm{d}_4\ \delta_3\ v_3\ \varphi_3)^T \qquad (3\text{-}12)$$

3.4.2 Geometry description and kinematics of the 6-4 parallel shoulder girdle mechanism

The parallel mechanism of the human shoulder girdle, shown in Figure 3-4, consists of a moving platform (scapula), whose plane is defined using three scapula bony landmarks (AC, TS, and AI), connected to a base platform (thorax) using six limbs: one limb has a constant length and represents the clavicle, one of the limbs with a variable length represents ST contact and modelled as a UPS link with *passive* prismatic joint and the other four links with variable lengths are modelled as UPS links with *active* prismatic joints. The four additional universal joints on the base are placed at the defined bony landmarks of the thorax (refer to Figure 3-1) to give them real anatomical basis. Thus, the fixed inertial coordinate system (with subindex 0) defined in Section 3.2 is placed at the base joint of the mechanism (at IJ). Ideally, the four additional base joints (placed at IJ, P8, TX and C7) lie on one plane, called sagittal plane, which divides the human body into left and right sides. The initial two base joints, placed at SC joint and at the center of the ellipsoid E, obviously, do not belong to that plane. The model in Figure 3-4 is just a simplified representation of the proposed mechanism.

The coordinate frame of the moving platform (with subindex 2) is attached at AC joint as defined in Section 3.2 (Figure 3-1). Therefore, the position and orientation of the moving platform (scapula) with respect to the base (thorax) is described by the 4×4 homogeneous transformation matrix $\mathbf{T}$ which consists of a 3×3 rotation matrix $\mathbf{R_2}$ of the moving platform and a 3×1 position vector P_2^0 of the AC joint expressed in the inertial frame. Vectors SC^0, PX^0, $T8^0$,$C7^0$, E^0, TS^2 and AI^2 have constant lengths defined by the dimensions of the shoulder model.

The length of the each limb can be found by taking the dot product of the vector along the limb with itself:

$$\mathrm{d}^2 = [P_2^0 - SC^0]^T[P_2^0 - SC^0], \qquad \text{for clavicle limb SC-AC} \qquad (3\text{-}13)$$

$$\mathrm{d}_1^2 = [P_2^0 + \mathbf{R_2}TS^2]^T[P_2^0 + \mathbf{R_2}TS^2], \qquad \text{for UPS limb IJ-TS} \qquad (3\text{-}14)$$

$$\mathrm{d}_2^2 = [P_2^0 + \mathbf{R_2}TS^2 - \ PX^0]^T[P_2^0 + \mathbf{R_2}TS^2 - \ PX^0], \quad \text{for UPS limb PX-TS} \qquad (3\text{-}15)$$

$$\mathrm{d}_3^2 = [P_2^0 + \mathbf{R_2}AI^2 - \ C7^0]^T[P_2^0 + \mathbf{R_2}AI^2 - \ C7^0], \quad \text{for UPS limb C7-AI} \qquad (3\text{-}16)$$

$$d_4^2 = [P_2^0 + \mathbf{R_2} AI^2 - T8^0]^T [P_2^0 + \mathbf{R_2} AI^2 - T8^0], \quad \text{for UPS limb T8-AI} \qquad (3\text{-}17)$$

$$d_{ST}^2 = [P_2^0 + \mathbf{R_2} ST^2 - E^0]^T \mathbf{E}_{\mathrm{ST}} [P_2^0 + \mathbf{R_2} ST^2 - E^0] - 1 = 0, \quad \text{for ST leg} \qquad (3\text{-}18)$$

Here $\mathbf{E}_{\mathrm{ST}} = \begin{bmatrix} \frac{1}{a^2} & 0 & 0 \\ 0 & \frac{1}{b^2} & 0 \\ 0 & 0 & \frac{1}{c^2} \end{bmatrix}$ a, b, c - are the ellipsoid half-axis dimensions

The set of equations (3-13)-(3-18) yields six equations describing the pose of the moving platform (scapula) with respect to the fixed base (thorax). It can be seen that the inverse kinematics of such mechanism is simple and gives a unique solution. Given the configuration of the moving platform ($\mathbf{R_2}$ and P_2^0**),** the lengths of the links can be found by taking the square root of the above expressions. Thus, there are two possible solutions for the link length. However, only the positive link length is physically feasible and if the solution is a complex number, the configuration of the top platform (scapula) is not reachable.

In contrast to inverse kinematics, forward kinematic (FK) analysis of this kind of parallel mechanism is a challenging task. For a given set of limb lengths, one needs to find the configuration of the moving platform. As stated before, the orientation and position of the moving platform (scapula) can be described using rotation matrix $\mathbf{R_2}$ and position vector P_2^0 that contain nine and three scalar unknowns, respectively. There exist different approaches and methods to solve this problem that involves highly nonlinear equations which will lead to multiple solutions.

Nevertheless, in comparison to rotation matrix $\mathbf{R_2}$ and position vector P_2^0, the Cartesian coordinates (x, y, z) of any three points on the scapula (say AC, TS and AI) expressed in the inertial frame can also fully define the pose of the scapula with respect to the thorax. Then, defining the spatial configuration of all the joints with respect to each other and to the origin (excluding the ST contact point for the moment) will give 8 quadratic equations with 9 unknowns (x, y, z coordinates of 3 moving points). As the location of the ST contact point on the scapula plane is unknown, one ellipsoid constraint equation will add another 3 unknowns (x, y, z coordinates of the ST contact) resulting in the system of 9 equations with 12 unknowns. In fact, the ST contact point that belongs to the scapula plane can be used to derive additional three equations. As the ST contact belongs to the scapula plane, its coordinates can be expressed in terms of the coordinates of the other three points on the scapula (TS, AI and AC). In other words, the coordinates of the ST contact point are functions of the coordinates of the other three scapula points. The vectors that extend from the ST contact point to any of the other three vertices of the scapula triangle are perpendicular to the vector normal to the scapula plane. In other words, the dot products between these vectors and the normal vector must be zero. In turn, the vector normal to the scapula plane can be found using the cross product of any two vectors that connect all three vertices of the scapula triangle as follows:

$$N^0 = (AI^0 - AC^0) \times (TS^0 - AC^0) \tag{3-19}$$

Finally, the system of 12 equations with 12 unknowns (x, y, and z coordinates of four points) to solve FK is derived as follows (3-20). Referring to Figure 3-4:

$$\mathbf{F}(\lambda, x) = \begin{bmatrix} (\mathrm{X_{AC}} - \mathrm{X_{SC}})^2 + (\mathrm{Y_{AC}} - \mathrm{Y_{SC}})^2 + (\mathrm{Z_{AC}} - \mathrm{Z_{SC}})^2 - \mathrm{d}^2 \\ (\mathrm{X_{TS}})^2 + (\mathrm{Y_{TS}})^2 + (\mathrm{Z_{TS}})^2 - \mathrm{d}_1^2 \\ (\mathrm{X_{TS}} - \mathrm{X_{PX}})^2 + (\mathrm{Y_{TS}} - \mathrm{Y_{PX}})^2 + (\mathrm{Z_{TS}} - \mathrm{Z_{PX}})^2 - \mathrm{d}_2^2 \\ (\mathrm{X_{AI}} - \mathrm{X_{C7}})^2 + (\mathrm{Y_{AI}} - \mathrm{Y_{C7}})^2 + (\mathrm{Z_{AI}} - \mathrm{Z_{C7}})^2 - \mathrm{d}_3^2 \\ (\mathrm{X_{AI}} - \mathrm{X_{T8}})^2 + (\mathrm{Y_{AI}} - \mathrm{Y_{T8}})^2 + (\mathrm{Z_{AI}} - \mathrm{Z_{T8}})^2 - \mathrm{d}_4^2 \\ \frac{(\mathrm{X_{ST}} - \mathrm{X_E})^2}{\mathrm{a}^2} + \frac{(\mathrm{Y_{ST}} - \mathrm{Y_E})^2}{\mathrm{b}^2} + \frac{(\mathrm{Z_{ST}} - \mathrm{Z_E})^2}{\mathrm{c}^2} - 1 \\ (\mathrm{X_{TS}} - \mathrm{X_{AC}})^2 + (\mathrm{Y_{TS}} - \mathrm{Y_{AC}})^2 + (\mathrm{Z_{TS}} - \mathrm{Z_{AC}})^2 - \mathrm{L}_1^2 \\ (\mathrm{X_{AI}} - \mathrm{X_{AC}})^2 + (\mathrm{Y_{AI}} - \mathrm{Y_{AC}})^2 + (\mathrm{Z_{AI}} - \mathrm{Z_{AC}})^2 - \mathrm{L}_2^2 \\ (\mathrm{X_{AI}} - \mathrm{X_{TS}})^2 + (\mathrm{Y_{AI}} - \mathrm{Y_{TS}})^2 + (\mathrm{Z_{AI}} - \mathrm{Z_{TS}})^2 - \mathrm{L}_3^2 \\ \mathrm{X_N} \cdot (\mathrm{X_{ST}} - \mathrm{X_{AC}}) + \mathrm{Y_N} \cdot (\mathrm{Y_{ST}} - \mathrm{Y_{AC}}) + \mathrm{Z_N} \cdot (\mathrm{Z_{ST}} - \mathrm{Z_{AC}}) \\ \mathrm{X_N} \cdot (\mathrm{X_{ST}} - \mathrm{X_{AI}}) + \mathrm{Y_N} \cdot (\mathrm{Y_{ST}} - \mathrm{Y_{AI}}) + \mathrm{Z_N} \cdot (\mathrm{Z_{ST}} - \mathrm{Z_{AI}}) \\ \mathrm{X_N} \cdot (\mathrm{X_{ST}} - \mathrm{X_{TS}}) + \mathrm{Y_N} \cdot (\mathrm{Y_{ST}} - \mathrm{Y_{TS}}) + \mathrm{Z_N} \cdot (\mathrm{Z_{ST}} - \mathrm{Z_{TS}}) \end{bmatrix} = \mathbf{0} \tag{3-20}$$

The system of equations (3-20) is a set of fundamental equations that has 12 polynomial equations with a highest order of 2, where $\lambda = [X_{AC} Y_{AC} Z_{AC} X_{TS} Y_{TS} Z_{TS} X_{AI} Y_{AI} Z_{AI} X_{ST} Y_{ST} Z_{ST}]^T$ is the 12-dimensional output vector of the unknowns and $x = [\mathrm{d}_1 \mathrm{d}_2 \mathrm{d}_3 \mathrm{d}_4]^T$ is the four-dimensional input vector of the link lengths variables. Other symbols in (3-20) represent constant values. Note that, if the base points IJ, P8, TX and C7 lie on one plane, their z-components become zero. This system of equations incorporates ellipsoid constraint and allows the ST contact to move on the scapula plane. Thus, the input values $x = [\mathrm{d}_1 \mathrm{d}_2 \mathrm{d}_3 \mathrm{d}_4]^T$ that solve (3-20) can be referred as the minimal coordinates that incorporate the ST constraint. Such systems of highly nonlinear equations can be solved using different analytical methods [146-149]. This can result in a number of possible forward kinematic solutions. However, a numerical iteration method with the appropriate initial guess vector can be applied to find the current forward kinematic solution of the moving platform that lies in the same branch of solutions as the initial configuration of the parallel platform [149]. Note that, if the location of the ST contact point is predefined and fixed on the scapula plane, the system of equations will be simplified to a system of 9 equations with 9 unknowns. A derivation of the closed-form expression is considerably simplified for this case.

Once the Cartesian coordinates (in inertial frame) of three points (AC, TS and AI) on the scapula are found, the orientation matrix $\mathbf{R_2}$ and position vector P_2^0 can be derived as follows:

- The unit vector along the vector TS-AC is the 3rd column of matrix $\mathbf{R_2}$

$$\mathbf{R_2}(:,3) = (\frac{\mathrm{X_{AC}}-\mathrm{X_{TS}}}{\mathrm{L_1}}, \frac{\mathrm{Y_{AC}}-\mathrm{Y_{TS}}}{\mathrm{L_1}}, \frac{\mathrm{Z_{AC}}-\mathrm{Z_{TS}}}{\mathrm{L_1}}) \tag{3-21}$$

- The unit vector along the cross product of vectors TS-AC (u) and TS-AI (w) is the 1st column of matrix $\mathbf{R_2}$

$$\mathbf{R_2}(:,1) = (\frac{(u_y w_z - u_z w_y)}{|(u \times w)|}, \frac{(u_z w_x - u_x w_z)}{|(u \times w)|}, \frac{(u_x w_y - u_y w_x)}{|u \times w|}) \tag{3-22}$$

- The 3rd unit vector that can be found as the cross product of the above two is the 2nd column of matrix $\mathbf{R_2}$.

$$\mathbf{R_2}(:,2) = \mathbf{R_2}(:,3) \times \mathbf{R_2}(:,1) \tag{3-23}$$

The position vector $P_2^0 = (\mathrm{X_{AC}}, \mathrm{Y_{AC}}, \mathrm{Z_{AC}})$ is derived from the Cartesian coordinates of the AC joint. It can be seen that, in all cases, the input set of link lengths (d_1, d_2, d_3, d_4) is directly related to the transformation matrix (rotation matrix $\mathbf{R_2}$ and position vector P_2^0) which, in turn, contains all the shoulder girdle joint angles, described in Section 3.2.

Once the configuration of the moving platform is known, any point, for instance GH joint, defined in scapula's coordinate frame (subindex 0) can be found as follows:

$$GH^0 = P_2^0 + \mathbf{R_2} GH^2 \tag{3-24}$$

3.5 Shoulder motion planning with the proposed mechanism

As stated in Section 3.2, the kinematic model of the human shoulder is redundant: there exist multiple sets of joint angles for a given pose of the upper arm. The motion planning in musculoskeletal shoulder models is a challenging task due to the presence of the ST constraint(s). When constraints are not considered, the kinematic model's nine joint angles (q) are independent and can be ascribed the values of the measured angles (q_m). When constraints are considered, the joint coordinates become interdependent and the motion planning requires data-driven optimization to minimize the error between the model's coordinates q and the measured values of the coordinates q_m at discrete instances of the motion [131, 138, 143, 150-152]. Thus, this kind of approach requires the availability of the measured data to solve the optimization problem at every instant of the movement. The minimal coordinates presented in this work are independent from each other and, when used to solve (3-20), incorporate the constraints. Hence, if measured movement is expressed in terms of the proposed minimal coordinates it can be directly imposed on the model.

In this section the proposed model is used for humeral abduction (from 0° to 160°) in the scapular plane. The method of planning the model's kinematics is adapted from [150] but it is now applied to the proposed shoulder model with one ST contact constraint utilizing a novel set of minimal coordinates presented in the previous Section. The independent variables $\mathrm{d}_1, \mathrm{d}_2, \mathrm{d}_3$ and d_4 parameterise shoulder girdle motion and are equivalent to the five joint angles ($\delta_1 \upsilon_1 \delta_2 \upsilon_2 \varphi_2$). First, the motion is planned in terms of the minimal coordinates q_{min} and constructed in terms of $q_{min}(t)$ which is then mapped back to $q(t)$. Using the shoulder girdle minimal coordinates, the spatial locations of the scapula points can be found and the joint angles can be extracted from the rotation matrices $\mathbf{R_1}$ and $\mathbf{R_2}$ knowing their sequence of rotation.

The time-dependent parameterization of the minimal coordinates is defined using the dataset from the literature [131] that contains positions of all the required anatomical landmarks and the dimensions of the ellipsoid. The minimal set of coordinates $q_{min}(t)$ is planned corresponding to the description of humeral abduction in [150]. From 30° to 160° abduction, the shoulder girdle's parameters are planned as a linear function of time. The clavicle's axial rotation coordinate δ_1 is held constant during the first 30° humeral abduction and then rotated posteriorly by 40° using a linear function of time. In order to simulate the arm abduction in the scapular plane the GH joint angles δ_3 and φ_3 are held constant at 0° and 30° whereas the third glenohumeral angle v_3 is planned using a linear function of time.

$$\varphi_1(t) = \begin{cases} 0^\circ & t \in [0, \frac{30}{160}] \\ 0^\circ + 40^\circ t, & t \in [\frac{30}{160}, 1] \end{cases} \tag{3-25}$$

$$\mathrm{d}_i(t) = \begin{cases} \mathrm{d}_i(0) & t \in [0, \frac{30}{160}] \\ \mathrm{d}_i(0) + \big(\mathrm{d}_i(1) - \mathrm{d}_i(0)\big)t, & t \in [\frac{30}{160}, 1] \end{cases} \qquad i = 1 - 4 \tag{3-26}$$

$$\delta_3(t) = 0^\circ, \quad v_3(t) = 0^\circ + 160^\circ t, \quad \varphi_3(t) = 30^\circ, \quad t \in [0,1] \tag{3-27}$$

As the minimal coordinates presented in this work are defined as the distances between the main anatomical landmarks, the initial values $d_1(0)$, $d_2(0)$, $d_3(0)$ and $d_4(0)$ are obtained from the existing dataset of the bony landmarks (Table 2 in [151]). The values $d_1(1)$, $d_2(1)$, $d_3(1)$ and $d_4(1)$ are set according to the measured final pose of the shoulder at 160◦ humeral abduction. The values $d_1(t)$, $d_2(t)$, $d_3(t)$ and $d_4(t)$ are calculated using equations (3-26) for t = 0°, 45°, 90°, 120°, 140° and 160°. These sets of four minimal coordinates (d_1, d_2, d_3, d_4) are used as inputs in (3-20) to obtain the spatial locations of the scapula landmarks AC, TS, AI and ST at each instant of the movement. (3-20) is solved in MATLAB using *fsolve* function with the initial guess vector (initial coordinates of the scapula landmarks). The initial estimate of the ST contact is chosen to be the centroid of the scapula plane. Once the geometric location of the three scapula points AC, TS and AI is obtained, the rotation matrix $\mathbf{R}_2$ is constructed using (3-21)-(3-23). To be consistent with the ISB recommendations [35] where the scapula reference frame is defined using the scapula landmark AA, the spatial coordinate of this point is found using (3-24). The new rotation matrix $\mathbf{R}_2^*$ is then constructed from the scapula points AC, TS and AA. Finally, the scapula joint angles are extracted from the rotation matrix using inverse trigonometric functions knowing that the sequence is Y-X-Z, as stated earlier in Section 3.2. The obtained scapular angles during the humeral abduction are shown in Figure 3-5.

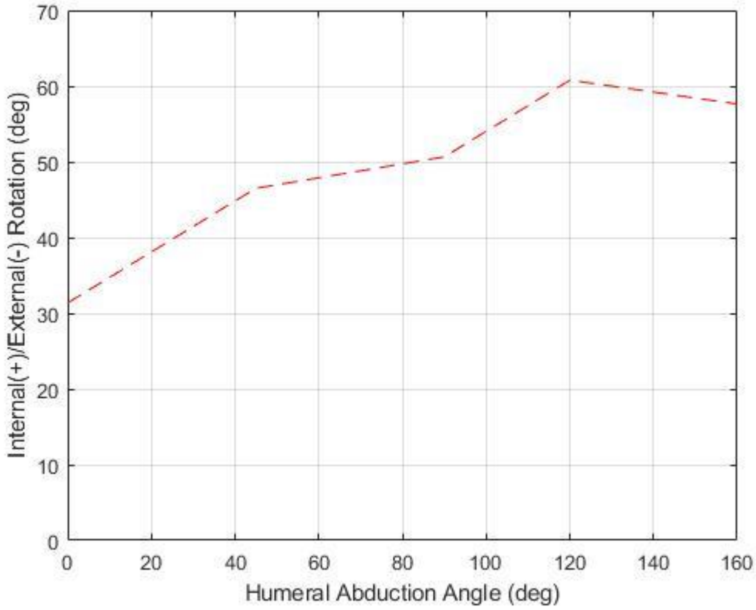

(a)

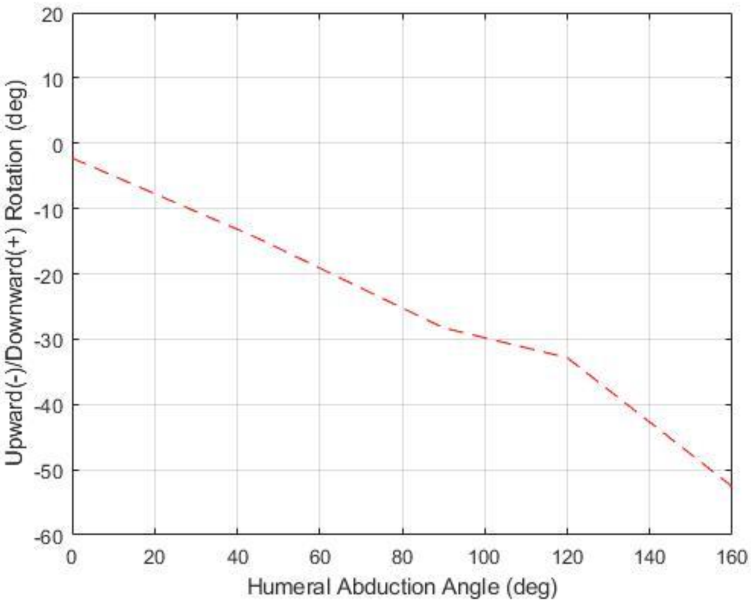

(b)

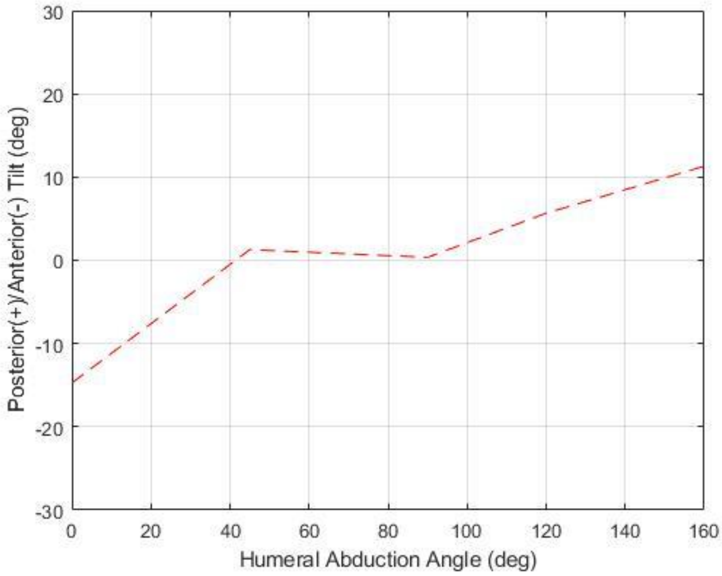

(c)

Figure 3-5: Scapular joint angles during humeral abduction. (a) Scapular internal rotation, υ_2. (b) Scapular upward rotation, δ_2. (c) Scapular posterior tilting, φ_2.

At 0° humeral abduction (initial position), the scapula is rotated internally 31°, upwardly 2° and tilted anteriorly 14°. At 160° humeral abduction (final position), the scapula is rotated internally 57°, upwardly 52° and tilted posteriorly 11°. Hence, the scapula is internally and upwardly rotated and posteriorly tilted during humeral abduction. The largest change (50°) between the initial and final values is shown by the upward rotation angle (Figure 3-5(b)). Despite the recommendations set by ISB for the shoulder, the direct comparison between the existing studies in the literature is problematic due to the methodologic differences: definition of the initial position, orientation of the coordinate systems, Euler angle sequences, geometrical parameters, variability in marker placement, etc. In this study, the choice of the initial guess vector can also affect the numerical calculations. Nevertheless, the general course of the computed scapula joint angles in the presented work is in agreement with the literature [131, 153-155].

The movement of the ST contact point during humeral abduction on a scapula plane (defined by points AC, TS and AI) is shown with arrow in Figure 3-6. The ST contact point has been close to the center of the scapula plane and moved only 16.65 mm during full humeral abduction. This seems to support the study in [155] where it has been found that the center of the inner scapular plane had small deviations in distance and angle with respect to the thorax. The presented shoulder motion planning case and the tracking of the moving ST articulation can be considered as an evaluation of the effectiveness of the proposed parallel mechanism for the human shoulder girdle.

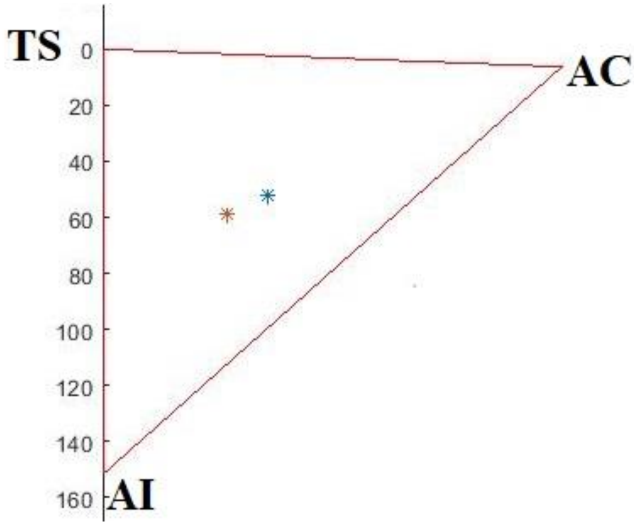

Figure 3-6: The movement of the ST contact (from blue to red) during humeral abduction (from 0° to 160°) on a scapula plane.

3.6 Discussion and Conclusion

As stated earlier, the contact between the scapula bone and thorax, which is not a joint in anatomical sense, complicates the shoulder kinematics and introduces the constraints to the existing shoulder biomechanical models. In fact, the shoulder models become less reliable when the ST constraints are not considered [138]. To simplify the shoulder motion planning and remove the interdependencies between the joint coordinates, minimal parameterization in terms of independent variables, which incorporate the model constraints and are equal to the number of DOFs, is needed. The advantages of using the minimal coordinates for the shoulder motion planning are introduced in [128] where three sets of 7 minimal coordinates (three of which are for the shoulder girdle) were derived for a 7-DOFs shoulder model with two ST contact constraints. In order to construct the dynamic model, one needs to map the minimal coordinates back to the joint angle parameterization as the kinematic chains defined to model the ST contact points would cause the physical inconsistencies such as a tensile force in the scapula whereas there is only a compressive one.

The single ST contact point model used to describe the ST articulation in this work led to the kinematic shoulder model with 8-DOFs, four of which correspond to the shoulder girdle. After replacing the single ST contact constraint with the equivalent kinematic chain the pose of the humerus is parameterized using two alternative forward kinematic maps. It has been then shown that, adding redundant UPS links with active prismatic joints to the 2-2 parallel mechanism does not alter the number of DOFs of the mechanism. Moreover, the variable link lengths of these additional kinematic chains that are independent of each other and are equal to the number of DOFs can serve as the minimal set of input parameters for the shoulder girdle parallel mechanism. Thus, in contrast to the 3 sets of minimal coordinates proposed in [128], a single common set of minimal coordinates for both forward kinematic maps is presented in this work. Indeed, the idea of adding redundant parallel kinematic links to the closed kinematic chains can be generalized and the approach presented in this work could form the basis of a general methodology of formulating parameterizations of kinematic models with closed kinematic chains.

Consequently, the human shoulder girdle is modelled as a 6-4 parallel mechanism. In fact, the geometry of the additional attachment points on the base could be adjusted in different ways, e.g. in case when two base joints are placed at one concentric joint on the base the structure of the parallel mechanism will be described as 5-4. However, the shifts in joint locations will not change the kinematic properties of the mechanism. The choice of the real bony landmarks for the base joints is made to facilitate the application of the model in the studies of the shoulder kinematics. The detailed kinematic analysis of the proposed parallel mechanism is carried out to provide more insight on kinematic characteristics of the human shoulder. It might be claimed that the feasible mechanical system can be constructed with similar kinematic characteristics to those of the human shoulder girdle. The equations of FK present a novel approach to estimate the spatial configuration of the scapula allowing the gliding motion of the ST contact point while respecting the surface constraint. In addition, the proposed shoulder girdle mechanism can be used to track the ST contact motion during a given shoulder movement which opens a new prospect in shoulder biomechanics. Also, a moving ST contact point could improve the prediction of muscular moment arms providing more anatomically real musculoskeletal models [138]. Another advantage of the proposed parallel mechanism is that it could be adapted to examine pathological cases, e.g. “winging” scapula, by locating the ST contact point further away from the medial border. In that case, the medial border of the scapula will be able to lift off the thorax surface.

The case study on shoulder motion planning shows that the proposed model can be used to predict shoulder kinematics during a given movement. The existing methods to predict shoulder motions use minimization with respect to measured kinematics or regression models which do not consider the kinematic constraints. The advantage of the proposed model is that it directly incorporates the moving ST contact constraint and simplifies the motion planning without the need of the measured data at every instant of time. In this regard, the proposed method of shoulder motion planning using the independent minimal coordinates can be used to correct the limitations of the regression models and this opens another appealing perspective. Moreover, the presented minimal coordinates parameterize the movement of bony landmarks and are apparently applicative for skin marker palpation techniques. The simplicity with which they can be applied also makes them attractive. A closed-form solution of (3-20) can give more insight on the kinematic properties of the shoulder girdle mechanism. The forces in the actuated limbs in the shoulder girdle parallel mechanism can be regarded as resultant forces from the shoulder muscles acting on the scapula as the number of the shoulder muscles involved in the upper limb motions is much greater than the shoulder DOFs.

To sum up, the human shoulder girdle can be considered as a closed kinematic chain considering the contact between the scapula and thorax and modelled as a parallel mechanism. The kinematic model of the human shoulder in this chapter is based on the model with one point ST contact constraint which makes the human shoulder girdle a 4-DOFs parallel mechanism. It is shown that, by imposing additional kinematic chains that do not change the number of DOFs, the shoulder girdle can be modelled as a 6-4 parallel mechanism. Moreover, the redundant link lengths can provide the minimal set of independent coordinates and can be used to facilitate the shoulder motion planning while abiding by the moving ST joint constraint. Thus, the results of this chapter contributes to the biomechanical analysis of the human shoulder and can be applied to further investigate the complex coupled motion of the most mobile multi-joint of the human body.

Chapter 4

Kinematic Modelling of Hybrid Human-Robot Mechanism

4.1 Introduction

In order to contribute to the solution of the human–robot compatibility issue, this chapter presents the kinematic modeling and analysis of a novel bio-inspired 5-DOFs hybrid human–robot mechanism (*HRM*). The proposed hybrid mechanism combines serial and parallel manipulators with rigid and cable links enabling a match between human and exoskeleton joint axes. Section 4.2 provides the background to the kinematic modelling of the hybrid mechanism. Section 4.3 describes the overall structure of the proposed hybrid mechanism and provides complete kinematic modelling including the derivation of unified and decoupled Jacobian matrices. Section 4.4 covers comprehensive singularity and workspace analysis of the proposed human-robot shoulder mechanism. The numerical and simulation results from CAD and 3D model of the physical mechanism are presented to validate the kinematic model. Section 4.5 presents the tension optimization in the cable-driven module with the numerical example.

4.2 Background

To address the kinematic incompatibility between the human and robot structure, numerous groups of researchers have designed and built different robotic devices with various mechanical advancements for shoulder complex rehabilitation, as presented in Chapter 2. A few of them consider and assist the shoulder girdle motions as summarized in Section 2.4. However, the rigid serial structures, extra actuators and complex configurations in these robotic shoulder devices make them heavy, large and expensive which in turn hinder their use in clinical set ups. To reduce the weight of the exoskeleton structure and load on upper limb segment, a lightweight cable-driven parallel mechanism (*CDPM*) has been proposed for upper limb rehabilitation [39]. The rigid links are replaced by unilateral cables and their parallel placement. This not only exhibits lower effective inertia and compactness but also resolves the misalignment issue with the shoulder joint. Despite its advantages over the rigid links devices, the cable-driven exoskeleton in [39] does not consider assistance of the shoulder girdle movements which limits its overall workspace and functionality. Therefore, in order to have complete kinematic compatibility between the human and exoskeleton structure, the mechanism design of the actuated robotic exoskeleton must cover all individual DOFs of the human shoulder, which remains a major challenge in the development of the shoulder rehabilitation exoskeletons [18].

In fact, the coupled structure of the robotic exoskeleton firmly connected to the human limbs is kinematically equivalent to an actuated manipulator, serial or parallel, with the additional inner passive restrained limbs that govern the number of DOFs of the manipulator and remove its redundant self-motion. Kinematics of the constrained parallel manipulators (*cPM*s) has been studied in the literature [156, 157], where the overall Jacobian matrix of such mechanisms depends not only on the Jacobian of the actuated legs but also on the restrained passive leg [158]. Moreover, it has been shown that the optimized design of the *cPM* possesses better kinematic characteristics, such as higher global condition index, larger workspace volume and better conditioned stiffness matrix, than that of the unconstrained manipulator [159]. The well-studied planar or spatial four-bar linkages, e.g. inverted slider crank mechanisms, can also be considered as constrained mechanisms (*cM*s) because the passive following link limits the motion of the driving linkage [160].

In this chapter, we apply and expand the kinematic analysis of constrained mechanisms to the exoskeleton application in order to solve the human-robot compatibility issues. The complex motions of a 4-DOFs human shoulder girdle, which has been modelled as a 6-4 parallel mechanism in Chapter 3, is usually simplified to a 2-DOFs as stated in Section 2.3. Thus, a 2-DOFs shoulder girdle model has been used in a proposed mechanism. In particular, the robotic exoskeleton coupled with the human shoulder is designed as a 5-DOFs *HRM* that comprises a 2-DOFs proximal *cM* serially connected to a 3-DOFs distal constrained *CDPM* module, corresponding to the shoulder girdle and the spherical shoulder joint, respectively. The DOFs of sub-mechanisms are dependent on the inner restrained passive limbs' (shoulder) DOFs. The hybrid structure of the mechanism consists of both serial and parallel links merging the advantages of both types of manipulators: increased overall workspace and rigidity [161, 162]. The load carrying capacity of the proximal module is enhanced with the inner passive limb and with the reduced weight of the parallel module due to its lightweight cable-driven links. The distal *CDPM* module is designed as a fully constrained spherical cable-driven mechanism with four actuated cables, similar to *CDPM*s in [39, 163]. Even though it implies actuation redundancy, the proper placement of the cable attachment points on both platforms of the designed *CDPM*, helps not only to fully control the motion and change the distribution of the cable tensions, but also to avoid singularities, enlarge the workspace and facilitate the forward kinematic problem of the parallel module. The study proposes the use of a cable-driven mechanism as it provides smooth and quite transmissions which are highly desirable for rehabilitation exoskeletons, does not restrict the natural motion of the human upper arm and reduces the overall weight of the mechanism as all the actuation units can be placed on the fixed support frame. Moreover, as the actuation of the human shoulder is achieved by parallel action of the shoulder muscles, cable-driven parallel mechanism can be considered as a bio-inspired design to conform to the anatomy of upper arm. The 2-DOFs rigid-link proximal module not only covers the essential DOFs of the human shoulder girdle but also further increases the overall workspace and functionality of the coupled hybrid *HRM*.

As the proposed *HRM* is designed based on kinematic analysis of *cM*s, it ensures the avoidance of joint axes misalignments between the human and robot links, improving human-robot compatibility. The hybrid combination of the active shoulder girdle rigid mechanism and *CDPM* significantly increases the ranges of motions of the designed shoulder exoskeleton and reduces the overall weight of the structure. In this chapter, numerical results are provided to demonstrate that the *HRM* is free of singularities within the workspace of the human shoulder. The advantageous characteristics of the proposed mechanism make it suitable for safe human-robot interaction where an intrinsically compliant robotic exoskeleton with lightweight modules is highly desirable.

4.3 Kinematic Modelling of the HRM

The three Cartesian Coordinate Systems (CS_0, CS_1 and CS_2) with the X_0, Y_0, Z_0, X_1, Y_1, Z_1 and X_2, Y_2, Z_2 axes, respectively, are defined to model the kinematics of the proposed hybrid mechanism, as shown in Figure 4-1. The inner restraining link L_1

of the proximal sub-mechanism is attached to the fixed base through the passive universal joint (*P* joint) on one end and serially connected to the restraining link L_2 of the distal module through the passive spherical joint (*S* joint) on the other end. Note that, when this mechanism is later applied to the human shoulder, L_1 and L_2 are the modelled links for the human clavicle and humerus, respectively.

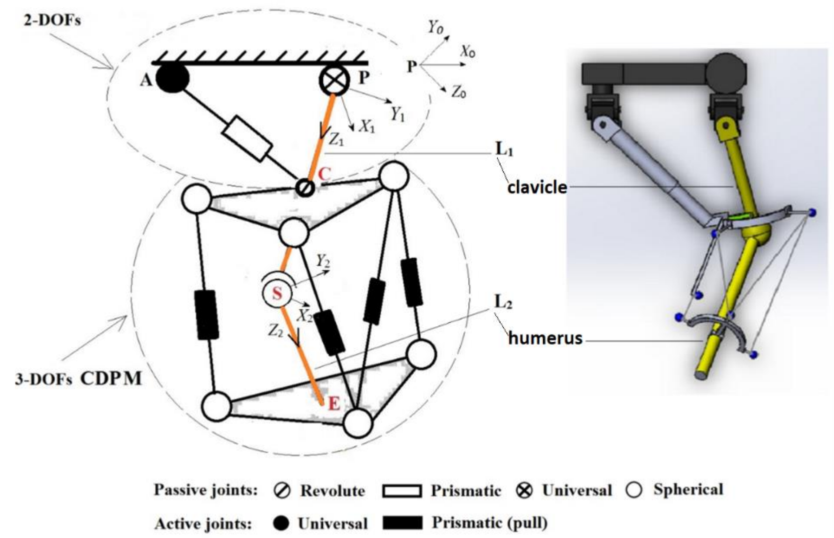

Figure 4-1: The kinematic structure of the *HRM* with the inner restrained linkage: kinematic model (left), CAD model (right).

To facilitate the analysis, the inertial fixed reference frame CS_0, is placed at the centre of the *P* joint with X_0-axis pointing along the fixed base link, Y_0-axis pointing upwards and Z_0-axis perpendicular, respectively. The origin of the first moving frame CS_1 is also attached to the *P* joint with its Z_1-axis along the moving link L_1, and the second moving frame CS_2 is attached to the centre of the passive spherical joint (*S* joint) with its Z_2-axis along the link L_2. For analysis purposes, the axes of the coordinate systems are aligned at the initial configuration.

The orientation matrices between the defined frames are obtained using orientation angles, namely *X*-*Y* and *Y*-*X*-*Y* rotation sequences of the *P* joint angles (θ_1, θ_2) and S joint angles (α, β, γ), respectively (with *c* – cos and *s* – sin):

$$\mathbf{R}_1^0 = \mathbf{R}_{X_1}(\theta_1)\mathbf{R}_{Y_1}(\theta_2) = \begin{bmatrix} c\theta_2 & 0 & s\theta_2 \\ s\theta_1 s\theta_2 & c\theta_1 & -c\theta_2 s\theta_1 \\ -c\theta_1 s\theta_2 & s\theta_1 & c\theta_1 c\theta_2 \end{bmatrix} \tag{4-1}$$

$$\mathbf{R}_2^1 = \mathbf{R}_{Y_2}(\alpha)\mathbf{R}_{X_2}(\beta)\mathbf{R}_{Y_2}(\gamma) = \begin{bmatrix} -s\alpha c\beta s\gamma + c\alpha c\gamma & s\alpha s\beta & s\alpha c\beta c\gamma + c\alpha s\gamma \\ s\beta s\gamma & c\beta & -s\beta c\gamma \\ -c\alpha c\beta s\gamma - s\alpha c\gamma & c\alpha s\beta & c\alpha c\beta c\gamma - s\alpha s\gamma \end{bmatrix} \tag{4-2}$$

where $\mathbf{R}_1^0$ is the rotation matrix of frame CS_1 w.r.t frame CS_0 obtained by multiplying the two successive basic rotation matrices $\mathbf{R}_{X_1}$ (about initially common *X*-axis by angle θ_1) and $\mathbf{R}_{Y_1}$ (about the moving Y'_1-axis by θ_2); $\mathbf{R}_2^1$ is the rotation matrix of frame CS_2 w.r.t frame CS_1 obtained by rotations performed about an axes of the moving CS_2, and $\mathbf{R}_2^0 = \mathbf{R}_1^0\mathbf{R}_2^1$ is the rotation matrix of frame CS_2 w.r.t the fixed frame CS_0 obtained by multiplying the matrices $\mathbf{R}_1^0$ and $\mathbf{R}_2^1$. The origin of frame CS_2 (centred at the *S* joint) and the end-effector point *E* can be represented in terms of the passive joint angles by the position vectors $\boldsymbol{S}^0$ and $\boldsymbol{E}^0$ (expressed in CS_0), respectively, as follows:

$$\boldsymbol{S}^0 = \boldsymbol{P}^0 + \mathbf{R}_1^0\boldsymbol{S}^1 = 0 + \begin{bmatrix} c\theta_2 & 0 & s\theta_2 \\ s\theta_1 s\theta_2 & c\theta_1 & -c\theta_2 s\theta_1 \\ -c\theta_1 s\theta_2 & s\theta_1 & c\theta_1 c\theta_2 \end{bmatrix}\begin{bmatrix} 0 \\ 0 \\ \mathrm{L}_1 \end{bmatrix} = \begin{bmatrix} \mathrm{L}_1 s\theta_2 \\ -\mathrm{L}_1 c\theta_2 s\theta_1 \\ \mathrm{L}_1 c\theta_1 c\theta_2 \end{bmatrix} \tag{4-3}$$

and

$$\boldsymbol{E}^0 = \boldsymbol{S}^0 + \mathbf{R}_2^0\boldsymbol{E}^2 = \mathbf{R}_1^0\begin{bmatrix} 0 \\ 0 \\ \mathrm{L}_1 \end{bmatrix} + \mathbf{R}_1^0\mathbf{R}_2^1\begin{bmatrix} 0 \\ 0 \\ \mathrm{L}_2 \end{bmatrix} \tag{4-4}$$

4.3.1 2-DOFs Proximal Module

The proximal part of the proposed hybrid mechanism is formed by connecting two open kinematic chains in parallel, one of which is actuated by the active universal joint (*A* joint) and the other one is connected to the passive universal joint *P*. Both universal joints *A* and *P* are fixed on the base on a distance *D* apart (on the fixed X_0-axis). The kinematic and CAD models of this closed-bar mechanism are shown in Figure 4-2.

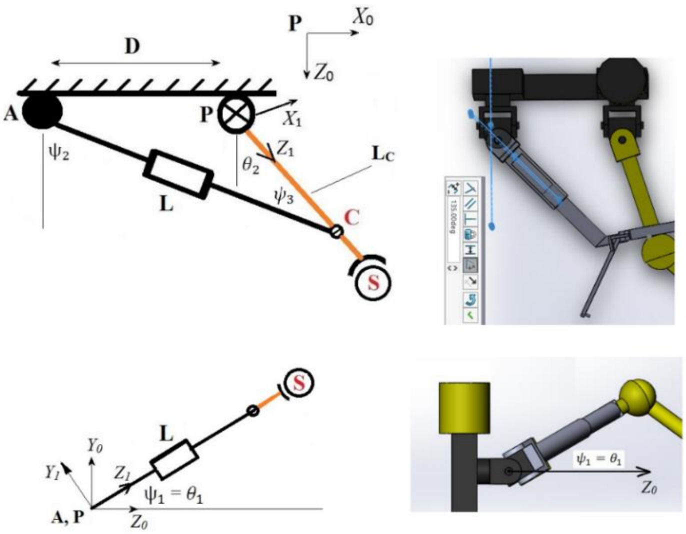

Figure 4-2: The proximal sub-mechanism as inverted slider crank mechanism (planar views): kinematic model (left), CAD model (right).

It is modelled as a spatial inverted slider-crank mechanism where the link L is a *UPR* link (universal–prismatic–revolute) – driven by the active universal joint with passive prismatic joint in the middle and connected through another passive revolute joint to the link L_1 at point C. The length parameter L_C is defined as the length distance along L_1 from the P joint to point C. The sets of two rotational angles of the universal joints A and P are (ψ_1, ψ_2) and (θ_1, θ_2), respectively. When the variable-length link L is actuated, the active joint variables (ψ_1, ψ_2) become the driving angles whereas the set of angles (θ_1, θ_2) of the second universal joint passively follow the rotational motion. This proximal module is designed such that the motion of the first revolute joint angle of both universal joints around the fixed X_0-axis (in Y_0-Z_0 plane) has the direct correspondence: i.e. $\theta_1 = \psi_1$, as shown in the lower part of Figure 4-2. However, due to the geometrical distance D between these universal joints along the X_0-axis, the joint angle θ_2 is a function of the joint angle ψ_2. Moreover, mechanically, the length L is a function of the joint angle ψ_2. The prismatic sliding joint is said to be passive, and cannot be actuated independently from the motion of the universal joints. The revolute passive joint angle between the two links is a function of both angles ψ_2 and θ_2, i.e. $\psi_3 = 90 + \psi_2 - \theta_2$. As a result, the passive link L_1 restrains the driving link L to a circular motion, in X_1-Z_1 plane. Alternatively, this coupled circular motion can be achieved by replacing the *UPR* link with the *URR* link, which is verified by CAD simulations and by applying the DOF formula (3-7) to the planar inverted slider-crank mechanism, shown in the upper part of Figure 4-2:

$$n = 3(M - J - 1) + \sum_i F_i = 3(4 - 4 - 1) + 4 = 1 \tag{4-5}$$

In fact, the universal joint can also be considered as two intersecting revolute joints. Thus, there are four 1-DOF joints (*RRPR* or *RRRR*) connected in the planar closed-bar mechanism that has one rotational DOF. The second equivalent revolute joint angles $(\theta_1 = \psi_1)$ of the two universal joints correspond to the second rotational DOF. As a result, the proximal sub-mechanism of the proposed hybrid mechanism in this work has in total 2-DOFs (rotational). Given the constant length parameters, the pose of the proximal module can be described using any set of just two universal joint angles (ψ_1, ψ_2) or (θ_1, θ_2). The position of the common connection point C can be expressed in terms of both universal joints' angles (transmission angles):

$$\boldsymbol{C} = \begin{bmatrix} \mathrm{L_C} s\theta_2 \\ -\mathrm{L_C} c\theta_2 s\theta_1 \\ \mathrm{L_C} c\theta_1 c\theta_2 \end{bmatrix} = \begin{bmatrix} \mathrm{L} s\psi_2 - \mathrm{D} \\ -\mathrm{L} c\psi_2 s\psi_1 \\ \mathrm{L} c\psi_1 c\psi_2 \end{bmatrix} \tag{4-6}$$

As $\theta_1 = \psi_1$, (4-6) can be reduced to a system of two equations. For the inverse positioning problem, with the given pose parameters (θ_1, θ_2), these will have two unknown variables (L and ψ_2) in two equations, from which the active universal joint angle ψ_2 is obtained as follows:

$$\psi_2 = \arctan(\tan(\theta_2) + \frac{D}{L_C c\theta_2}) \tag{4-7}$$

and the variable link length:

$$L = \frac{L_C c\theta_2}{c\psi_2} \tag{4-8}$$

On the other hand, the passive universal joint angle can also be expressed in terms of (function of) the active universal joint angle, i.e. $\theta_2 = f(\psi_2)$, by solving the forward positioning problem with the given joint parameters (ψ_1, ψ_2). Rewriting (4-7):

$$\tan(\psi_2) = \frac{L_C s\theta_2 + D}{L_C c\theta_2} \tag{4-9}$$

Squaring both sides of (4-9):

$$\tan^2(\psi_2) {L_C}^2 c^2(\theta_2) = {L_C}^2 s^2(\theta_2) + 2L_C\, s\theta_2\, D + D^2 \tag{4-10}$$

Substituting $cos^2(\theta_2)$ = 1 - $sin^2(\theta_2)$ and rearranging with x = $sin\,(\theta_2)$:

$$ax^2 + bx + c = 0 \tag{4-11}$$

where $a = {L_C}^2 + \tan^2(\psi_2){L_C}^2;\ b = 2L_C D;\ c = D^2 - \tan^2(\psi_2){L_C}^2$.

Solving the quadratic (4-11), the following expression for θ_2 can be derived:

$$\theta_2 = \arcsin(\frac{-b + \sqrt{b^2 - 4ac}}{2a}) \tag{4-12}$$

Once θ_2 is known, the variable link L can be found using (4-8). Also, the first equation in (4-6) can be rewritten, using (4-8), as follows:

$$L_C s\theta_2 - L_C c\theta_2 \tan(\psi_2) + D = 0 \tag{4-13}$$

Now, differentiating w.r.t ψ_2,

$$L_C c\theta_2 \frac{d\theta_2}{d\psi_2} + L_C s\theta_2 \frac{d\theta_2}{d\psi_2} \tan(\psi_2) - \frac{L_C c\theta_2}{c^2(\psi_2)} = 0 \tag{4-14}$$

(4-14) is rearranged to get the expression for kinematic coefficient $\frac{d\theta_2}{d\psi_2}$:

$$\frac{d\theta_2}{d\psi_2} = \frac{L_C c\theta_2}{c^2(\psi_2)(L_C c\theta_2 + L_C s\theta_2 \tan(\psi_2))} \tag{4-15}$$

Thus, taking the derivative of the position equations, the relationship between the rate of change of the active joint angles (ψ_1, ψ_2) of the proximal module and the rate of change of the passive joint angles (θ_1, θ_2), which can be considered as an independent generalised joint variables (or DOFs), is written in the matrix form:

$$\begin{bmatrix} \dot{\theta}_1 \\ \dot{\theta}_2 \end{bmatrix} = \begin{bmatrix} 1 & 0 \\ 0 & f(\psi_2) \end{bmatrix} \begin{bmatrix} \dot{\psi}_1 \\ \dot{\psi}_2 \end{bmatrix} \quad \text{and} \quad \begin{bmatrix} \dot{\psi}_1 \\ \dot{\psi}_2 \end{bmatrix} = \begin{bmatrix} 1 & 0 \\ 0 & g(\theta_2) \end{bmatrix} \begin{bmatrix} \dot{\theta}_1 \\ \dot{\theta}_2 \end{bmatrix} \tag{4-16}$$

where $f(\psi_2)$ is given by (4-15) and $g(\theta_2)$ can be derived in a similar manner by differentiating (4-13) w.r.t. θ_2. (4-16) can further be rewritten as follows:

$$\begin{bmatrix} \dot{\theta}_1 \\ \dot{\theta}_2 \end{bmatrix} = \mathbf{J_{Sf}} \begin{bmatrix} \dot{\psi}_1 \\ \dot{\psi}_2 \end{bmatrix} \quad \text{and} \quad \begin{bmatrix} \dot{\psi}_1 \\ \dot{\psi}_2 \end{bmatrix} = \mathbf{J_{Si}} \begin{bmatrix} \dot{\theta}_1 \\ \dot{\theta}_2 \end{bmatrix} \tag{4-17}$$

where $\mathbf{J_{Sf}}$ (S – serial, f - forward) is the forward and $\mathbf{J_{Si}}$ (i – inverse) is the inverse analytical Jacobian matrices of the proximal module. Here, *serial* notation for the Jacobian matrices is used due to the actuation of the serial linkage.

4.3.2 Cable-Driven Parallel Mechanism (CDPM)

The *CDPM* of the *HRM* consists of the base platform and the moving platform connected by four active cables in order to actuate the passive spherical 3-DOFs joint, as shown in Figure 4-3.

In fact, the central spherical joint constraints any translational motion allowing only rotational motions. There are three connection points on the base platform (*BP*) represented as (B_1, B_2, B_3) and three connection points on the moving platform (*MP*) represented as (U_1, U_2, U_3). Both platforms contain one concentric joint where two cables intersect. The cable links are modelled as *SPS* links with passive spherical joints at both ends and active prismatic joints aligned with the cable pulling lines of actions. The four (*m*) active cables for a 3-DOFs (*n*) module are a necessary condition ($m > n$) to fully constrain the mobile platform [163]. The base and mobile platform cable attachment points are defined with respect to frame CS_1 and CS_2, respectively. These geometrical parameters are considered as design parameters and can be optimised to improve the performance of *CDPM*.

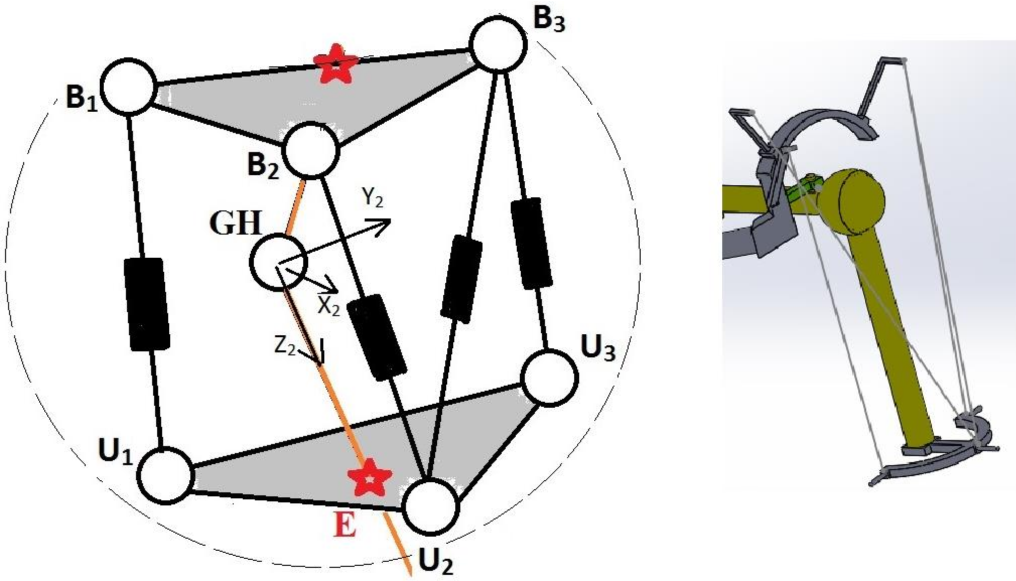

Figure 4-3: Cable-Driven Parallel Module of the *HRM*:
kinematic model (left), CAD model (right).

To be consistent with the preceding analysis, all the reference frames defined earlier are used here so that the orientation matrix $\mathbf{R}_2^1$ of the *MP* relative to the *BP* can be given in terms of the orientation angles (*α, β, γ*) from the passive joint angle space (generalised coordinates). The coordinates of the cable connection points $B_{1\text{-}3}$ and $U_{1\text{-}3}$ are constant in frames CS_1 and CS_2, respectively. The position vectors from points $B_{1\text{-}3}$ to point $U_{1\text{-}3}$, i.e. the cable vectors $\boldsymbol{l}_i$ (for *i* from 1 to 4), can be expressed with respect to frame CS_1 as follows:

$$\boldsymbol{l}_1^1 = \boldsymbol{S}^1 + \mathbf{R}_2^1\boldsymbol{u}_1^2 - \boldsymbol{b}_1^1 \quad (4\text{-}18)$$

$$\boldsymbol{l}_2^1 = \boldsymbol{S}^1 + \mathbf{R}_2^1\boldsymbol{u}_2^2 - \boldsymbol{b}_2^1 \quad (4\text{-}19)$$

$$\boldsymbol{l}_3^1 = \boldsymbol{S}^1 + \mathbf{R}_2^1\boldsymbol{u}_2^2 - \boldsymbol{b}_3^1 \quad (4\text{-}20)$$

$$\boldsymbol{l}_4^1 = \boldsymbol{S}^1 + \mathbf{R}_2^1\boldsymbol{u}_3^2 - \boldsymbol{b}_3^1 \quad (4\text{-}21)$$

where $\boldsymbol{b}_{1-3}^1$ are the position vectors, from CS_1 to the points $B_{1\text{-}3}$, expressed in frame CS_1 and $\boldsymbol{u}_{1-3}^2$ are the position vectors, from CS_2 to the points $U_{1\text{-}3}$, expressed in frame CS_2. The lengths of vectors $\boldsymbol{l}_i$ are:

$$l_i^2 = l_{ix}^2 + l_{iy}^2 + l_{iz}^2, \qquad i = 1\text{-}4 \quad (4\text{-}22)$$

Equations (4-22) are the position constraint equations for the cable driven parallel mechanism that can be derived by taking the dot product of the vector loop equations (4-18)-(4-21):

$$|\boldsymbol{l}_1^1| = \sqrt{(\boldsymbol{S}^1 + \mathbf{R}_2^1\boldsymbol{u}_1^2 - \boldsymbol{b}_1^1)^T(\boldsymbol{S}^1 + \mathbf{R}_2^1\boldsymbol{u}_1^2 - \boldsymbol{b}_1^1)} \tag{4-23}$$

$$|\boldsymbol{l}_2^1| = \sqrt{(\boldsymbol{S}^1 + \mathbf{R}_2^1\boldsymbol{u}_2^2 - \boldsymbol{b}_2^1)^T(\boldsymbol{S}^1 + \mathbf{R}_2^1\boldsymbol{u}_2^2 - \boldsymbol{b}_2^1)} \tag{4-24}$$

$$|\boldsymbol{l}_3^1| = \sqrt{(\boldsymbol{S}^1 + \mathbf{R}_2^1\boldsymbol{u}_2^2 - \boldsymbol{b}_3^1)^T(\boldsymbol{S}^1 + \mathbf{R}_2^1\boldsymbol{u}_2^2 - \boldsymbol{b}_3^1)} \tag{4-25}$$

$$|\boldsymbol{l}_4^0| = \sqrt{(\boldsymbol{S}^1 + \mathbf{R}_2^1\boldsymbol{u}_3^2 - \boldsymbol{b}_3^1)^T(\boldsymbol{S}^1 + \mathbf{R}_2^1\boldsymbol{u}_3^2 - \boldsymbol{b}_3^1)} \tag{4-26}$$

where $|\boldsymbol{l}| = [l_1, l_2, l_3, l_4]^T$ are the magnitudes of the cable lengths. To obtain the velocity relationship, (4-23)-(4-26) are squared and differentiated with respect to time:

$$2\, l_1\dot{l}_1 = (\dot{\boldsymbol{S}}^1 + \dot{\mathbf{R}}_2^1\, \boldsymbol{u}_1^2)^T(\boldsymbol{S}^1 + \mathbf{R}_2^1\boldsymbol{u}_1^2 - \boldsymbol{b}_1^1) + (\boldsymbol{S}^1 + \mathbf{R}_2^1\boldsymbol{u}_1^2 - \boldsymbol{b}_1^1)^T(\dot{\boldsymbol{S}}^1 + \dot{\mathbf{R}}_2^1\, \boldsymbol{u}_1^2) \tag{4-27}$$

$$2\, l_2\dot{l}_2 = (\dot{\boldsymbol{S}}^1 + \dot{\mathbf{R}}_2^1\, \boldsymbol{u}_2^2)^T(\boldsymbol{S}^1 + \mathbf{R}_2^1\boldsymbol{u}_2^2 - \boldsymbol{b}_2^1) + (\boldsymbol{S}^1 + \mathbf{R}_2^1\boldsymbol{u}_2^2 - \boldsymbol{b}_2^1)^T(\dot{\boldsymbol{S}}^1 + \dot{\mathbf{R}}_2^1\, \boldsymbol{u}_2^2) \tag{4-28}$$

$$2\, l_3\dot{l}_3 = (\dot{\boldsymbol{S}}^1 + \dot{\mathbf{R}}_2^1\, \boldsymbol{u}_2^2)^T(\boldsymbol{S}^1 + \mathbf{R}_2^1\boldsymbol{u}_2^2 - \boldsymbol{b}_3^1) + (\boldsymbol{S}^1 + \mathbf{R}_2^1\boldsymbol{u}_2^2 - \boldsymbol{b}_3^1)^T(\dot{\boldsymbol{S}}^1 + \dot{\mathbf{R}}_2^1\, \boldsymbol{u}_2^2) \tag{4-29}$$

$$2\, l_4\dot{l}_4 = (\dot{\boldsymbol{S}}^1 + \dot{\mathbf{R}}_2^1\, \boldsymbol{u}_3^2)^T(\boldsymbol{S}^1 + \mathbf{R}_2^1\boldsymbol{u}_3^2 - \boldsymbol{b}_3^1) + (\boldsymbol{S}^1 + \mathbf{R}_2^1\boldsymbol{u}_3^2 - \boldsymbol{b}_3^1)^T(\dot{\boldsymbol{S}}^1 + \dot{\mathbf{R}}_2^1\, \boldsymbol{u}_3^2) \tag{4-30}$$

The terms $\dot{\boldsymbol{S}}^1$, $\dot{\boldsymbol{b}}_{1-3}^1$ and $\dot{\boldsymbol{u}}_{1-3}^2$ are equal to zero because they are derivatives of constant parameters. Equations (4-27)-(4-30) can be further simplified to:

$$l_1\dot{l}_1 = (\boldsymbol{l}_1^1)^T\, (\dot{\mathbf{R}}_2^1\, \boldsymbol{u}_1^2) \tag{4-31}$$

$$l_2\dot{l}_2 = (\boldsymbol{l}_2^1)^T\, (\dot{\mathbf{R}}_2^1\, \boldsymbol{u}_2^2) \tag{4-32}$$

$$l_3\dot{l}_3 = (\boldsymbol{l}_3^1)^T\, (\dot{\mathbf{R}}_2^1\, \boldsymbol{u}_2^2) \tag{4-33}$$

$$l_4\dot{l}_4 = (\boldsymbol{l}_4^1)^T\, (\dot{\mathbf{R}}_2^1\, \boldsymbol{u}_3^2) \tag{4-34}$$

The cable connection points on *MP* can be expressed in frame CS_1, $\boldsymbol{u}_{1-3}^1 = \mathbf{R}_2^1\boldsymbol{u}_{1-3}^2$, and the derivative of the rotation matrix, $\dot{\mathbf{R}}_2^1 = \Omega_2^1\, \mathbf{R}_2^1$, where Ω_2^1 is defined as the angular velocity screw matrix of the *MP* (w.r.t. the *BP*). Applying the substitution and rewriting:

$$l_1\dot{l}_1 = (\boldsymbol{u}_1^1 \times \boldsymbol{l}_1^1)^T\, \boldsymbol{\omega}_2^1 \tag{4-35}$$

$$l_2\dot{l}_2 = (\boldsymbol{u}_2^1 \times \boldsymbol{l}_2^1)^T\, \boldsymbol{\omega}_2^1 \tag{4-36}$$

$$l_3\dot{l}_3 = (\boldsymbol{u}_2^1 \times \boldsymbol{l}_3^1)^T\, \boldsymbol{\omega}_2^1 \tag{4-37}$$

$$l_4\dot{l}_4 = (\boldsymbol{u}_3^1 \times \boldsymbol{l}_4^1)^T\, \boldsymbol{\omega}_2^1 \tag{4-38}$$

Finally, rearranging them in the matrix form:

$$\begin{bmatrix} l_1 & 0 & 0 & 0 \\ 0 & l_2 & 0 & 0 \\ 0 & 0 & l_3 & 0 \\ 0 & 0 & 0 & l_4 \end{bmatrix} \begin{bmatrix} \dot{l}_1 \\ \dot{l}_2 \\ \dot{l}_3 \\ \dot{l}_4 \end{bmatrix} = \begin{bmatrix} (\boldsymbol{u}_1^1 \times \boldsymbol{l}_1^1)_x & (\boldsymbol{u}_1^1 \times \boldsymbol{l}_1^1)_y & (\boldsymbol{u}_1^1 \times \boldsymbol{l}_1^1)_z \\ (\boldsymbol{u}_2^1 \times \boldsymbol{l}_2^1)_x & (\boldsymbol{u}_2^1 \times \boldsymbol{l}_2^1)_y & (\boldsymbol{u}_2^1 \times \boldsymbol{l}_2^1)_z \\ (\boldsymbol{u}_2^1 \times \boldsymbol{l}_3^1)_x & (\boldsymbol{u}_2^1 \times \boldsymbol{l}_3^1)_y & (\boldsymbol{u}_2^1 \times \boldsymbol{l}_3^1)_z \\ (\boldsymbol{u}_3^1 \times \boldsymbol{l}_4^1)_x & (\boldsymbol{u}_3^1 \times \boldsymbol{l}_4^1)_y & (\boldsymbol{u}_3^1 \times \boldsymbol{l}_4^1)_z \end{bmatrix} (\boldsymbol{\omega}_2^1)^1 \tag{4-39}$$

$$\mathbf{B_1}\,\dot{\boldsymbol{l}} = \mathbf{B_2}(\boldsymbol{\omega}_2^1)^1 \tag{4-40}$$

where **[4 × 4]** matrix $\mathbf{B}_1$ is usually referred as forward Jacobian and **[4 × 3]** matrix $\mathbf{B}_2$ as inverse Jacobian of the parallel mechanism, $\dot{\boldsymbol{l}}$ is the vector of the rate of change of the cable lengths and $(\boldsymbol{\omega}_2^1)^1$ is the angular velocity vector of *MP* w.r.t *BP* and expressed in frame CS_1. Equation (4-40) is useful in determining the three different types of kinematic singularities due to the parallel structure of *CDPM* [156]. As matrix $\mathbf{B_1}$ is a square matrix, it can be inverted to derive the **[4 × 3]** geometrical Jacobian $\mathbf{J_{Pg}}$ (P –parallel, g - geometrical) of *CDPM*:

$$\dot{\boldsymbol{l}} = \mathbf{B_1}^{-1}\mathbf{B_2}\,(\boldsymbol{\omega}_2^1)^1 = \mathbf{J_{Pg}}\,(\boldsymbol{\omega}_2^1)^1 \tag{4-41}$$

The vector of the active cable joint rates can now be related to the rate of change of the spherical joint's orientation angles (passive joint rates of *CDPM*):

$$\begin{bmatrix} \dot{l}_1 \\ \dot{l}_2 \\ \dot{l}_3 \\ \dot{l}_4 \end{bmatrix} = \mathbf{J_{Pg}} \begin{bmatrix} 0 & c\alpha & s\alpha s\beta \\ 1 & 0 & c\beta \\ 0 & -s\alpha & c\alpha s\beta \end{bmatrix} \begin{bmatrix} \dot{\alpha} \\ \dot{\beta} \\ \dot{\gamma} \end{bmatrix} = \mathbf{J_{Pg}S} \begin{bmatrix} \dot{\alpha} \\ \dot{\beta} \\ \dot{\gamma} \end{bmatrix} = \mathbf{J_{Pi}} \begin{bmatrix} \dot{\alpha} \\ \dot{\beta} \\ \dot{\gamma} \end{bmatrix} \tag{4-42}$$

where $\mathbf{S}$ is a square matrix that relates the angular velocity components of the parallel module to the passive spherical joint angles and $\mathbf{J_{Pi}}$ is a **[4 × 3]** inverse analytical Jacobian matrix of *CDPM* module. The so called pseudoinverse **[3 × 4]** matrix, $\mathbf{J_{Pi}}^{\dagger} = (\mathbf{J_{Pi}}^T\mathbf{J_{Pi}})^{-1}\mathbf{J_{Pi}}^T$, can be employed for further analysis of *CDPM*. The transpose of the derived Jacobian, $\mathbf{A} = \mathbf{J_{Pi}}^T$, which is also called the *structure matrix* of *CDPM*, represents the mapping between the cable forces ($\boldsymbol{f}$) and the manipulator torques ($\boldsymbol{\tau}$).

The combined inverse analytical Jacobian of the hybrid mechanism can now be written as follows:

$$\begin{bmatrix} \dot{\psi}_1 \\ \dot{\psi}_2 \\ \dot{l}_1 \\ \dot{l}_2 \\ \dot{l}_3 \\ \dot{l}_4 \end{bmatrix} = \begin{bmatrix} \mathbf{J_{Si}} & \mathbf{0_{2\times3}} \\ \mathbf{0_{4\times2}} & \mathbf{J_{Pi}} \end{bmatrix} \begin{bmatrix} \dot{\theta}_1 \\ \dot{\theta}_2 \\ \dot{\alpha} \\ \dot{\beta} \\ \dot{\gamma} \end{bmatrix} = [\dot{\boldsymbol{q}}_{\boldsymbol{a}}] = \mathbf{J_i}[\dot{\boldsymbol{q}}_p] \tag{4-43}$$

where $\mathbf{J_i}$ is a $\mathbf{[6 \times 5]}$ unified inverse analytical Jacobian matrix that relates the vector of the active joint rates $\dot{\boldsymbol{q}}_{\boldsymbol{a}}$ (where $\boldsymbol{q}_{\boldsymbol{a}}$ is a cable space vector combined with the active universal joints) to the vector of the passive joints' rates $\dot{\boldsymbol{q}}_p$. The vector $\boldsymbol{q}_p = (\theta_1, \theta_{2,} \alpha, \beta, \gamma)^T$ can be defined as the vector of the generalised coordinates - the minimum number of variables that can uniquely define the pose of the hybrid manipulator. These are the five angle parameters that correspond to 5-DOFs of the proposed hybrid mechanism.

Even though the unified relationships are important for the analysis of the proposed hybrid mechanism, it is useful to decouple the two modules and analyse them separately, e.g. to identify the singular configurations. As in *PM*s, the forward kinematic problem of *CDPM* is not trivial and leads to multiple solutions. However, due to the special arrangements of the cable connection points and the actuation redundancy, it is possible to obtain unique current forward kinematic solution of *CDPM* using numerical iteration method. To demonstrate the kinematic merits of the proposed hybrid mechanism and to undertake a comprehensive analysis of different types of its singularities, the application of robotic exoskeleton for human shoulder rehabilitation is considered in Section 4.3.

4.4 Numerical Results

The human shoulder is a multi-joint complex that can be modelled as a 5-DOFs serial linkage: a *"clavicle"* link attached to the human torso through the 2-DOFs universal joint on one end, and serially connected through the 3-DOFs ball-and-socket shoulder joint to the *"humerus"* link on the other end. Analogously, for analysis purposes, the inner passive linkage of the proposed mechanism in this work is treated as the human shoulder linkage. In this regard, the generalized coordinates defined in Section 4.2 represent the human shoulder joint angles.

The design parameters of the hybrid mechanism for the considered shoulder case are listed in Table 4-1. The ROM of the human shoulder angles are taken from the literature [164]. The passive spherical joint representing the human shoulder joint is allowed to have the full range of human shoulder motion: i.e. α, β and γ can vary from -35 to 90, from -40 to 90 and from -90 to 90 degrees, respectively. Both of the passive universal joint angles are restricted to -40 to 40 degrees as the human shoulder girdle's ROM is quite limited. The pose, at which all the joint variables are zero, i.e. all the frames ($CS_{0\text{-}2}$) are aligned, corresponds to the upper arm being stretched to the right of the human body. The link lengths are arbitrary chosen based on the average dimensions of an adult individual. All the kinematic equations have been written in the MATLAB code to computationally analyse the singularities and workspace of the mechanism.

Table 4-1. The design and joint angle parameters of the *HRM*.

D = L_c (mm)	**L_1** (mm)	**L_2** (mm)	**b** (mm)	**u** mm	$\boldsymbol{\theta_1}$ range°	$\boldsymbol{\theta_2}$ range°	$\boldsymbol{\alpha}$ range°	$\boldsymbol{\beta}$ range°	$\boldsymbol{\gamma}$ range°
200	220	270	100	100	-40:40	-40:40	-35:90	-40:90	-90:90
	x-comp	*y*-comp	*z*-comp				*x*-comp	*y*-comp	*z*-comp
$\boldsymbol{b}_1^1$	-2b	2b	L_1+b			$\boldsymbol{u}_1^2$	-u	0	L_2
$\boldsymbol{b}_2^1$	-b	2b	L_1			$\boldsymbol{u}_2^2$	0	u	L_2
$\boldsymbol{b}_3^1$	b	2b	L_1			$\boldsymbol{u}_3^2$	u	0	L_2

4.4.1 Singularity Analysis

As stated earlier, due to the hybrid structure of the mechanism under study, it is important to undertake a complete analysis of its singular configurations by considering the <u>decoupled singularities</u> associated with the individual modules of the hybrid *HRM* and the <u>combined singularities</u> arising from their structural arrangement.

1) *The singularities associated with the proximal module*. As described in Section 4.2.1, the shoulder girdle mechanism is modelled as a slider crank mechanism with two sets of transmission angles (ψ_1, ψ_2) and (θ_1, θ_2). The singularities of such mechanism can be obtained by examining its Jacobian matrices to determine the configurations leading to $\det(\mathbf{J_S})_{2\times2} = 0$. According to (4-16), the determinant of the forward Jacobian becomes zero when $f(\psi_2)$ or (4-15) is equal to zero. This happens when $\cos(\theta_2)$ goes to zero, which corresponds to $\theta_2 = \pm 90$ deg. In fact, the singularities of such mechanism appear when the driving link is unable to move

the mechanism, or in mathematical terms when $\frac{d\theta_2}{d\psi_2} = 0$. By inspecting $g(\theta_2)$ in the same way, it can be concluded that a singular configuration will also be reached when $\psi_2 = 0$. This is why the initial arrangement of the driving linkage is already at an angle to avoid such uncontrollable configuration. There are no singularities associated with the other DOF of the shoulder girdle mechanism, as $\theta_1 = \psi_1$. Moreover, due to the quite limited ROM of the real human shoulder girdle (-40 to 40 deg. for both angles θ_1 and θ_2), its joint angles will never reach ± 90 deg. Therefore, the proximal module under study does not have any singularities ($\det(\mathbf{J_S})_{2\times 2} \neq 0$) within its workspace due to the restricted ranges of the shoulder girdle angles.

2) *The singularities associated with the distal CDPM module*. Due to the unidirectional force properties of the cable-driven parallel mechanism, the singularities for this sub-mechanism are further classified into two categories:

(i) Kinematic singularities of CDPM. These types of singularities are due to the parallel structure of the mechanism and they are obtained through examining the parallel Jacobian matrices when treating cables as rigid links. The singularities of such parallel mechanisms are usually divided into three types:

- The 1st type of *parallel singularity* is faced when $\det(\mathbf{B_1})_{4\times 4} = 0$ and $\det(\mathbf{B_2})_{4\times 3} \neq 0$. This follows that *MP* loses one or more degrees of freedom.
- The 2nd type of parallel singularity is faced when $\det(\mathbf{B_1})_{4\times 4} \neq 0$ and $\det(\mathbf{B_2})_{4\times 3} = 0$. This follows that *MP* gains one or more degrees of freedom.
- The 3rd type of parallel singularity is faced when $\det(\mathbf{B_1})_{4\times 4} = 0$ and $\det(\mathbf{B_2})_{4\times 3} = 0$. This follows that *MP* can undergo finite motions when its actuators are locked or where a finite input does not produce an output motion.

From inspecting the determinant of forward parallel Jacobian matrix $\mathbf{B_1}$, it can be concluded that the singular configurations appear when the cable lengths become zero (which is not feasible in *CDPM*). As the inverse parallel Jacobian matrix $\mathbf{B_2}$ is a non-square matrix due to the actuation redundancy of *CDPM*, the parallel Jacobian matrix $\mathbf{J_P}$ is also a non-square matrix and it is singular only if matrix $\mathbf{B_2}$ is singular. Hence, the singularities associated with the parallel structure of *CDPM* are identified through the rank analysis of matrix $\mathbf{B_2}$. As can be seen from (4-39), matrix $\mathbf{B_2}$ depends on the design variables (cable connection coordinates) and it is known that singularities can be caused by an improper respective geometry of the parallel platforms: e.g. when the link vectors are parallel to each other. This implies that the similar polygons with the same orientation for the base and mobile platforms of *CDPM* should be avoided at the design stage. For this reason, the *CDPM* of the proposed hybrid mechanism has been designed with different polygons for its base and mobile platforms, as can be seen from the coordinates of the cable attachment points in Table 4-1. Optimal designs of parallel robots can also be achieved by examining kinetostatic performance indices (i.e. condition number, conditioning index, manipulability [165]) which are usually used to qualify the workspace of parallel robots.

Since cables in *CDPM* are not rigid links and can become slack, the singularity analysis just from the kinematical perspective is not sufficient and the structure matrix **A**, which is a transpose of the parallel Jacobian, has to be examined to identify the configurations where cables fail to manipulate the end-effector platform with positive tensions (force-closure condition). Such configurations are said to be singular in terms of force-closure even if there is no kinematic singularity. This leads to the next type of *CDPM* singularities.

(ii). Force-closure singularities of CDPM associated with the force-closure condition of *CDPM*. These are obtained by examining the structure matrix **A**. For example, when $\det(\mathbf{A})_{3\times4} = 0$, they are *force-closure singularities.* There are various ways to check this condition:

- When $\mathrm{rank}(\mathbf{A}) < n$, the tension-closure condition is not satisfied
- When $\det(\mathbf{A}\mathbf{A}^T) = 0$, the tension-closure condition is not satisfied
- Inspecting the row vectors of $\mathbf{A}_{\mathrm{n}\times\mathrm{m}}$. This procedure [166] starts with taking the cross-product of any two different columns of **A** which results in a set of induced vectors. Then, taking the dot products of every induced vectors with the corresponding remaining (*m – 2*) columns, generate a new set of $[(m-2)\times 1]$ vectors. Finally, by checking the signs of the last vectors, the force-tension condition can be obtained. If the entries have different signs, the force-closure condition will be satisfied. Also, note that during the cross-product procedure, the linear dependency of the vectors should be checked to remove any zero vectors.

• Finding the null space $\mathbf{N}(\mathbf{A})$ to check the so-called tension factor $TF = \frac{\min(\boldsymbol{N}(\mathbf{A}))}{\max(\boldsymbol{N}(\mathbf{A}))}$ [167]. If TF ($0 < TF < 1$) is close to zero, tension-closure condition will not be satisfied.

As it is impossible to depict the variation of the tension factor as a function of the three orientation angles (α, β, γ) of *CDPM*, this performance index was presented with the main two orientation angles α and β, which are sufficient to cover the workspace of the end-effector, with $\gamma = 0$. The *TF* is numerically calculated at each pose for the defined ranges of orientation angles, α and β, with spacing $\Delta = 1^{\circ}$. The complex variation of the *TF* for the considered workspace of 3-DOFs *CDPM* is presented in 3D plot, as a meshed surface plot shown in Figure 4-4. The distribution of the tension factor of *CDPM* shows the specific regions that are close or far away from singularities. Even though the tension factor distribution plot shows some regions when *TF* approaches zero, these are still not completely singular configurations and the inverse kinematics/dynamics problems at these poses have real unique solutions.

Figure 4-4: The distribution of the Tension Factor over the *CDPM* workspace.

In contrast, the tension-closure inspection methods, described in [166, 168], can only state if the tension condition is satisfied or not, but do not provide the measure of distribution of poses close to singular, like the tension factor method. Also, note that the methods to assess the force closure condition are implemented only after the rank deficiency of matrix **A** is checked, which is related to kinematic singularities. This fact can lead to an argument that the analysis of kinematic singularities may become redundant with the complete analysis of force closure singularities.

By implementing the above checks for force-closure singularities in MATLAB, there were no singular points detected within the workspace of the human shoulder joint. This is expected as the proposed *CDPM* (with its special geometry and cable routing) has more cables than DOFs, and such actuation redundancy eventually avoids singular configurations, both kinematic and force closure. It is worth to note here, that due to this redundancy in *CDPM* the inverse dynamics problem, i.e. finding the positive tension distribution for a given wrench, will lead to multiple (even infinite) solutions. This is usually solved by implementing different optimization techniques [169, 170].

The *combined singularities* associated with the serial arrangement of the proximal and distal modules. The derived unified Jacobian matrix in (4-43) cannot be utilized to access this type of singularity due to the large zero-blocks in the off-diagonal components which decouples the kinematic relations. However, as the inner restrained links of the proposed *HRM* are just serially connected through the common joint, this type of singularity appears when these passive links of both modules are fully aligned or folded. The two shoulder links of *HRM* cannot fold into each other due to the spherical joint limits and mechanical interference of the limbs. Whenever they are fully extended, such “singular” configuration corresponds just to the boundary point of the mechanism’s workspace. Therefore, this type of singularity corresponds to the poses of maximum reach of the mechanism. Indeed, humans exploit such poses as mechanical advantages, e.g. to increase the load carrying capacity of the end-effector.

Finally, it can be concluded that for the given ranges of passive shoulder angles, the workspace of the proposed *HRM* is free of singularities. Figure 4-5 shows the cloud of points (241,425 points) of the end-effector position $\boldsymbol{E}^0$ (4-4) for the specified ROM of the shoulder joints.

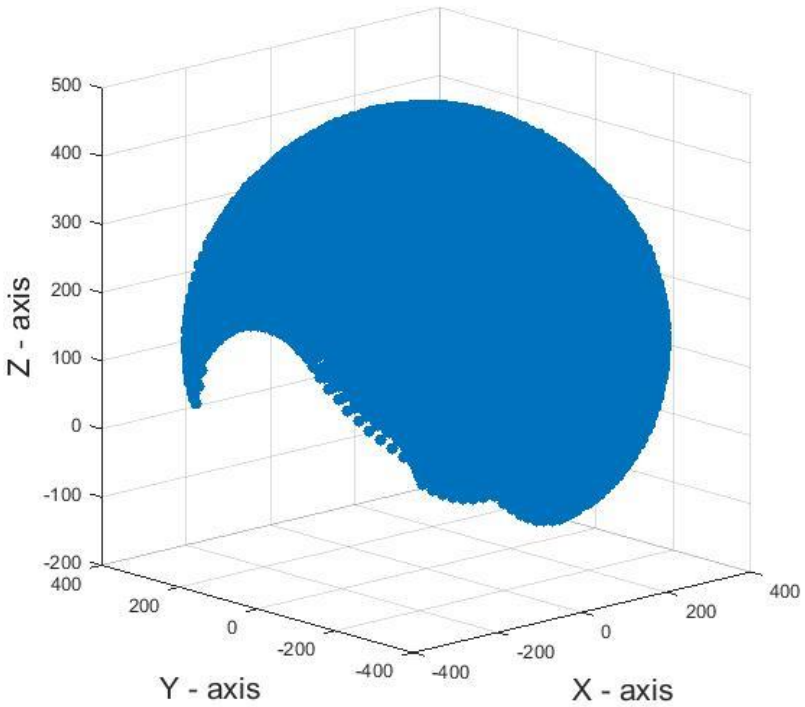

Figure 4-5. The human shoulder workspace free of singularities.

4.4.2 Trajectory Planning

The proposed *HRM* is designed to accomplish different complex shoulder motion tasks. A *trajectory* is defined as the path of the desired motion which is time-parameterised in pose space. Usually, it is desirable to generate a smooth trajectory (smooth transitions of velocities and accelerations) to avoid undesirable frictions and loading at the joint or motor levels. It is worth to know that a smooth trajectory can be generated either in *Cartesian space* (operational space) or *joint space*, and that there are associated differences between these two approaches. In this work, the trajectories are generated in joint space to ensure that the end-effector stays within the reachable workspace and does not fall into singular configurations, which cannot be ensured if the trajectory is planned in Cartesian space. In either way, the initial, final and/or intermediate route points can still be specified in Cartesian space.

2D motion planned in joint space. The shoulder abduction movement in the frontal plane of the human body, mostly exercised in rehabilitation therapies [27], is selected as a simple trajectory to demonstrate the inverse kinematics of the hybrid mechanism. Such motion is entirely in *YZ*-plane, and the CAD model of mechanism at the initial, middle and final poses of the simulated trajectory is shown in Figure 4-6. The joint space trajectory $\boldsymbol{q}(t)$ = $[\theta_1(t), \theta_2(t), \alpha(t), \beta(t), \gamma(t)]$ is planned using cubic polynomial from the initial position $\boldsymbol{q}_s$ = $[0\ 0\ 0\ 90\ 0]^T$ to the final configuration $\boldsymbol{q}_f$ = $[40\ 0\ 0\ \text{-}50\ 0]^T$ in a time interval of t (t = 5) seconds. Also, the initial and final velocities (and accelerations) for the desired path are all set to zero $\dot{\boldsymbol{q}}_s$=$\dot{\boldsymbol{q}}_f$=$\ddot{\boldsymbol{q}}_s$=$\ddot{\boldsymbol{q}}_f$ $= 0$. The angles of the active universal joint $\psi_{1-2}(t)$ and the lengths of cables $l_{1\text{-}4}$(t) for the entire trajectory are determined by solving inverse kinematic equations in Section 4.2 at each instance in time. Figure 4-7 shows the actuator space (ψ_1, ψ_2, l_1, l_2, l_3, l_4) profiles for simulated trajectory $\boldsymbol{q}(t)$. As can be seen from the graphs, the first robot angle ψ_1 is directly equivalent to the joint angle θ_1; the second robot angle ψ_2 is not actuated as the motion is planned entirely in *YZ*-plane; all cable lengths decreased during the planned motion to pull the arm, and the length profiles of cables 2 and 3 are identical since these two cables are symmetrically placed about the *YZ*-plane. The position of the end-effector w.r.t. torso (4-4) is plotted in Figure 4-8, validating that its motion is planar.

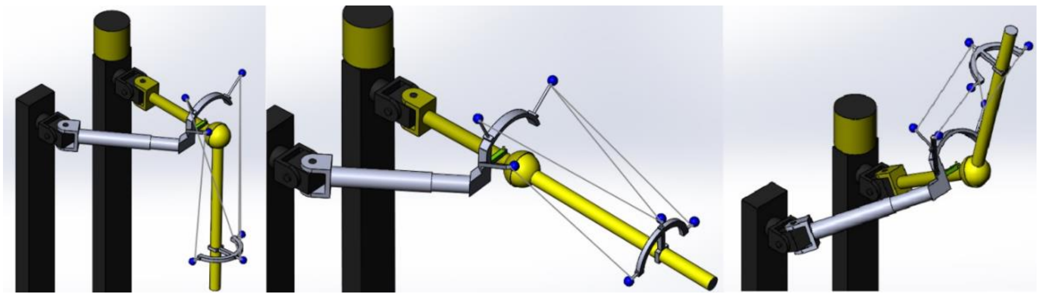

Figure 4-6: The CAD model of the hybrid mechanism during the shoulder abduction.

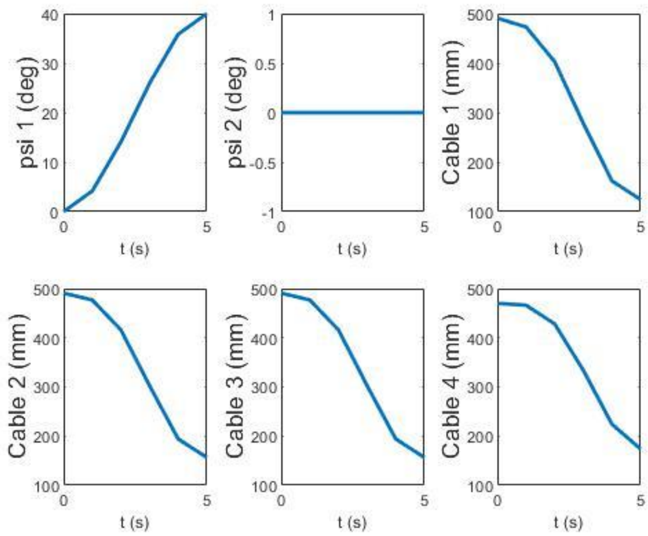

Figure 4-7: The actuator space profiles for the simulated trajectory in 2D.

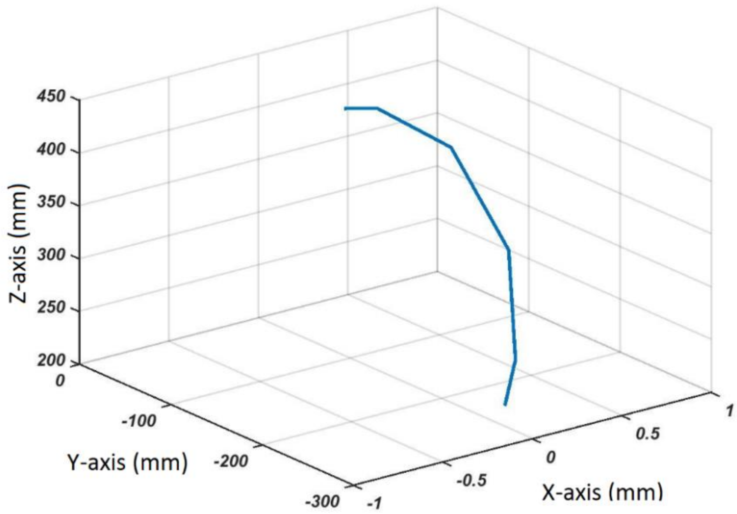

Figure 4-8: The end-effector position in operational space during the simulated trajectory in 2D.

To further verify the kinematics and derived unified Jacobian, the rates of change of the actuator space variables are obtained using (4-43) at each instance of time and plotted over the planned trajectory, as shown in Figure 4-9. It can be seen that the plots in Figure 4-9 comparable to the derivatives of the actuator space variables in Figure 4-7. The negative cable velocity profiles indicate that all cables decreased in length. Again, the velocity profiles for the cables 2 and 3 are identical and all the velocities started and terminated at zero.

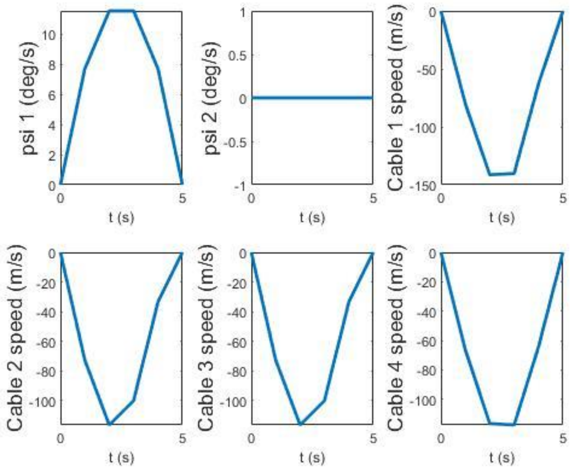

Figure 4-9: The derivatives of the actuator space variables.

<u>*3D motion planned in joint space*</u>. Another case study is simulated to move the mechanism's end-effector in 3D operational space. Similar to the previous example, the trajectory is planned in joint space with the chosen interval of time t (t = 10). In addition to the initial and final poses, another three points are included

on the way (way-points), as follows: $\boldsymbol{q}_1$ = [0 0 0 0 0]^T, $\boldsymbol{q}_2$ = [20 10 20 -20 10]^T, $\boldsymbol{q}_3$ = [0 20 40 0 -10]^T, $\boldsymbol{q}_4$ = [-10 30 60 20 -10]^T, $\boldsymbol{q}_5$ = [0 40 80 0 -10]^T. The end-effector position E^0 (w.r.t torso) at each of the way-points along the defined trajectory is plotted in Figure 4-10. Note that, the Cartesian path of the end-effector is not known initially when planned in joint space.

The joint space variables, the corresponding variables of the actuator space, obtained through the inverse kinematics, and the Cartesian coordinates of the end-effector are all listed in Table 4-2 for a set of randomly generated set of poses. Also, a tension factor is calculated at each pose and it can be seen that *TF* is getting smaller at the end of the trajectory where some of the joint space variables (θ_2 and α) approach their ROM limits. It can also be observed that, when D = L_c, the relationship between the transmission angles of the slider crank mechanism becomes 2:1. That is, for a 20 degrees rotation of the robotic angle ψ_2, there is a 40 degrees rotation of the joint angle θ_2. The design parameters can further be optimized based on different performance indices (including *TF)* of the workspace.

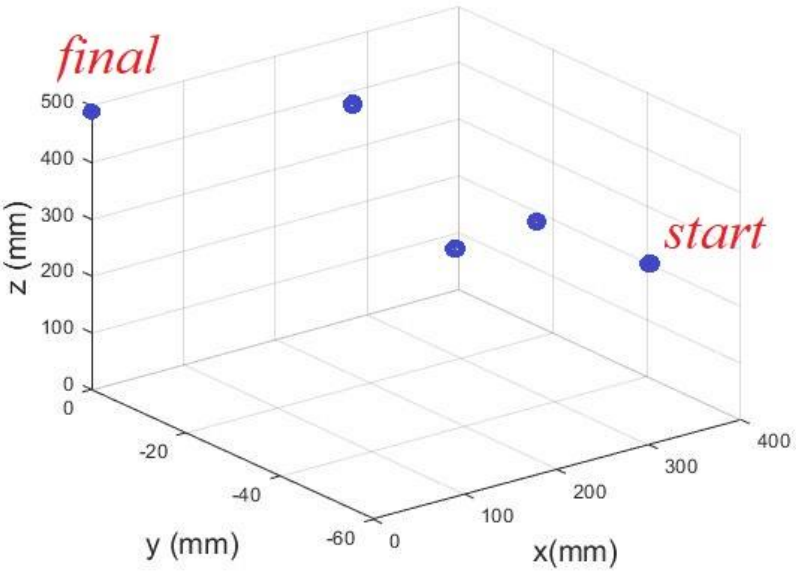

Figure 4-10: Positions of the end-effector points in operational space during the simulated trajectory in 3D.

Other different trajectories and configurations of the designed hybrid *HRM* have been tested and all the kinematics has been verified in a MATLAB-CAD environment.

Table 4-2. The tabulated data for the simulated trajectory in 3D.

	Joint Space (degrees)					**Actuator Space** (degrees, mm)						**Cartesian Space** (mm)			**TF**
	θ_1	θ_2	α	β	γ	ψ_1	ψ_2	l_1	l_2	l_3	l_4	E_x	E_y	E_z	
Init	0	0	0	0	0	0	45	280	304	304	336	0	0	490	0.51
	20	10	20	-20	10	20	50	312	287	188	235	203	-54	416	0.39
	0	20	40	0	-10	0	55	368	346	256	297	282	0	380	0.47
	-10	30	60	20	-10	-10	60	458	419	295	346	359	-48	249	0.33
Final	0	40	80	0	-10	0	65	510	383	197	280	395	0	76	0.21

A small-scale prototype of the proposed hybrid mechanism was specially built to test its kinematic performance (Figure 4-11). It was fabricated from the manufactured and 3D printed parts: the universal joints (purchased) with the prismatic slider are metallic, while the ball-and-socket joint is 3D printed from plastic. All links were assembled together to form a hybrid mechanism and the high strength fishing lines were employed for cables. The prototype mechanism can be manually actuated to test the workspace range and the changes in cables' lengths during different shoulder motions. The workspace analysis of the physical prototype demonstrated that the ranges of motions are restricted only by the joint limits, i.e. the limits of the ball-and-socket and universal joints. The upper limit of the spherical joint is shown in Figure 4-11 (right).

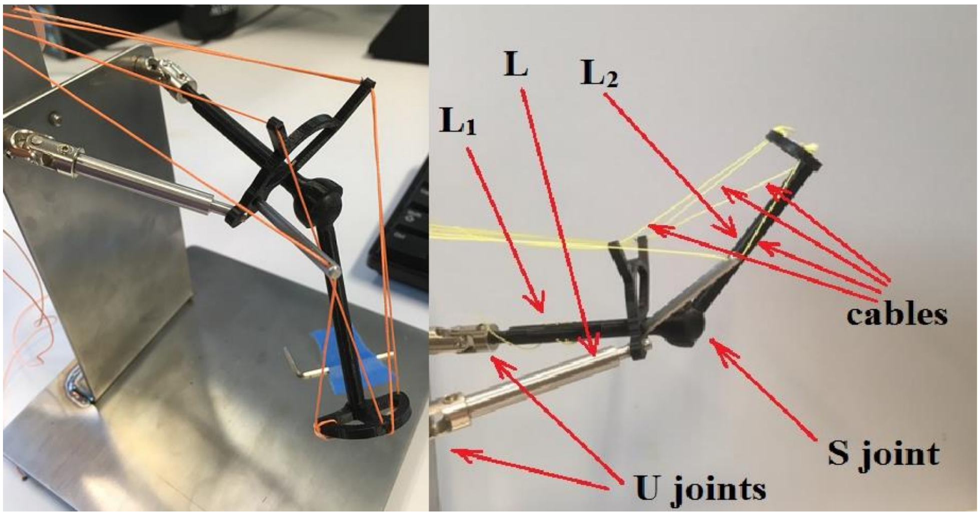

Figure 4-11: A prototype of the hybrid mechanism.

4.5 Tension Optimization in CDPM

One of the most important properties of cable-driven robots is their inability to exert pushing forces [170]. Thus, it is required to maintain positive tension in cables so that they do not slack. In order to apply a certain torque on *CDPM*, a set of the corresponding cable tensions has to be derived. When solving Inverse Dynamics (ID) problem of *CDPM*, which is the problem of finding the cable tensions from the given wrench vector, the solution sets may contain negative tensions. In other words, there are infinite number of solutions for ID problem of *CDPM* due to its redundancy: the number of cables (m = 4) is greater than the number of DOFs (n = 3). However, taking into account that open-ended cables can only exert pulling forces, according to Caratheodory's theorem, at least $n+1$ cables are needed to control a n-DOFs cable-driven parallel mechanism [171]. Therefore, to satisfy this requirement, a 3-DOFs *CDPM* of the proposed hybrid *HRM* is actuated by four cables.

Still, to obtain a set of positive tensions from the given wrench vector, some kind of tension optimization algorithm is needed. There are different approaches to solve this problem, e.g. solving ID using a linear program (LP) optimization method [172,173], a quadratic program (QP) optimisation method [174, 175], minimum infinity norm of a vector function [176] and other methods [177-179].

In this work, a linear program optimization method has been used to solve ID problem of *CDPM* for the positive cable tensions within the defined bounds. To demonstrate the use of the selected approach, a dynamic model of *CDPM* [180] is briefly presented here, in the joint space of *CDPM*, $\boldsymbol{q} = (\alpha, \beta, \gamma)^T$, as follows.

$$\mathbf{M}(\boldsymbol{q})\ddot{\boldsymbol{q}} + \mathbf{C}(\boldsymbol{q}, \dot{\boldsymbol{q}}) + \mathbf{G}(\boldsymbol{q}) + \boldsymbol{\Gamma}_{ext} = -\mathbf{J}_{\mathbf{Pi}}{}^{T}(\boldsymbol{q})\boldsymbol{f} \tag{4-44}$$

where

$$\mathbf{M}(\boldsymbol{q}) = \mathbf{S}^{\mathrm{T}} \begin{bmatrix} I_{O_x} c_\beta c_\gamma & I_{O_x} s_\gamma & 0 \\ -I_{O_x} c_\beta s_\gamma & I_{O_y} c_\gamma & 0 \\ I_{O_z} s_\beta & 0 & I_{O_z} \end{bmatrix}, \qquad \text{Mass matrix}$$

$$\mathbf{C}(\boldsymbol{q}, \dot{\boldsymbol{q}}) = \mathbf{S}^{T} \begin{bmatrix} I_{O_x}(-\dot{\alpha}\dot{\beta} s_\beta c_\gamma - \dot{\alpha}\dot{\gamma} c_\beta s_\gamma + \dot{\beta}\dot{\gamma} c_\gamma) \\ I_{O_y}(\dot{\alpha}\dot{\beta} s_\beta s_\gamma - \dot{\alpha}\dot{\gamma} c_\beta c_\gamma - \dot{\beta}\dot{\gamma} s_\gamma) \\ I_{O_z}\dot{\alpha}\dot{\beta} c_\beta \end{bmatrix} + \mathbf{S}^{T}(\boldsymbol{\omega}_\varepsilon \times (\mathbf{I}_{\mathrm{O}}\boldsymbol{\omega}_\varepsilon), \qquad \text{Coriolis matrix}$$

$$\mathbf{G}(\boldsymbol{q}) = -\mathbf{S}^{\mathrm{T}}(\boldsymbol{r}_{OG} \times ({}^{\varepsilon}_{\mathrm{O}}\mathbf{R}\, m\boldsymbol{g})). \qquad \text{Gravity matrix}$$

Given the *CDPM* dynamic model and the desired pose or trajectory in the joint space, the left hand side of the *CDPM* dynamic equation (4-44), can be calculated. The dynamic equation can then be rewritten in the following form:

$$\boldsymbol{\tau} = \mathbf{A}\boldsymbol{f} \tag{4-45}$$

where $\boldsymbol{\tau}$ is a $[\mathbf{3} \times \mathbf{1}]$ torque vector, $\mathbf{A}$ is a $[\mathbf{3} \times \mathbf{4}]$ pose dependent structure matrix of *CDPM*, defined in Section 4.2.2 and $\boldsymbol{f}$ is $[\mathbf{4} \times \mathbf{1}]$ vector of cable tensions. As (4-45) is underdetermined, i.e. the structure matrix is non-square, the pseudoinverse of it, $(\mathbf{A}^T\mathbf{A})^{-\mathbf{1}}\mathbf{A}^T$, is used to find the solutions for the cable tensions. However, when using only the pseudoinverse approach, the solution set of cable tensions can still contain negative tensions. Therefore, the calculated set of cable tensions is further passed through the optimization routine to obtain optimized (positive) cable tensions. The objective is to minimize the sum of all the tensions satisfying (4-45) and the defined lower and upper bounds for the minimum and maximum tensions in *CDPM*, respectively. The *linprog* command in MATLAB [181] finds the minimum of a problem specified by:

$$\min_{x} f^T x \text{ such that } \begin{Bmatrix} A * x \ \leq b, \\ Aeq * x = beq, \\ lb \leq x \leq ub. \end{Bmatrix} \tag{4-46}$$

where *f*, *x*, *beq*, *lb* and *ub* are vectors of non-optimized tensions, optimized tensions, applied torques, lower and upper bounds, respectively, and *Aeq* is structure matrix.

4.5.1 Numerical Example

To validate the chosen optimization method, a numerical simulation, using IK and ID solutions of *CDPM*, has been implemented in MATLAB. The main model parameters used in the calculations and based on the average anthropometric human body data are listed in Table 4-3.

Table 4-3. The upper arm dynamic model parameters.

Length of the clavicle	L_1	20 cm
Length of the upper arm	L_2	22 cm
Mass of the arm	m	5 kg
Radius of the arm	r	5 cm
Radius of the upper arm cuff (cable connection points)	u	10 cm

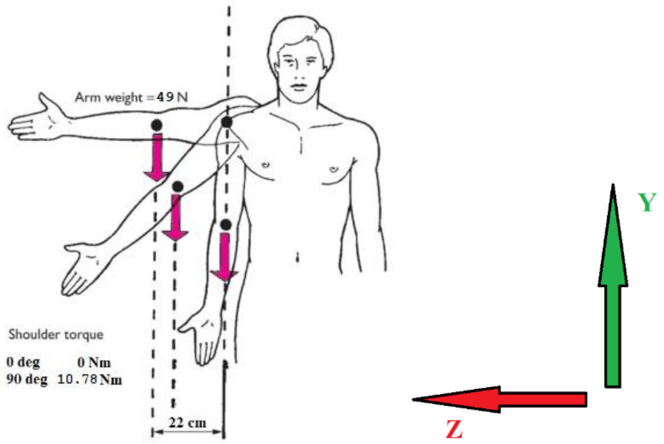

Figure 4-12: The angle-torque relationship during the shoulder abduction in *YZ* plane.

Figure 4-12 illustrates a shoulder abduction movement in the frontal plane of the human body (*YZ plane*). The torque required to elevate the arm in this plane, taking into account only gravitational force (in negative *Y*-axis), is around *X*-axis, $\boldsymbol{\tau} = [\tau_x, \quad 0, \quad 0]^T$.

For a given simple pose of *CDPM*, $\boldsymbol{q} = [\alpha, \quad \beta, \quad \gamma]^T = [0, \quad 0, \quad 0]^T$ (deg) – shoulder abduction of 90 deg. (please note that this pose corresponds to $\beta = 0$) in the frontal plane, the corresponding torque is calculated, $\boldsymbol{\tau} = [10.78, \quad 0, \quad 0]^T$ (Nm), using the dynamic and human model parameters (Table 4-3 and 4-44). This pose corresponds to the upper position of the arm in Figure 4-12. Also, from the given joint angle, a Jacobian, and then a structure matrix, **A**, is obtained using IK equations of *CDPM* from Section 4.2.2. The lower and upper bounds of cable tensions were arbitrary defined as 3 N and 20 N, respectively. The set of cable tensions before and after optimization algorithm are calculated in MATLAB, as follows:

The non-optimized vector of cable tensions: $\boldsymbol{f} = [43.12, 21.56, 32.34, -21.560]^T$ (N).
The optimized vector of cable tensions: $\boldsymbol{f}_{\mathbf{opt}} = [10.84, 9.67, 3.00, 12.94]^T$ (N).

As can be seen, the non-optimized tension vector contains negative values but the optimized tensions are positive within the defined bounds and satisfy the force-torque equation. To check the latter, the obtained set of optimized tensions is multiplied by the structure matrix at this pose, and the torque vector is obtained: $\boldsymbol{\tau} = [10.78, 0, 0]^T$, which is equal to the initially given torque vector. This validates the cable tension optimization implementation to solve ID problem of *CDPM*, which is crucial for performing proper force control experiments. Thus, it is possible to provide the certain torques for the "end-effector" of the *HRM* based on optimized tensions in *CDPM*.

Also, for some defined trajectory in the joint space, using both IK and ID equations of *CDPM*, the cable lengths and optimized positive tensions can be generated as functions of time.

4.6 Conclusion

The proposed hybrid mechanism has its merits compared to the conventional types of robots due to the hybrid structure and the cable-driven links. The redundancy of *CDPM* ($m > n$) avoids the singularities and enlarges the workspace of the parallel mechanism. A *CDPM*, which utilizes the human arm as a mechanical structure, is designed without rigid links and does not have specific revolute axes, so there are no joint misalignments between anatomical axes of the human joint and axes of *CDPM*. The parallel structure around the shoulder joint also contributes to this goal and provides the self-alignment with the spherical joint. As a result, it does not include additional motion constraints due to joint axes misalignments and does not restrict the natural motion of a human shoulder adding increased versatility and self-alignment characteristics. Also, cables under tension together with the human upper limb are considered as structural members of the proposed *CDPM*. Moreover, the non-fixed base of such fully restrained *CDPM* increases the overall workspace, dexterity, control over the stiffness and adds more functionality to the hybrid mechanism which can be advantageous in applications such as rehabilitation robotics. The 2-DOFs proximal module, designed as an inverted slider crank mechanism, also has a self-alignment feature as it can perform both actuated and passive motions to follow the coupled movements of the human shoulder girdle. The inner passive restraining links and outer active mechanism in the *HRM* can be regarded as human limbs and robotic exoskeleton, respectively. Such approach is advantageous in terms of avoiding the joint axes misalignments between the human and robot as the kinematic structure of the robotic mechanism is designed to follow the natural motions of the human joints. The self-alignment characteristic of the proposed *HRM* is evaluated by testing its motions (driving the links) in CAD simulation and using a built small-scale prototype.

Even though the hybrid mechanisms, in general, have more types of singularities to consider, the proposed mechanism for the shoulder rehabilitation does not suffer from any type of singularity within the workspace of the human shoulder. Moreover, the real human shoulder joint angles vary greatly among the individuals and are usually more limited than the selected ranges, especially for people suffering from neurological disability.

Finally, the designed bio-inspired *HRM* can be referred as anthropomorphic mechanism, where the pulling cables and inner passive restrained links act like human muscles and limbs, respectively. The kinematics and designs of different 4-bar mechanisms can be employed to model the coupled human-robot structures, e.g. when connecting a robotic exoskeleton to a human limb with one or two DOFs. In this regard, the potential field of applications of such *HRM*s is robotic rehabilitation of multi-joint human limbs, where independent segmental control of the joints can be achieved.

Chapter 5

Prototype Development of HYBRID-SRE

5.1 Introduction

This chapter provides an overview of a developed real-scale prototype of a robotic shoulder rehabilitation exoskeleton and its hardware components. Its mechanism design is based on the 5-DOFs hybrid *HRM* analysed in Chapter 4 - hence the name HYBRID-SRE. The main structural components of HYBRID-SRE (Figure 1-1) presented here are: support structure and actuation, shoulder cuff and upper arm cuff. The simple control diagrams and the main hardware loop of the developed set up are also illustrated in this chapter.

5.2 Specific Considerations

As there is no single recipe for constructing ideal robotic prototype of shoulder rehabilitation exoskeleton, the following is the list of some specific considerations that can be addressed at the development stage:

- Will the robotic exoskeleton be a stationary set up oriented for clinical setting or a wearable orthosis for home use?
- Will it support one or both upper arms (unilateral or bilateral)?
- Will it be a fully passive device or actuated, or combine both passive and active joints?
- For how many and to which shoulder DOFs it will be able to provide assistance (passive/active)?
- What will be the kinematic structure of the mechanism (serial, parallel, hybrid)?
- What kind of links (rigid, tendon, combined, soft) it will consist of?
- What type of actuation (electric, pneumatic, hydraulic, SEA) will be implemented?
- What type of sensors it will be equipped with?
- From what kind of materials it will be made of?
- What will be its overall weight applied to the human body?
- What mechanical and software solutions will be implemented for safety?
- What parts of it will be adjustable to adapt to different sizes?
- What kind of control hardware and software can be used?

- What kind of control strategies will be more suitable to utilize?
- How much will it cost to produce such a prototype?
- What will be its appearance when worn on patient?
- What other technological advancements can be employed: machine learning tools, brain interfaces, additional sensors/stimulators on human body?

Therefore, the prototype development stage started with analysing and understanding the answers of these questions. As robotic exoskeletons interact closely with the human body, it is also important to overview the existing safety, quality, technical and product certification standards used in the field of rehabilitation robots. As this field is relatively new, there is still not a single standard that can cover all the design and performance aspects of robotic exoskeletons used in rehabilitation. However, there already exist several related useful ISO standards worth to consider, as follows:

- *ISO 13482 - Robots and Robotic Devices – Safety requirement for personal care robots*. This standard provides a comprehensive overview of the safety requirements for robotic devices. The standards for one of the considered types of personal care robots, namely restraint type physical assistant robots (that is fastened to a human during use), can be partially applied to the robotic exoskeletons.
- *ISO 12100 - Safety of machinery – General principles for design – Risk assessment and risk reduction*. This standard can be used to undergo the risk assessment of the developed prototype.
- *ISO 15066 – Collaborative Robot Technical Specification*. This standard is not extended to address the robotic exoskeletons but it provides useful information (forces, stiffness, speeds, etc.) for specific human body parts which can then be used as a benchmark values while considering safety issues (from ISO 13842).
- *IEC 60601-1 - Medical Electrical Equipment*. As the use of rehabilitation robots involves humans, they fall under the domain of medical robots. This standard defines the main safety and performance requirements for medical electrical systems. In addition, it also contains reference test methods to verify the safety needs. Note that the ISO 13482 standard does not apply its specified safety guidelines to robots as medical devices.
- *ISO 80601-2-78 – Particular requirements for basic safety and essential*

performance of medical robots for rehabilitation, assessment, compensation or alleviation. This standard, being the extended part of standards on medical robots, is the most recent (upcoming) and the most relevant standard that specifically addresses the use of rehabilitation robots. It considers the robotic devices that can perform "actively controlled physical interactions" to a patient and is intended to determine the load restrictions, actuator requirements and other essential performance specifications. Unfortunately, its status was still "under development" when requested by the author.

As there is a number of the developed standards related to the use of the robotic devices, it is not practical to follow all of them when dealing with rehabilitation robotic exoskeletons, as long as the relevant specific considerations have been made and other reasonable evaluations have been performed.

5.3 Support Structure and Actuation

First of all, the proposed HYBRID-SRE is designed as a stationary sitting set up oriented for use in clinical setting. As one of the main objectives is to develop an exoskeleton with lightweight modules, all the heavy electric actuation units are mounted on the strong support structure behind the human body to reduce the overall weight on human limbs. The support structure is made of steel and fixed on the floor for stability. A simple chair is placed on the fixed base to simulate the clinical setting device.

Shoulder Girdle Module. The Shoulder Girdle Module (*SGM*), shown in Figure 5-1, corresponds to a 2-DOFs proximal module of the hybrid *HRM* in Chapter 4, Section 4.2.1. The first rotational drive R_1, which is meant to assist the shoulder girdle elevation/depression (E/D) movement, is mounted on the fixed support structure on the back and its initial position can be manually adjusted along the horizontal and vertical axes according to the subject's dimensions. The second rotational drive R_2, for the shoulder girdle protraction/retraction (P/R) movement, is linked to the first one so that the axes of two rotational drives around which they rotate intersect forming the active universal joint of the *HRM* from Chapter 4 with two revolute angles (ψ_1, ψ_2). This actuated linkage is further serially rigidly connected to the shoulder cuff through a passive prismatic slider that corresponds to the passive joint described in Section 4.2.1. As a result, the *SGM* provides full assistance for the shoulder girdle movements, follows the shifting position of the human shoulder joint, and due to combination of active/passive joints resolves the kinematic discrepancy caused by the distance between the robot structure and human body. Each of the rotational drives is comprised of motor, encoder and planetary gearhead (from *Maxon Motor*). Their rotations are restricted using mechanical stops at the motor holders according to the real maximum ROM of the human shoulder girdle motions (-45 to 45 deg. rotation).

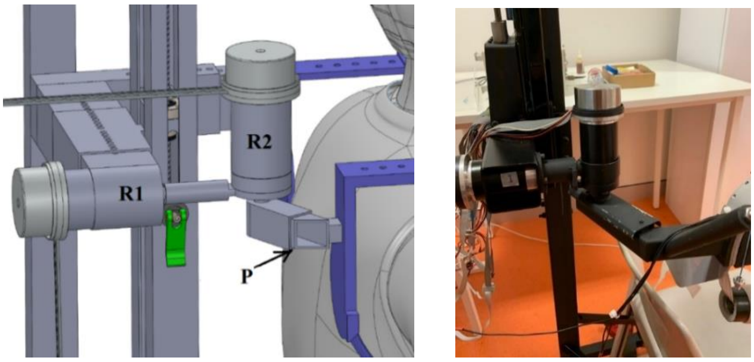

Figure 5-1: Shoulder Girdle Module: CAD model and the built prototype.

Linear Drives actuation system. The linear drives used to actuate the four cables of 3-DOFs *CDPM* module are mounted on the back of the support structure, as shown in Figure 5-2. The active cables provide the pulling forces from the top, passing through the cable connection points on the shoulder cuff to the cable connection points on the upper arm cuff. The cable connection points are made as “spherical” joints by placing a little 3D printed part inside, as shown on the right in Figure 5-2, so it can be easily replaced in case it wears out. Each of the linear drives is comprised of motor, encoder and ball screw spindle (from *Maxon Motor*). Their range of motion is limited by the length of the spindle shafts which was estimated based on the needed cable lengths between the shoulder and upper arm cuffs.

Figure 5-2: Linear drives actuation system of HYRBID-SRE.

All the drives (rotational and linear), selected by considering their gear ratios, output nominal speed, force and other motor characteristics, were properly wired through the motor controllers to the DAQ board for real-time control from a PC. In order to perform different experimental trials and performance evaluation of the developed set up, the preliminary tests were conducted first such as establishing a controller for each actuator.

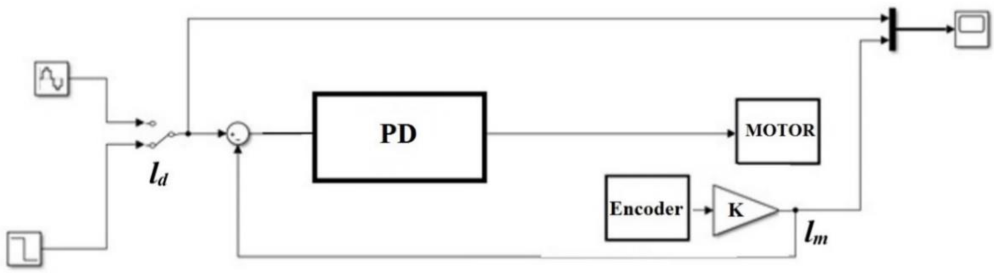

Figure 5-3: The PD position control diagram for each actuator.

First, each of the rotational and linear actuators of HYBRID-SRE was controlled using a simple PD controller shown in Figure 5-3. As the desired input for the rotational actuators is in degrees, the encoder pulses are converted into the degrees using this specific gain, $K_{\text{rotational}} = \frac{360°}{4*1024(puls)*126}$. Similarly, as the inputs for the linear actuators are the cable lengths (cm), the encoder pulses are converted into the corresponding unit of cm using this specific gain, $K_{\text{linear}} = \frac{1}{4*1000\left({}^{puls}/_{rev}\right)*2.4\left({}^{rev}/_{mm}\right)*10\left({}^{mm}/_{cm}\right)}$. The gains of the PD controller were experimentally determined to be K_p = 8.5 and K_d = 0.42 (with filter coefficient N = 500) for all actuators.

5.4 Shoulder Cuff and Force Sensors

The shoulder cuff, shown in Figure 5-4, is actuated by the *SGM* and it sits on the human shoulder just above AC and GH joints. It is designed as an arc cuff that can be adjusted to different shoulder dimensions with the inner foam material for comfortability. The designed and fabricated robotic shoulder cuff can also be moved up/down or to the left/right along the fixed support, depending on the user's height and shoulder width. The shoulder cuff also serves as a base platform for *CDPM* module with extended links for cable connection points. These extended variable-length links can also be adjusted on the cuff at different positions/angles so that the location of cable connection points (cable routing) can be adjusted accordingly, if needed [182]. The base cable connection points of *CDPM*, (B_1, B_2, B_3), are shown in Figure 5-4(b).

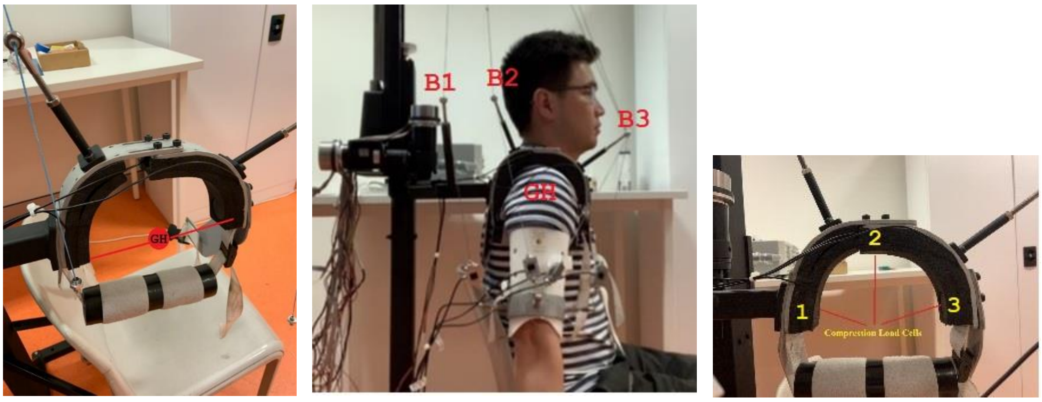

(a) (b) (c)

Figure 5-4: Shoulder cuff of HYBRID-SRE. (a) Shoulder cuff prototype, (b) Cable connection points on the shoulder cuff, (c) Force sensors enclosed inside the cuff.

The shoulder cuff is developed for the human right arm and has a deformable aluminium plate in front to strap it around the body under the left arm for torso stabilization. It is also equipped with three 1-axis compression force sensors, placed in the inner part of the cuff at the locations shown in Figure 5-4(c). These force sensors can measure the interaction forces between the human shoulder and the robotic shoulder cuff. The force sensors 1 and 3, on the front and back sides of the inner shoulder cuff, are used in the shoulder girdle P/R motions while the force sensor 2, on the top of the inner shoulder cuff, is used to sense the shoulder girdle elevation.

It is worth mentioning here that the robotic *SGM*, connected to the two rotational actuators at the fixed support base, can be moved in a number of different ways:

• Passive movement (no actuation): this is achieved due to the full back drivability of the rotational actuators even when the actuators are turned off.

• Actuated movement: the rotational actuators are actuated:

- Position Control is achieved using a simple PD controller loop for each motor independently, shown in Figure 5-3.

- Zero-Force Control. This simple control scheme requires the feedback from the force sensors inside the shoulder cuff. By implementing such a zero-force control algorithm, the *SGM* can be actuated in real time (e.g. with a defined constant speed, depending on the therapy) once the shoulder cuff senses the applied force (above certain threshold on individual basis) from the human shoulder girdle. Such type of zero-force control is favorable due to the fact that this kind of guarded motion can be considered as a real-time following of the center of the human spherical shoulder joint, which is very important when dealing with issues of human-robot interactions in the shoulder exoskeleton.

5.5 Upper Arm Cuff and Tension Load Cells

The upper arm cuff, shown in Figure 5-5, is made from the purchased orthotic brace used in rehabilitation, which comfortably and tightly wraps the upper arm of different sizes. A semicircular metallic cuff is attached on that brace to locate the cable connection points, (U_1, U_2, U_3), of *CDPM* module. Four tension load cells (S-type) are connected along the four actuated cable lines close to the metallic cuff (end-effector of *CDPM*) to provide the cable tension measurements for experimental purposes. As can be seen, the developed shoulder and upper arm cuffs correspond to the base and moving platform of *CDPM* in the *HRM* proposed in Chapter 4.

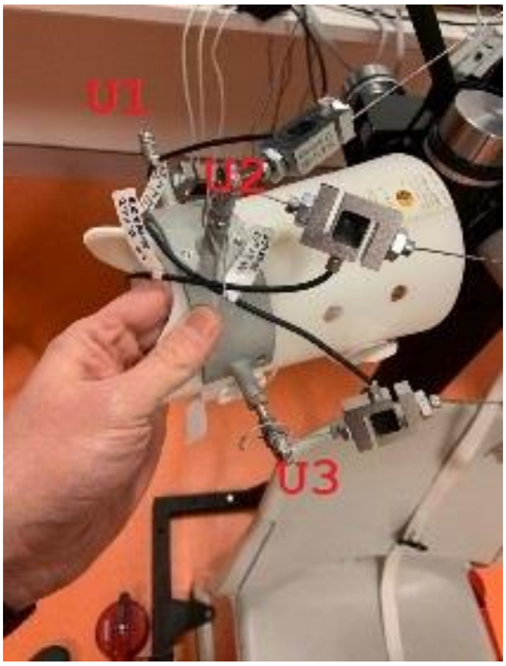

Figure 5-5: The upper arm cuff of HYBRID-SRE.

As *CDPM* of HYBRID-SRE is equipped with tension load cells, their force feedback can be used to implement a simple tension controller for each cable. Hence, an additional tuning of cable tension was performed independently for each cable using the corresponding linear actuators of *CDPM* with a PID controller, shown in Figure 5-6.

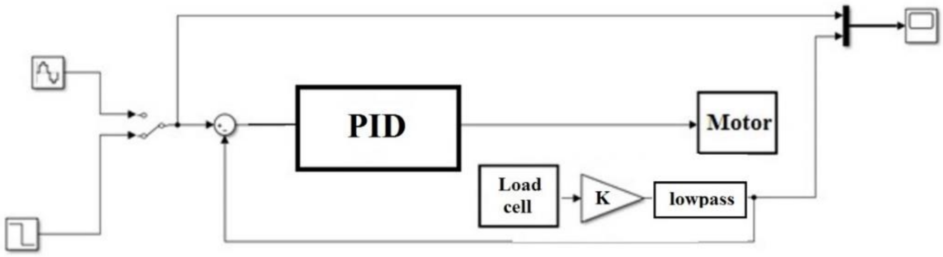

Figure 5-6: The PID cable tension controller diagram based on the tension load cell data.

The input is the desired cable tension value (N) and the load cell's output is converted, according to its specifications, through the corresponding specific gain, $K_{\text{tension}} = -\frac{20kg*9.8(^{m}/_{s^2})}{5.4V}$, into the measured cable tension (N) followed by the low-pass filter. The proportional, integral and derivative gains were obtained through experimental trials: K_p = 3.15, K_i = 2 and K_d = 0.25 (with filter coefficient 500). The step response of one of the cables' tension is shown in Figure 5-7 with the arbitrary chosen value of 2 N. This tension controller was used to achieve a specified input tensions in each individual cable during the performance evaluation of the developed prototype, e.g. to pretension the cables of *CDPM* to initial values at the reference pose.

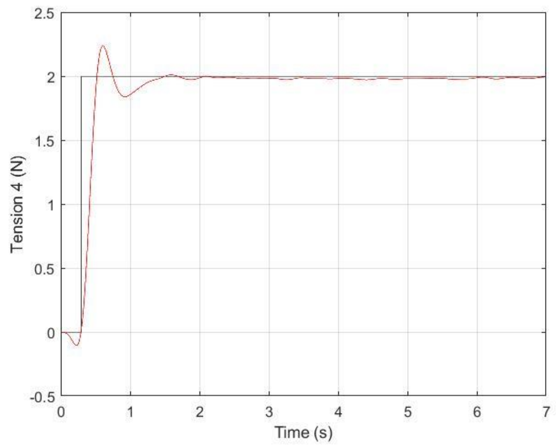

Figure 5-7: The step input response for one of the cable tensions (reference vs measured).

The tensions in the cables of *CDPM* are increased by pulling the cables with the corresponding linear actuators. Therefore, it is also possible to implement a simple control scheme for each actuator satisfying the minimum positive tension (lower bound), using the feedback data from the tension load cell in addition to the position feedback from the encoder, as shown in Figure 5-8.

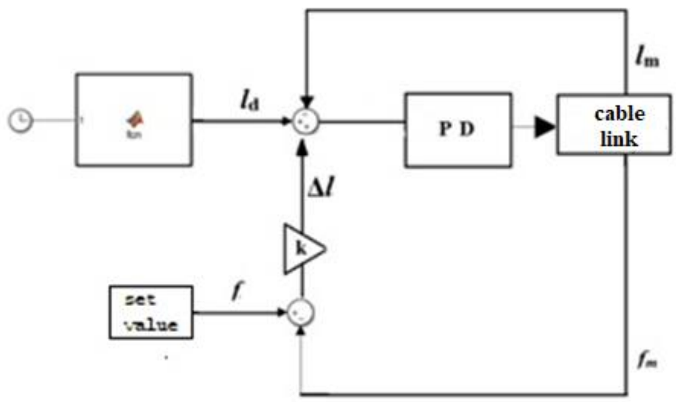

Figure 5-8: Position-based impedance controller of cable link

The feedback data from the tension load cell is used to find the tension error (set lower bound minus measured), which is then multiplied by *k*, an experimentally obtained stiffness constant that relates the change in cable tension to the change in cable length (linear relationship), to obtain a corresponding change in cable length. This adjusted length command, *Δl*, is then added to the set cable lengths before the

PD block of the individual position control diagram. Also, a simple intermediate switch block (not shown in the diagram) was added to prevent the extra cable pulling if the tension error is negative, i.e. the measured tension is above the minimum set value. The overall control is still governed by the position loop but it also adapts to satisfy the minimum positive tensions along the desired trajectory (given in the joint space).

Using the IK of *CDPM*, the changes of four cable lengths are calculated from the given joint space trajectory (set of the human shoulder angles $\boldsymbol{q}$), and used as inputs for individual (separately for each motor) position controllers. As a result, two simple controllers of *CDPM* are defined as follows:

- *Position Controller* (PC) – simultaneous actuation of four linear actuators with purely position PD controller (Figure 5-3) for each actuator w/o any force feedback from the tension load cells.
- *Position-based Impedance Controller* (PIC) – position-based impedance controller (Figure 5-8) with feedbacks from both position encoders and tension load cells.

5.6 Control Hardware

All hardware (actuator drives, servo controllers, load cells, amplifiers, electrical connections, etc.) were accurately assembled and connected to the data acquisition QPIDe terminal board (from *Quanser*) which is controlled by MATLAB/Simulink (*QUARC Real-Time Control*) software installed on PC. The "ESCON Studio" user interface for ESCON servo controllers (*Maxon Motors*) was used to enter the individual motor parameters and control modes (speed/current).

Input channels used (QPIDe board):
- 6 encoder inputs (4 linear drives + 2 rotational drives)
- 7 analog inputs from various sensors (4 tension load cells + 3 compression force sensors)

Output channels used (QPIDe board):
- 6 digital outputs to turn on/off motors (+ 6 to change the direction CW/CCW)
- 6 analog outputs to control the drives (4 linear + 2 rotational).

The overall hardware loop of HYBRID-SRE is shown in Figure 5-9.

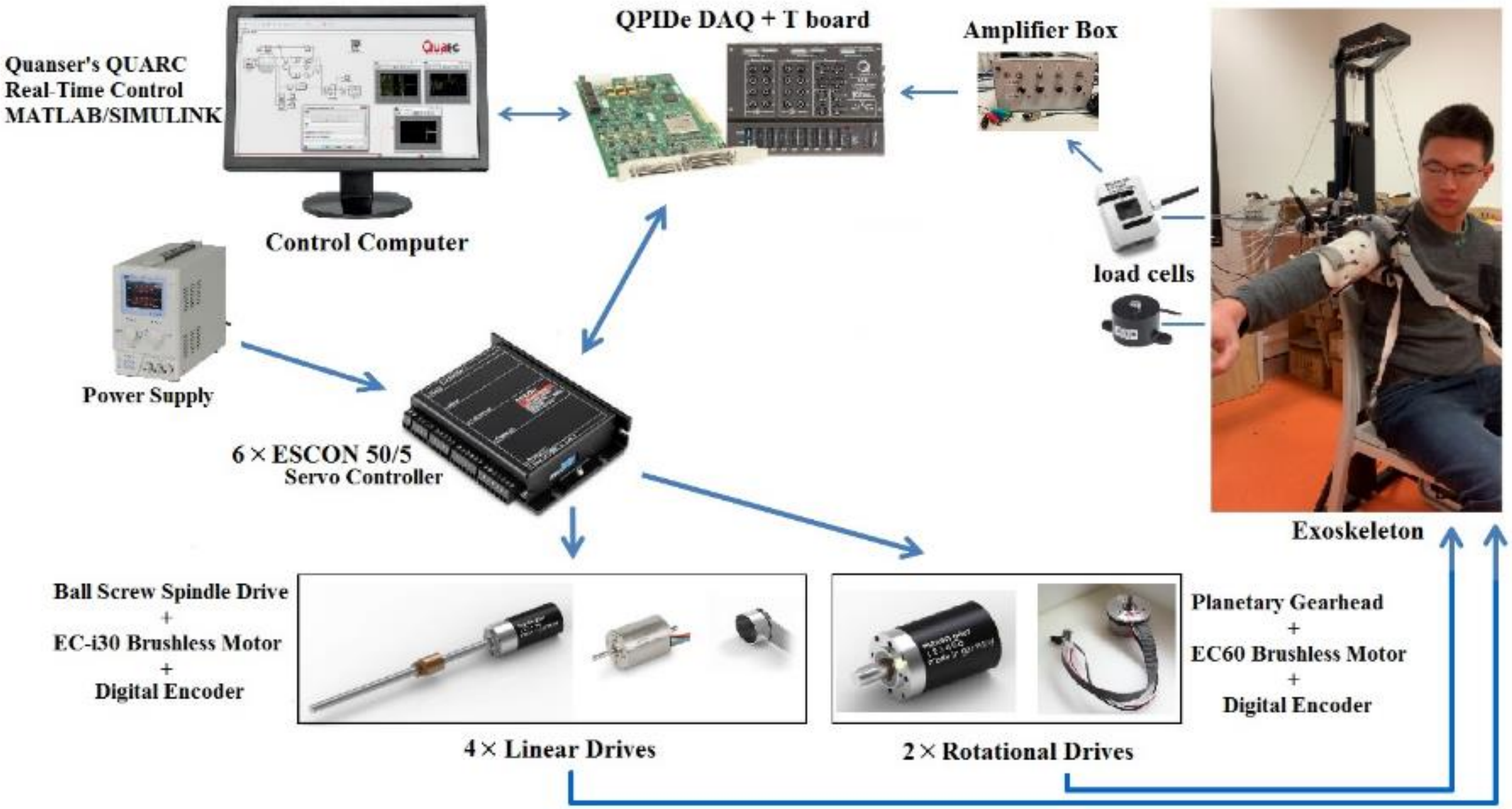

Figure 5-9: The main hardware loop of HYBRID-SRE

The main CAD assembly of HYBRID-SRE with its components' specifications are provided in Appendix A.2.

5.7 Discussion and Conclusion

This chapter presents the first implementation of the developed HYBRID-SRE prototype. The actuation system is external to exoskeleton and fixed supports carry the device weight, which allows more wearability for the user. The symmetrical support structure on the back consists of modular parts that can be replaced to switch the whole set up from the right arm to the left arm with some further modifications.

The electric actuation is chosen for both sub-mechanisms of HYBRID-SRE. In particular, the back-drivable rotational drives mounted on the fixed support are used to actuate the shoulder cuff and linear drives are used to actuate the cable-driven module. The HYBRID-SRE is referred as an exoskeleton with lightweight modules due to the lightweight cuffs that are directly attached to the human limbs and due to the lightweight cables (instead of rigid links) routed through the cuffs to the motors mounted on an external fixed frame. In this manner, less weight is applied to the human body and it is considered as a stationary set up so that its total weight is not comparable to the wearable or portable exoskeletons. By pulling on the cables using motors, torques can be generated at the shoulder joint. The stronger the cables, the less unwanted motion or vibration they will exhibit, and the choice of cables (elasticity, diameter, material) is also important due to safety issues as they operate close to a human body.

Table 5-1 compares the proposed HYBRID-SRE with some of the existing cable-driven shoulder rehabilitation exoskeletons reviewed in Chapter 2. In addition to the type of actuators, the cable-driven exoskeletons also differ in transmission types they utilize. Due to the parallel placement of cable connection points (without any specific revolute axes) exoskeletons, such as CAREX and HYBRID-SRE, do not suffer from the joint axes misalignments which improves their ability of self-alignment. Moreover, the overall workspace of HYBRID-SRE is further increased by the moving *SGM* when compared to the fixed shoulder cuff in CAREX exoskeleton. Thus, in comparison to other existing cable-driven exoskeletons, the developed HYBRID-SRE can assist all main 5-DOFs shoulder.

Table 5-1. Comparison Table of some of the existing cable-driven exoskeletons.

Name	Type of actuator	Actuation unit	Transmission type	Shoulder DOF
CADEN-7 [35]	Rotatory electric	External (serial)	Close cable pulley transmission	3-DOFs
ABLE [61]	Rotatory electric to linear ball screw	External on body (serial)	Close cable-pulley with linear configuration	3-DOFs
IntelliArm [41]	Rotatory electric	External (serial)	Close cable pulley transmission/Capstan	4-DOFs
CAREX [37]	Rotatory electric	External frame (parallel)	Motorized reel to anchor points	3-DOFs
HYBRID-SRE	Rotatory electric to linear ball screw	External frame (parallel)	Motorized cable to anchor points	3-DOFs (cable-driven) + 2-DOFs (rigid linkage)

As the linear drive is chosen for the actuation of *CDPM*, the length of the linear ball screw is selected according to the cable length range between the shoulder and upper arm cuffs. The compact 1-axis compression sensors are selected so that they can comfortably fit in the inner part of the designed shoulder cuff. The tension load cells are selected so that they can be placed along the cables close to the upper arm cuff. Both cuffs, force sensors and their connections can further be upgraded to make them even more comfortable, lightweight and suitable for rehabilitation purposes.

HYBRID-SRE actuates indirectly shoulder girdle and shoulder joint by positioning each link in a desired position. The indirect actuation allows the joints to accommodate their centers of rotation. Proper generation of feasible trajectories can give the required variable force and deal with the non-linearities generated by the friction within joints and cables. Two basic position based control strategies, described in this chapter, are implemented to test the performance of the developed exoskeleton.

There are many trade-offs in robotic system and there is no ideal choice for its components. Each part of HYBRID-SRE is constructed with adjustable features to accommodate various dimensions and to implement further design optimization.

Chapter 6

Performance Evaluation of HYBRID-SRE

6.1 Chapter Overview

This chapter reports on the main experimental work with HYBRID-SRE: workspace evaluation using additional sensors (Xsens), trajectory tracking experiments and independent/coupled motions of shoulder DOFs. The experimental procedures and outputs are followed with discussion in the corresponding paragraphs.

6.2 Specific Questions

As HYBRID-SRE is developed to provide support to the motions of the affected upper limb, it is also important to address more specific questions when evaluating its performance, as follows:

- Can the exoskeleton appropriately support the required motion, both with and without loading? And what is the difference, from human perspective, between the motion with and without the robotic exoskeleton?

- What is the ROM of the patient's upper limb, both with and without wearing the exoskeleton?

- How accurate is the trajectory tracking and what is the pose uncertainty during the repeatable motions?

- Is the actuation system back-drivable? Can the patient move the robot freely when it is not driven?

- How comfortable is the attached robotic device and posture of the patient when undergoing therapy trainings?

- Is it easy to put on/put off the exoskeleton?

- How easy it is to implement a simple initial training and control of the exoskeleton?

6.3 Workspace Evaluation

This section presents the workspace verification of the developed exoskeleton using Xsens Technology [183].

(a) (b)

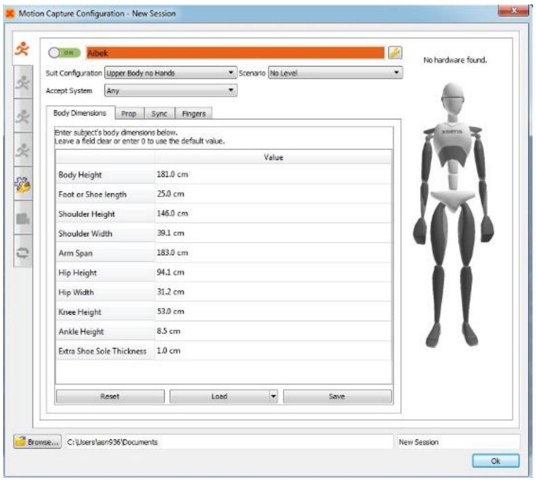

(c)

Figure 6-1: (a) Xsens trackers on the front; (b) Xsens trackers on the back; (c) The body parameters.

The Xsens Motion Capture Technology was used to compare the ROM of the developed HYBRID-SRE prototype to the ROM of the healthy human's shoulder. It is also later used to verify the kinematics of HYBRID-SRE during different control experiments. The upper body of the healthy participant was equipped with the motion trackers as seen in Figure 6-1(a,b). The measured body dimensions of the upper body (Figure 6-1c) were entered into the software followed by the calibration of the motion capture system.

First, the participant, wearing the Xsens suit with motion trackers, performed various common shoulder motions without being attached to the exoskeleton. All motions were performed twice starting and ending at the initial sitting pose. The recorded motions (of the right arm) are:

- Shoulder abduction/adduction (A/A) in the coronal plane to its max
- Shoulder flexion/extension (F/E) in the sagittal plane to its max
- Horizontal flexion/extension (HF/HE) in the transverse plane to its max
- Butterfly-like trajectory
- Circular-like trajectory
- Shoulder elevation/depression (E/D) (shoulder girdle movement only)
- Shoulder protraction/retraction (P/R) (shoulder girdle movement only)

Then, it has been possible to extract the measured data, namely, the position and joint angles of the right arm segments during the performed shoulder motions. As the human arm was also equipped with the forearm tracker and it was held stretched without bending the elbow, the 3D Cartesian position data of the forearm tracker w.r.t the sternum (T8 human bony landmark) was chosen to be extracted and plotted to illustrate the enlarged workspace of the shoulder motions. The global coordinate system of the Xsens trackers is shown in Figure 6-2a. Note that, the *X*-axis of the Xsens frame is aligned with the *X*-axis of the frame used in this work, while the *Y* and *Z* axes are aligned with -*Z* and *Y* axes, respectively. Hence, the sequence of the Euler angles in Xsens differ from the adapted sequence of the shoulder joint angles.

The 2D (back view) and 3D representations of the shoulder A/A motions (repeated twice) in the coronal plane are shown in Figure 6-2(b,c), respectively.

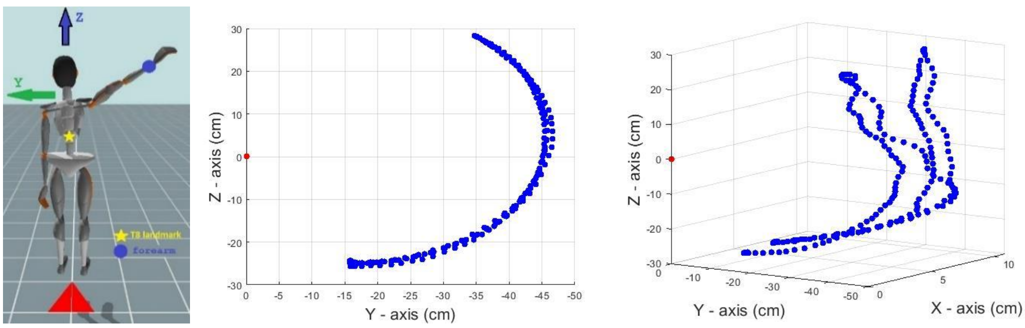

(a) (b) (c)

Figure 6-2: (a) Xsens coordinate system. (b,c) Shoulder A/A (back view, 3D view).

The extracted Xsens data (position of the forearm tracker) during the shoulder F/E (in the sagittal plane) and HF/HE (in the transverse plane) motions are plotted in Figure 6-3 and Figure 6-4, respectively.

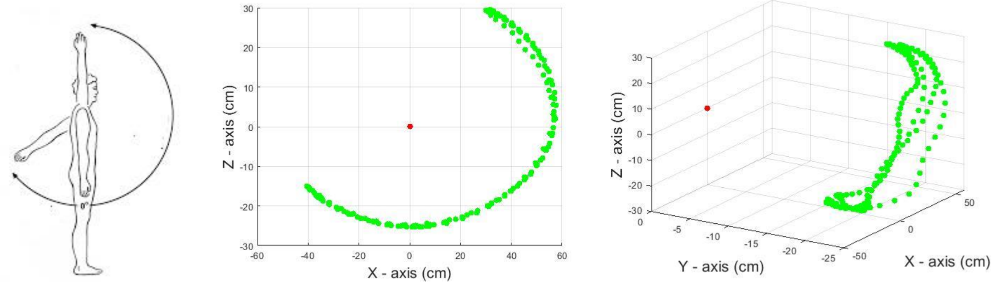

Figure 6-3: Shoulder flexion/extension motions.

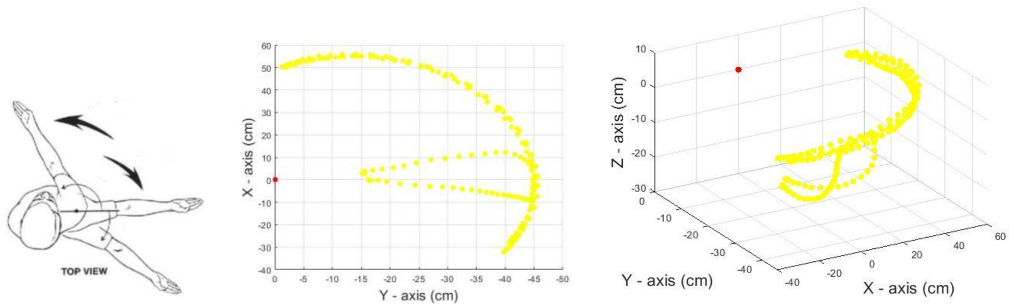

Figure 6-4: Shoulder horizontal flexion/extension motions.

The combined 3D plot of the main shoulder motions together with the other tested motions (butterfly and circular) is shown in Figure 6-5 from two different angles of view.

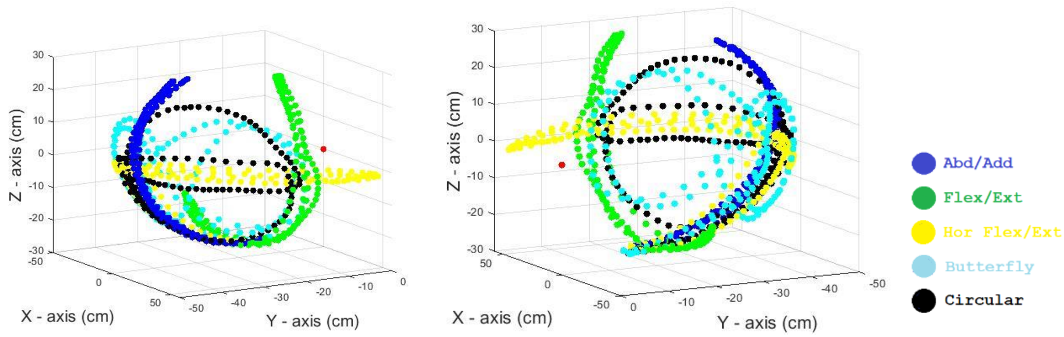

Figure 6-5: The combined plot of different shoulder motions.

The independent shoulder girdle motions, namely, shoulder E/D and shoulder P/R, were also performed and recorded using Xsens technology. The position data for the right upper arm segment (instead of the forearm) were used to represent the tested shoulder girdle motions. To plot and distinguish the limited range of the shoulder girdle movements, all the previous motions were colored in one color (blue), as shown in Figure 6-6.

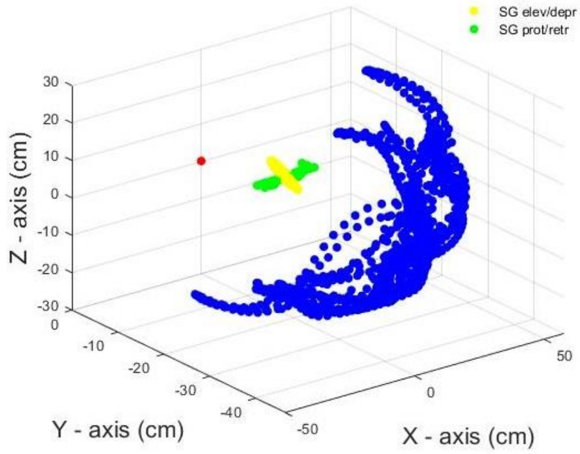

Figure 6-6: The 3D plot of all shoulder motions w/o exoskeleton: shoulder E/D (yellow), shoulder P/R (green) and all other tested motions (blue).

To test the ROM of the developed exoskeleton, the healthy participant, wearing the Xsens suit with motion trackers (Figure 6-7(a)), repeated the same motion patterns while being attached to HYBRID-SRE (with no actuation) with the fully back-drivable shoulder girdle mechanism (shoulder cuff). In the similar manner, the right forearm tracker positions were recorded and extracted for the shoulder motions, and the right upper arm tracker positions were used to generate the shoulder girdle motions. The position plot of the subject's right upper arm motions while wearing the exoskeleton is shown in Figure 6-7(b).

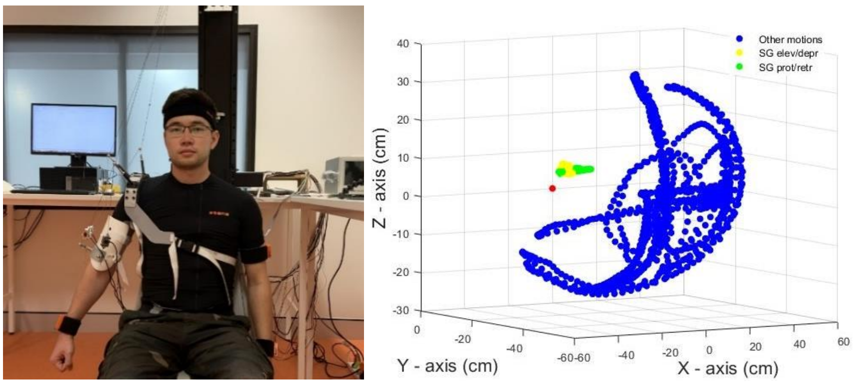

(a) (b)

Figure 6-7: (a) A test subject wearing Xsens motion trackers; (b) The 3D pose of the right upper arm during the tested motions.

The combined plots of the Cartesian position of the right arm during the motions with and without HYBRID-SRE are shown in Figure 6-8.

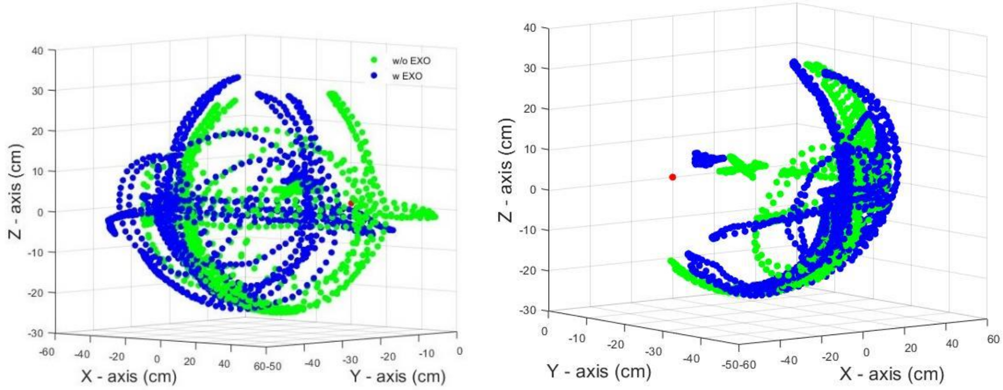

Figure 6-8: The combined workspace plots from different angles of view with (in blue) and without (in green) HYBRID-SRE.

At first sight, it may seem that they did not perfectly match each other and it was reasonably expected due to several reasons and issues:

- The calibration of Xsens sensors were performed at the location where the trials without exoskeleton were conducted while the experiments with exoskeleton were measured at the robotic set up (in a different spot in the Lab).

- The initial XYZ coordinates of the motion trackers w.r.t the global coordinate system were shifted in between the trials (with and w/o exoskeleton).

- As the experiments were performed by a human, the motions were not repeated in an exact same way (especially more complex ones) and in the exact same period of time.

- The motion trackers on the upper body could have also slightly moved during and between the tested motions.

- The self-rotation of the upper arm around its axis also affects the orientation of the tracker.

- Xsens errors, electrical noise next to the exoskeleton set up and other issues.

Nevertheless, even though it looks like the position workspace plots differ a bit, the actual position error is within just a couple of centimeters. Moreover, during the testing, all the tested shoulder motions were reached and there was no position from the trial without the exoskeleton that were not reached when wearing the exoskeleton. Also, the participant did not experience any considerable discomfort during the trials and could perform all the motions with minimum resistance due to the lightweight structure of the exoskeleton. Even though this generated set of points is not a complete workspace of the human shoulder, it still covers a good portion of it with the main shoulder motions used in the daily activities.

In addition to the recorded positions of the motion trackers, the shoulder joint angles were also measured (by Xsens) during all the tested motions. The comparison plots of the shoulder A/A, F/E and HF/HE angles during the two separate trials (with and without the exoskeleton) are plotted in Figure 6-9(a,b,c), respectively.

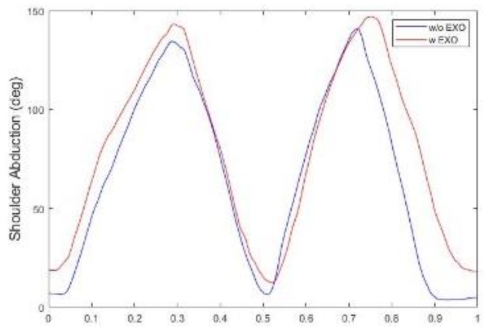

(a)

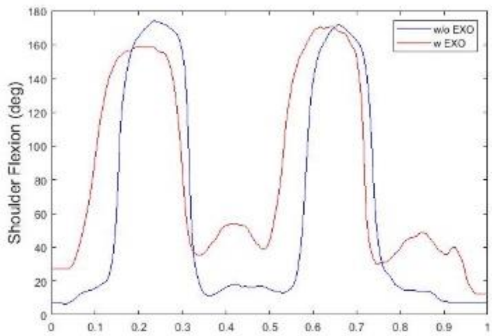

(b)

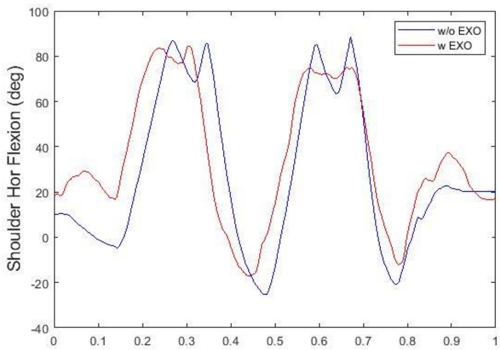

(c)

Figure 6-9: The comparison of the joint angles during the main shoulder motions with and w/o exoskeleton.

There can be seen inevitable shifts between the measured shoulder angles on the comparison plots in Figure 6-9. These offsets are due to the same listed reasons that correspond to the differences in the position plots in Figure 6-8. Still, it can be confidently claimed that the ROM of the developed HYBRID-SRE is sufficient to cover the ROM of the healthy human shoulder. It is worth noting that the moving shoulder girdle module with its self-alignment characteristics plays an important role in the enlarged workspace of the exoskeleton.

6.4 Initial Position

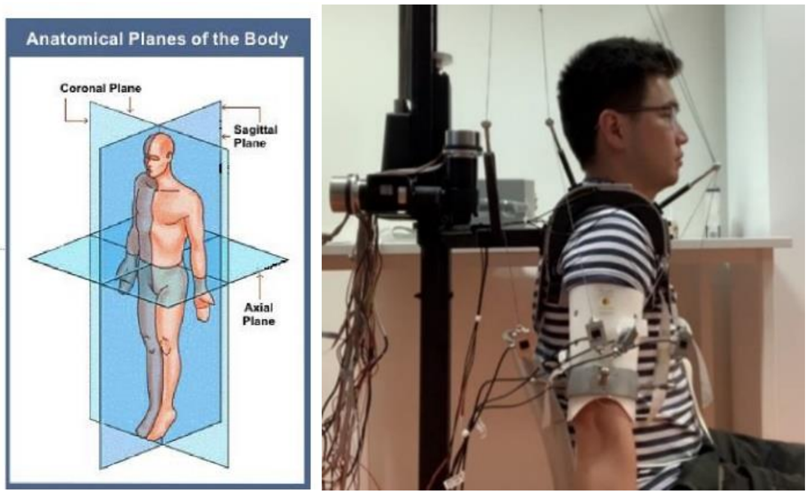

(a) (b)

Figure 6-10: (a) Human Body Planes; (b) Initial Pose.

To conduct a set of experimental case studies, the initial parameters and pose were defined as follows. The initial position: the subject is in sitting pose, the upper limb parallel with the body, palm faces the sagittal plane, as shown in Figure 6-10. This starting position corresponds to the following pose in the joint space, $\boldsymbol{q_{initial}}$ = $(\theta_1, \theta_{2,}\, \alpha, \beta, \gamma)^T$ = $(0, 0, 0, 90, 0)^T$. The reference cable lengths are obtained using IK of *CDPM* at this initial pose: l_{ref} = [45.9, 44.3, 42.5, 39] ^{T} (cm). The initial minimum cable tensions in *CDPM* module are defined as: $[f_1, f_2, f_3, f_4]^T$ = [0.5, 0.5, 0.5, 0.5]^T (N) and they are used as the lower bounds in the tension optimization solver. The initial input tensions were controlled using the tension controller (Figure 5-6) for each cable independently prior to each trial by such initial *pretension step* to achieve the reference pose. The main human arm model parameters, listed in Table 4-3, were used in the kinematic and dynamic models of the developed exoskeleton.

6.5 Trajectory Tracking Experiments

After conducting all the preliminary tests, which included the tuning of the individual position/tension loops, verification of the tension optimization solver, and defining all the initial parameters, HYBRID-SRE prototype was set ready to perform the set of basic control experiments. In order to test the basic position controllers, a set of experimental case studies were performed starting from the most common shoulder motions and expanding to the more complex trajectories (e.g. butterfly shape like trajectories). The tested motions involved both independent and coupled motions of the sub-mechanisms of HYBRID-SRE. All the experimental trials were conducted with the Xsens suit on for verification purposes. Two simple controllers, defined in Section 5-5, were employed in these trials: namely, *Position Controller* (PC) and *Position-based Impedance Controller* (PIC), shown in Figure 5-3 and Figure 5-8, respectively.

One of the main shoulder motions, crucial for activities of daily living and the most practiced in rehabilitation therapies [27], the shoulder abduction of 90 deg., was used as *Trajectory 1* (Traj.1) for testing purposes. As the shoulder cuff is fixed for this case, the inputs for the actuators in charge of the shoulder girdle were set to zero: $\theta_1 = \theta_2 = 0$. The abduction movement in the frontal (*YZ*) plane implies the change only in the orientation joint angle β. Thus, the joint space trajectory was planned from the initial pose $\boldsymbol{q_s}$, to the final pose $\boldsymbol{q_f}$, in a time interval of 10 seconds, with zero initial and final velocities (and accelerations).

Trajectory 1 – Shoulder Abduction:

$\boldsymbol{q_s} = (0, 0, 0, 90, 0)^T \rightarrow \boldsymbol{q_f} = (0, 0, 0, 0, 0)^T$ specified time (t =10 s)

Figure 6-11(a,b) shows the changes in cable lengths (reference vs measured) and cable tensions of *CDPM* during Traj. 1 from PC control trial. As expected, it can be seen that the measured cable lengths perfectly matched the reference cable lengths of *CDPM* (Figure 6-11(a)). In fact, only two cables (Cables 2 and 3) are enough to lift the arm to this desired pose from the reference position due to their symmetrical placement about the motion plane. Therefore, the weight of the arm during the tested motion was distributed between these two cables, as shown in Figure 6-11(b), while Cables 1 and 4 were held at low tension during PC control of

Traj. 1. It can also be seen, that pretension step of Cable 1 was not properly achieved or disturbed prior to this control trial.

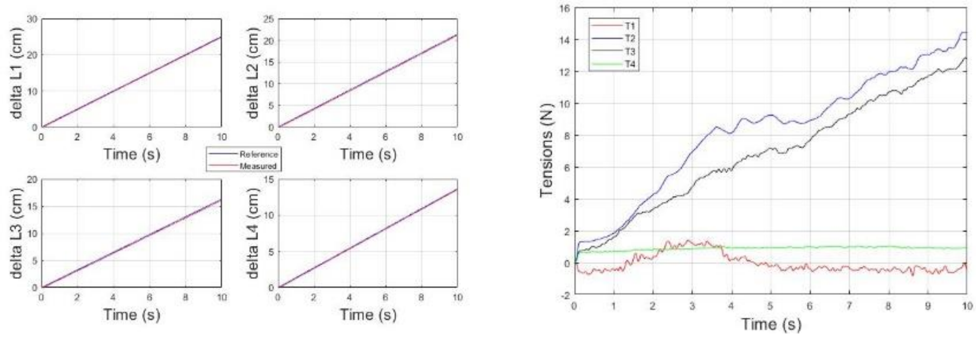

(a) (b)

Figure 6-11: PC control of Traj. 1. (a) The changes in cable lengths of *CDPM* (reference vs measured). (b) The cable tensions.

To ensure non-negative cable tensions during Traj. 1 motion, PIC control scheme was then applied. The changes in cable lengths (reference vs measured) and the measured tensions of *CDPM* from the trial with PIC control are shown in Figure 6-12.

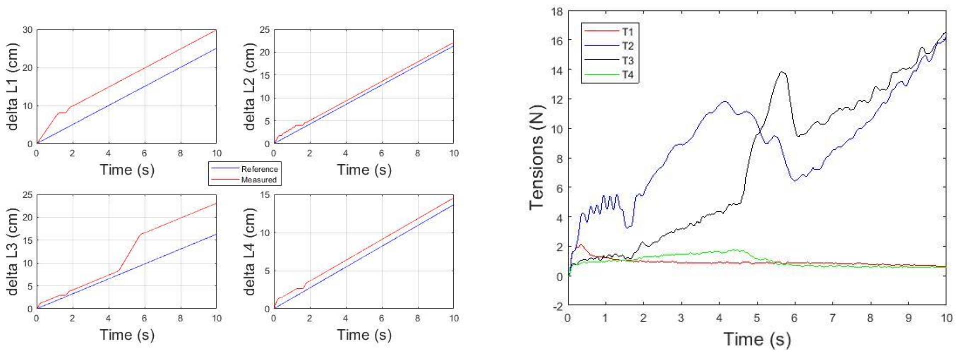

Figure 6-12. PIC control of Traj. 1. (a) The changes in cable lengths of *CDPM* (reference vs measured). (b) The cable tensions.

As can be seen, all cables of *CDPM* were held in positive tension (Figure 6-12b) and measured cable lengths, shown in Figure 6-12a, were affected by the feedback from the tension load cells during PIC control of Traj. 1. As in PC control trial, the Cables 1 and 4 stayed at low tensions as they did not contribute much to achieve the desired pose for this case.

To verify the basic position control experiments, the extracted Xsens data from the motion trackers (worn by the participant) was used to plot the joint space paths of

Traj. 1 trials. The actual joint angles (shoulder abduction angles) from the two control trials (PC and PIC), measured by Xsens, are compared in Figure 6-13.

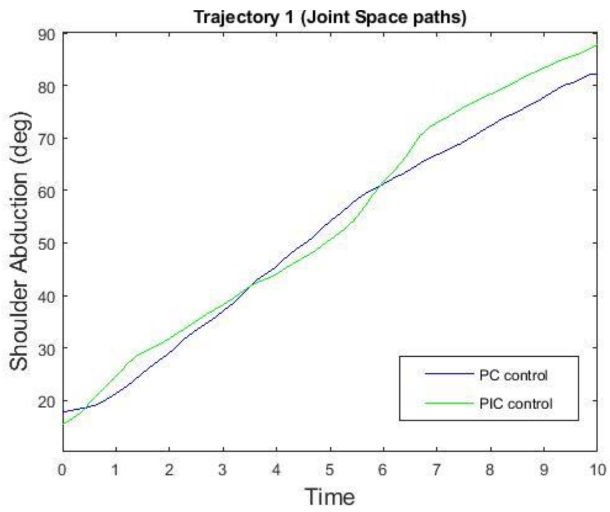

Figure 6-13. The shoulder joint angle during Traj. 1 (PC vs PIC), measured by Xsens.

As can be seen from Figure 6-13, the shoulder abduction did not start from 0 deg. which is reasonable due to the fact that the human right arm was slightly inclined from the body (16-18 deg.) at the initial position and the tracker was placed at the outer part of the arm. The final measured human shoulder abduction angles are in the range of 82-88 deg. for different controllers (PC, PIC), which are quite close to the desired 90 deg. The factors that influence the performance of HYBRID-SRE:

- The L_2 parameter (length of the participant's upper arm) is approximated.
- The coordinates of the cable connection points ($B_{1\text{-}3}$) are defined w.r.t to the center of the shoulder cuff arc which is assumed to be the center of the human shoulder joint.
- The errors associated with the Xsens trackers.
- Other issues: initial position, pretension step, noise, friction, shifts during the motions, human factors and sensor errors.

Trajectory 2 – Shoulder Horizontal Flexion:

$\boldsymbol{q_s}$=0, 0, 0, 90,0$)^T$ → $\boldsymbol{q_1}$=$(0, 0, 0, 0,0)^T$→ $\boldsymbol{q_2}$=$(0, 20, 80, 0,0)^T$→ $\boldsymbol{q_3}$=$(0, -10, -10, 0,0)^T$→ $\boldsymbol{q_4}$=$(0, 0, 0, 0,0)^T$→ $\boldsymbol{q_f}$=$(0, 0, 0, 90,0)^T$.

Trajectory 3 – Butterfly Trajectory:

$\boldsymbol{q_s}$=$(0, 0, 0, 90,0)^T$→$\boldsymbol{q_1}$=$(0, 0, 20, 30,0)^T$→$\boldsymbol{q_2}$=$(10, 10, 30, 20, 20)^T$→$\boldsymbol{q_3}$=

$(0, 20, 40, 30, 20)^T \rightarrow \boldsymbol{q_4} = (0, 10, 30, 40, 10)^T \rightarrow \boldsymbol{q_5} = (0, 0, 20, 30, 10)^T \rightarrow \boldsymbol{q_6} = (10, 0, 10, 20, 20)^T \rightarrow \boldsymbol{q_7} = (0, 0, 0, 30, 10)^T \rightarrow$
$\boldsymbol{q_8} = (0, 0, 10, 40, 10)^T \rightarrow \boldsymbol{q_9} = (0, 0, 20, 30, 0)^T \rightarrow \boldsymbol{q_f} = (0, 0, 0, 90, 0)^T$.

To control another shoulder motions with the defined trajectories, the shoulder girdle mechanism of the exoskeleton was set to active mode by controlling two rotational actuators with a simple position controller. For comparison purposes, the two basic position controllers PC and PIC were selected to control *CDPM* on the defined Traj. 2 and Traj. 3. As before, the participant was equipped with Xsens trackers during all the control trials.

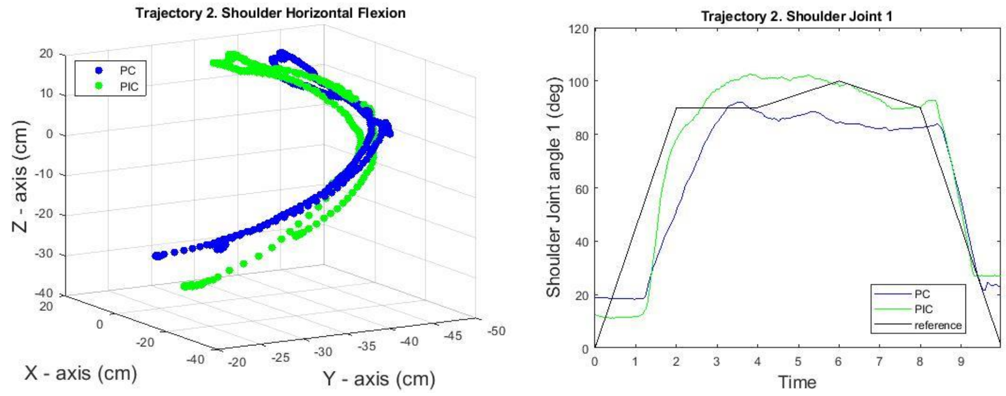

(a) (b)

Figure 6-14: PC and PIC control of Traj. 2. (a) 3D Cartesian paths (Xsens), (b) The measured shoulder angle (Xsens).

Figure 6-14(a) shows the actual 3D paths of the shoulder horizontal flexion movements (Traj. 2) obtained by the Xsens forearm tracker during PC and PIC control trials. The reference path of one of the shoulder joint angles, defined in Traj. 2, is transformed to the Xsens frame and plotted together with the measured corresponding joint angles during the two control trials (PC and PIC), as shown in Figure 6-14(b). Once more, there will always be inevitable differences in the measured results due to the same reasons discussed before, the main of which is the fact that these Xsens outputs are the human motion (not robotic) measurements. The measured cable tensions of *CDPM* during both control trials (PC and PIC) of Traj. 2 are plotted in Figure 6-15(a,b). As can be seen in Figure 6-15(b), all cables were held above the defined lower tension bound with PIC control approach.

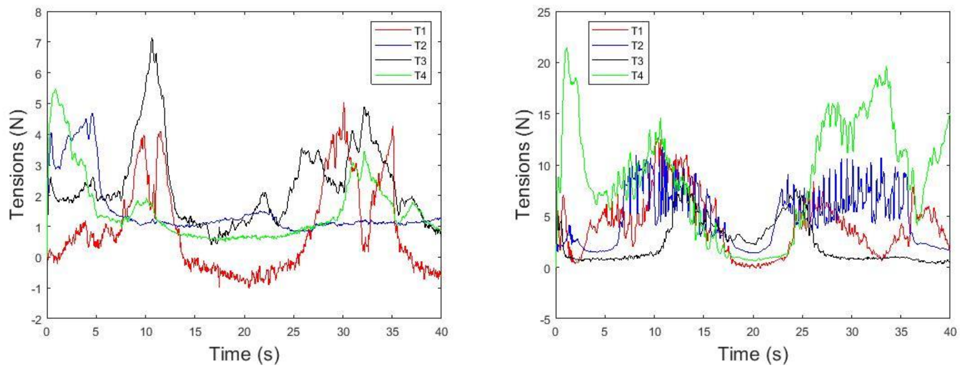

(a) (b)

Figure 6-15. The cable tensions of *CDPM* during PC (a) and PIC (b) control of Traj. 2.

Figure 6-16 shows the actual 3D Cartesian paths of Traj. 3 (butterfly-like shape), measured by Xsens, during both PC and PIC control trials. It is possible that the initial *XYZ* frames of Xsens trackers were at different orientation between the two trials which caused the orientation shift of the 3D position plots in Figure 6-16. It is worth mentioning here that all the measured Xsens data was plotted only after exporting it from Xsens to Excel and post-processing in MATLAB.

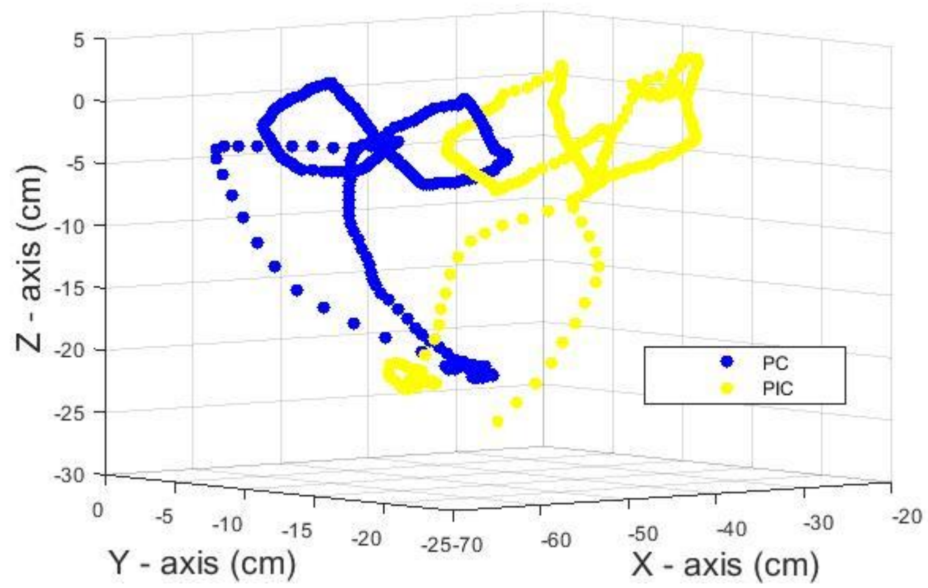

Figure 6-16: The 3D Cartesian paths of Traj. 3 (butterfly shape) during PC and PIC trials.

As can be seen in Figure 6-16, the butterfly-like shape of PC control trial is a bit smoother than the positional trace of PIC control trial that was slightly disturbed to satisfy the minimum positive tensions. The cable tensions of *CDPM* during both PC and PIC control of Traj. 3 are plotted in Figure 6-17a and Figure 6-17b, respectively. Once more, as can be seen in Figure 6-17(b), all cables were held above the defined lower tension bound with PIC control approach.

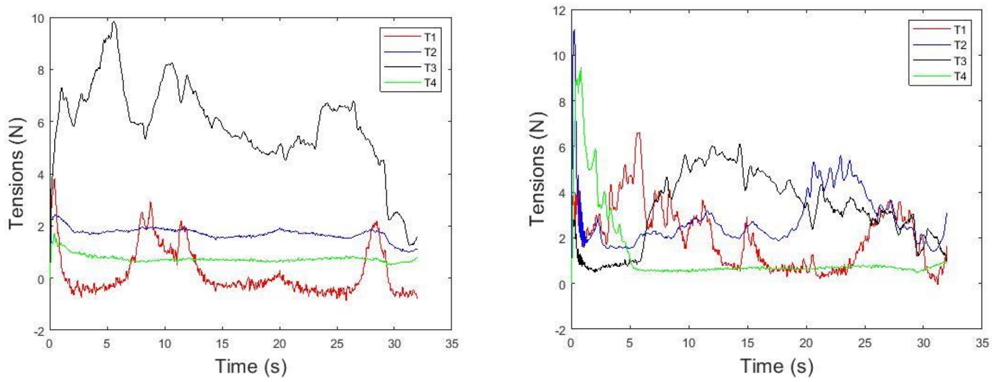

(a) (b)

Figure 6-17: The cable tensions of *CDPM* during PC (a) and PIC (b) control of Traj. 3.

6.6 Conclusion

One of the main advantageous feature of the developed HYBRID-SRE, due to the over-actuated lightweight *CDPM* (4 cables for 3-DOFs) and the actuated (or passive) *SGM*, is its ability to cover the large workspace which was experimentally evaluated (with Xsens technology) being close to the maximum reachable workspace of the healthy human shoulder. Hence, it can be claimed that the exoskeleton’s workspace is sufficient to perform the shoulder motions related to the activities of daily living (ADL) and the physical rehabilitation therapies (e.g. after stroke), which usually lie well within the tested workspace.

As the developed exoskeleton is equipped with both position and force sensors, it was experimentally controlled using the basic control strategies, depending on what kind of feedback was in use: only position feedback (PC), or both position and force feedback with the main position loop (PIC). As can be seen in Figures 6. 11(b), 6.15(a) and 6.17(a), some cable tensions are negative due to purely position control and insufficient initial pretensioning. The PIC control was used to maintain the minimum positive tensions in *CDPM* along the desired trajectory, by adjusting (pulling) the cable lengths if their tensions dropped below the defined lower tension bound. Also, to better maintain the positive tensions and improve the control performance some pretension mechanisms (e.g using springs) are desirable. Indeed, the exoskeleton can not be properly controlled if tension in the cables is not guaranteed. The basic PIC control was selected to control the complex shoulder motions for trajectory tracking purposes as the dynamics of such motions may not be well defined to implement purely force control (with tension optimization solver). The position and angle measurements from the Xsens trackers were used for verification and comparison purposes.

Apparently, parallel robots, especially the cable-driven ones are quite special regarding the control issues. In one hand, the position has to be controlled, while on the other hand the positive cable tensions have to be ensured. To overcome this problem, a modified position-based impedance controller needs to be implemented which provides tension in the inner-loop and position controller in the outer loop, and a more appropriate control structures than the implemented control approaches in this work must further be developed for a proper control of HYBRID-SRE. For example, popular choices are augmented PD [184], computed torque [185] or tension based position control [186] that may require additional sensors (e.g. IMUs). The implementation of such controllers is left for future work as it was out of scope of this thesis.

Another main advantage of HYBRID-SRE is the 2-DOFs *SGM* which can perform both actuated and passive motions to follow the coupled movements of the human shoulder girdle. It not only enlarges the shoulder workspace, as stated before, but also provides the independent assistance to the shoulder girdle DOFs avoiding the undesirable misalignments and interaction forces between the human and robot structures, which is highly important concern in robotic neurorehabilitation practices.

Chapter 7

Conclusions and Future Work

This work has presented design and development of a robotic shoulder rehabilitation exoskeleton, named HYBRID-SRE, with contributions made in biomechanics of the human shoulder and kinematics of the human-robot modelling.

To conclude, HYBRID-SRE is capable of providing the assistance to all the shoulder DOFs (independent or coupled), covering the whole workspace of the human shoulder, avoiding the human-robot joint axes misalignments, following the change of the CGH caused by the coupled shoulder motion while reducing the undesirable interaction forces and performing physiologically accurate shoulder movements without any considerable discomfort to the user. Also, the various force and position sensors in HYBRID-SRE are not only useful to implement different control algorithms but they also make the whole experimental set up a measurement tool itself. The measured forces and the ROM of the joints can be used for assessment purposes, e.g. monitoring and recording the progress of the training. In fact, the functionality of HYBRID-SRE, together with some practical improvements, makes it capable of providing most of the training modalities, mentioned in chapter 2 (Section 2.2). The future experiments with HYBRID-SRE can be improved with the additional sensors (e.g. IMU, EMG sensors) that can also be integrated into more advanced control strategies.

As the primary goal of the developed HYBRID-SRE is to assist the shoulder motions, the conducted experiments with the healthy participants were performed with their elbows being extended to exclude any undesirable disturbance caused by elbow flexion. The future work also includes the expansion of *CDPM* to accommodate the elbow motions with further extension to the wrist assistance.

The performance evaluation of HYBRID-SRE which went through the Risk Assessment approved by the University was implemented involving only healthy participants. The further experimental tests with the improved control strategies are needed prior to translating this set up to a clinical practice. Nevertheless, the authors believe that such development as HYBRID-SRE needs to be taken into consideration by the researchers for advanced design concepts that eventually will reach commercial implementation.

Other areas for future research are:

- As all people are different in size and have unique individual body characteristics, adjustable elements and simpler mounting methods are needed. New developments in soft robotics can make the future exoskeletons more flexible so that the structure of the robot will bend with the body and it will be simpler in fitting. Most of the current shoulder exoskeletons look unappealing to a general public but with the lighter “exo-suits” they could be worn underneath the cloth. To overcome the problem caused by the forces added to the body by such soft suits, the future designs should be able to change their frames from solid to soft when needed. The exoskeletons made completely of texture with inflatable parts can be utilized to exchange off material weight and structure. 3D printers using materials with variable mechanical properties can also be used to construct the devices after scanning certain parts of the individual’s upper body.
- Reducing the cost of the developed shoulder robotic exoskeletons is another important challenge that needs to be overcome by the developers. Current commercial upper limb rehabilitation robots are highly expensive (e.g. ArmeoPower cost 250k EUR [16]). Moreover, their cost does not include the maintenance and physical therapy sessions. The more the already developed commercial products enter the market, conduct clinical studies and increase their sales, the lower will be their final cost. Perhaps, focusing only on a shoulder complex with the optimized robotic exoskeleton design can bring the cost of the new devices down. Small compact air compressors with replaceable cartridges within the inflatable exoskeletons can also drastically reduce the cost of these upper limb robots. Better networking between research laboratories and businesspeople, connections to medical and insurance companies, proper regulations and social security are needed to increase the cost-effectiveness of such robotic assistive devices. Finally, rehabilitation robots are not meant to replace the human job but rather to be an effective subset of this job. As the cost of personnel will be rising while the cost of technology will go down, the shoulder robotic exoskeletons will continue to become safer, more reliable and practical.

- There is no single procedure for constructing a perfect standard shoulder robotic exoskeleton. The future shoulder exoskeletons should be safe, compliant, lightweight, adjustable, low-cost and easy to use with user friendly interfaces. Such robotic rehabilitation devices with embedded force and motion sensors will provide more efficient physical therapies to patients with shoulder impairments. A completely wearable, intrinsically compliant shoulder orthoses will be another desirable feature. New control algorithms, advanced electronics, software and machine learning tools will constitute the core of the future research platforms. Research findings in the fields of lower limb rehabilitation, biomechanical modeling, neurophysiology, control systems, mechanism synthesis, and additive manufacturing should also be incorporated in the development of intelligent robotic exoskeletons for shoulder rehabilitation.

To sum up, the further research in robotic shoulder exoskeletons should consider:

• optimum mechanism design for shoulder girdle's main DOFs

• matching the robot's workspace to the entire workspace of the human shoulder taking into account translations of GH joint

• developing an accurate musculoskeletal, kinematic and dynamic models of the human shoulder taking into account all DOFs and ROM of the shoulder complex

• acquiring more experimental/clinical data on the human physiological reaction to mechanical shoulder exoskeleton use

• modelling compliant actuation, designing soft adjustable structures, actuator-brake coupling for gravity compensations, etc.

• employing latest advances in energy harvesting systems: high pressure compressors, fuel cells, flexible batteries, etc.

• developing new faster control algorithms with real time force-feedback controllers in actuation and AAN training strategies.

• collaboration and networking with the researchers from related different fields of study, physiotherapists and industry partners.

References

[1] Stroke.org, “American Stroke Association. About Stroke,” 2020. [Online]. Available: https://www.stroke.org/en/about-stroke. [Accessed: 07-12-2020].

[2] Strokefoundation.com.au, “National Stroke Foundation of Australia. Facts and figures,” 2017. [Online]. Available: https://strokefoundation.org.au/About-Stroke/Learn/facts-and-figures. [Accessed: 07-12-2020].

[3] Strokefoundation.com.au, “The Deloitte Access Economics Report. The economic impact of stroke in Australia,” 2020. [Online]. Available: https://strokefoundation.org.au/What-we-do/For-health-professionals-and-researchers/Research/Research-resources/Economic-impact-of-stroke-in-Australia. [Accessed: 07-12-2020].

[4] E. S. Lawrence, C. Coshall, R. Dundas, J. Stewart, A. G. Rudd, R. Howard and C. D. Wolfe, "Estimates of the prevalence of acute stroke impairments," *Stroke*, vol. 32 (6), pp. 1279-1284, 2001.

[5] T. J. Quinn, S. Paolucci, K. S. Sunnerhagen, J. Sivenius, M. F. Walker, D. Toni and K. R. Lees, “Evidence-based stroke r-ehabilitation: an expanded guidance document from the european stroke organisation (ESO) guidelines for management of ischaemic stroke and transient ischaemic attack 2008,” *J Rehabil Med*, vol 41(2), pp. 99–111, 2009.

[6] P. Langhorne, J. Bernhardt, and G. Kwakkel, "Stroke rehabilitation," *The Lancet*, vol. 377 (9778), pp. 1693-1702, 2011.

[7] S. E. Fasoli, H. I. Krebs, J. Stein, W. R. Frontera, and N. Hogan, "Effects of robotic therapy on motor impairment and recovery in chronic stroke," *Arch Phys Med Rehabil*, vol. 84 (4), pp. 477-482, 2003.

[8] R. Riener, T. Nef, and G. Colombo, "Robot-aided neurorehabilitation of the upper extremities," *Med Biol Eng Comput*, vol. 43 (1), pp. 2-10, 2005.

[9] R. Colombo, I. Sterpi, A. Mazzone, C. Delconte, and F. Pisano, "Improving proprioceptive deficits after stroke through robot-assisted training of the upper limb: a pilot case report study," *Neurocase*, vol. 22, pp. 191-200, 2016.

[10] N. Norouzi-Gheidari, P. S. Archambault, and J. Fung, "Effects of robot-assisted therapy on stroke rehabilitation in upper limbs: Systematic review and meta-analysis of the literature," *J Rehabil Res Development*, vol. 49 (4), pp. 479-496, 2012.

[11] R. A. R. C. Gopura, D. S. V. Bandara, K. Kiguchi, and G. K. I. Mann, "Developments in hardware systems of active upper-limb exoskeleton robots: A review," *Robotics and Autonomous Systems*, vol. 75, pp. 203-220, 2016.

[12] R. C. V. Loureiro, W. S. Harwin, K. Nagai, and M. Johnson, "Advances in upper limb stroke rehabilitation a technology push," *Med Biol Eng Comput*, vol. 49, pp. 1103-1118, 2011.

[13] P. Maciejasz, J. Eschweiler, K. Gerlach-Hahn, A. J. Troy, and S. Leonhardt, "A survey on robotic devices for upper limb rehabilitation," *J Neuroeng Rehabil*, vol 11 (3), pp.1-29, 2014.

[14] N. Jarrasse, T. Proietti, V. Crocher, J. Robertson, A. Sahbani, G. Morel and A. Roby-Brami, "Robotic exoskeletons: a perspective for the rehabilitation of arm coordination in stroke patients," *Front Hum Neurosci*, vol. 8, p. 947, 2014.

[15] H. S. Lo and S. Q. Xie, "Exoskeleton robots for upper-limb rehabilitation: state of the art and future prospects," *Med Eng Phys,* vol. 34 (3), pp. 261-268, 2012.
[16] G. Turchetti, N. Vitiello, L. Trieste, S. Romiti, E. Geisler, and S. Micera, "Why effectiveness of robot-mediated neurorehabilitation does not necessarily influence its adoption," *IEEE Reviews in Biomed Eng,* vol. 7, pp. 143-153, 2014.
[17] M. Babaiasl, S. H. Mahdioun, P. Jaryani, and M. Yazdani, "A review of technological and clinical aspects of robot-aided rehabilitation of upper-extremity after stroke," *Disabil Rehabil Assist Technol*, vol. 11 (4), pp. 263-280, 2016.
[18] A. S. Niyetkaliyev, S. Hussain, M. H. Ghayesh, and G. Alici, "Review on Design and Control Aspects of Robotic Shoulder Rehabilitation Orthoses," *IEEE Transactions on Human-Machine Systems*, vol. 47(6), pp.1134-1145, 2017.
[19] A. S. Niyetkaliyev, S. Hussain, P. K. Jamwal, and G. Alici, "Modelling of the human shoulder girdle as a 6-4 parallel mechanism with a moving scapulothoracic joint," *Mechanism and Machine Theory,* vol. 118, pp. 219-230, 2017.
[20] A. S. Niyetkaliyev, E. Sariyildiz, and G. Alici, "Kinematic Modeling and Analysis of a Novel Bio-Inspired and Cable-Driven Hybrid Shoulder Mechanism," *ASME Journal of Mechanisms and Robotics*, vol 13 (1), 011008, pp. 1-12, 2020.
[21] A. S. Niyetkaliyev, E. Sariyildiz, and G. Alici, "A Hybrid Multi-Joint Robotic Shoulder Exoskeleton for Stroke Rehabilitation," *The IEEE/ASME Int. Conf. on AIM*, Auckland, New Zealand, pp. 857–862, 2018.
[22] O**.** Peter, G. Fazekas, K. Zsiga and Z. Denes. "Robot mediated upper limb physiotherapy: review and recommendations for future clinical trials," *Int J Rehabil Res*, vol. 34(3), pp. 196–202, 2011.
[23] C. Vaida, G. Carbone, K. Major, Z. Major, N. Plitea, and D. Pisla, "On human robot interaction modalities in the upper limb rehabilitation after stroke," *Appl. Math. Mech., Eng*, vol. 60 (1), pp. 1-12. 2017.
[24] A. Basteris, S. M. Nijenhuis, A. H. Stienen, J. H. Buurke, G. B. Prange and F. Amirabdollahian, "Training modalities in robot-mediated upper limb rehabilitation in stroke: a framework for classification based on a systematic review," *J Neuro Engineering Rehabil*, vol 11 (111), pp. 1-15, 2014.
[25] D. Koo, P. H. Chang, M. K. Sohn, and J. Shin, "Shoulder mechanism design of an exoskeleton robot for stroke patient rehabilitation," *2001 IEEE Int. Conf. Rehabil. Robot.*, Zurich, Switzerland, pp. 1-6, 2011.
[26] N. Klopcar and J. Lenarcic, "Bilateral and unilateral shoulder girdle kinematics during humeral elevation," *Clin Biomech* (Bristol, Avon), vol. 21 (1), pp. S20-S26, 2006.
[27] F. C. Forte, M. P. de Castro, J. M. de Toledo, D. C. Ribeiro, and J. F. Loss, "Scapular kinematics and scapulohumeral rhythm during resisted shoulder abduction--implications for clinical practice," *Phys Ther Sport*, vol. 10 (3), pp. 105-111, 2009.
[28] P. M. Ludewig, V. Phadke, J. P. Braman, D. R. Hassett, C. J. Cieminski, and R. F. LaPrade, "Motion of the shoulder complex during multiplanar humeral elevation," *J Bone Joint Surg Am*, vol.

91 (2), pp. 378-389, 2009.

[29] T. Nef and R. Riener, "ARMin – design of a novel arm rehabilitation robot," *IEEE 9th Int. Conf. Rehabil. Robot. ICORR 2005*, Chicago, IL, USA, pp. 57-60, 2005.

[30] M. Mihelj, T. Nef, and R. Riener, "ARMin II – 7 DoF rehabilitation robot mechanics and kinematics," *IEEE Int. Conf. Robotics and Automation*, Roma, Italy, pp. 4120-4125, 2007.

[31] T. Nef, M. Guidali, and R. Riener, "ARMin III – arm therapy exoskeleton with an ergonomic shoulder actuation," *Applied Bionics and Biomechanics*, vol. 6, pp. 127-142, 2009.

[32] T. Nef and R. Riener, "Shoulder Actuation Mechanisms for Arm Rehabiliation Exoskeletons," *2nd Biennial IEEE/RAS-EMBS Int. Conf. Biomed. Robot. Biomechatronics*, Scottsdale, AZ, USA, pp. 862-868, 2008.

[33] C. Carignan, M. Liszka, and S. Roderick, "Design of an arm exoskeleton with scapula motion for shoulder rehabilitation," *12th Int. Conf. Advanced Robotics*, Seattle, WA, USA, pp. 524-531, 2005.

[34] C. Carignan, J. Tang, and S. Roderick, "Development of an exoskeleton haptic interface for virtual task training," *Int. Conf. Intelligent Robots and Systems*, St. Louis, USA, pp. 3697-3702, 2009.

[35] J. C. Perry, J. Rosen, and B. S., "Upper-Limb Powered Exoskeleton Design," *IEEE/ASME Trans Mechatronics*, vol. 12 (4), pp. 408-417, 2007.

[36] L. K. Miller and J. Rosen, "Comparison of multi-sensor admittance control in joint space and task space for a seven degree of freedom upper limb exoskeleton," *3rd IEEE RAS & EMBS Int. Conf. Biomed. Robot. Biomechatronics*, Tokyo, Japan, pp. 70-75, 2010.

[37] Y. Mao and S. K. Agrawal, "Design of a Cable-Driven Arm Exoskeleton (CAREX) for Neural Rehabilitation," *IEEE Trans Robotics*, vol. 28 (4), pp. 922-931, 2012.

[38] G. Yang, H. L. Ho, and W. Chen, "A Haptic Device Wearable on a Human Arm," *IEEE Conf. Robot. Autom. Mechatronics*, Singapore, vol 1, pp. 243-247, 2004.

[39] Y. Mao, D. G.G., S. J.P., and S. K. Agrawal, "Human Movement Training With a Cable Driven ARm EXoskeleton (CAREX)," *IEEE Trans Neural Syst Rehabil Eng*, vol. 23 (1), pp. 84-92, 2015.

[40] Y. Mao and S. K. Agrawal, "A Cable Driven Upper Arm Exoskeleton for Upper Extremity Rehabilitation," *IEEE Int. Conf. Robotics and Automation*, Shanghai, China, pp. 4163-4168, 2011.

[41] H. S. Park, Y. Ren, and L. Zhang, "IntelliArm an exoskeleton for diagnosis and treatment of patients with neurological impairments," *2nd Biennial Int. Conf. Biomed. Robot. Biomechatronics*, Scottsdale, AZ, USA, pp. 109-114, 2008.

[42] Y. Ren, S. H. Kang, H. S. Park, Y. N. Wu, and L. Q. Zhang, "Developing a Multi-Joint Upper Limb Exoskeleton Robot for Diagnosis, Therapy, and Outcome Evaluation in Neurorehabilitation," *IEEE Trans Neural Syst Rehabil Eng*, vol. 21 (3), pp. 490-499, 2013.

[43] J.-H. Park, K.-S. Lee, H. Lee, and H. S. Park, "Development of a passive shoulder joint tracking device for upper limb rehabilitation robots," *IEEE Int. Conf. Rehabil. Robot. (ICORR)*, Singapore, pp. 713-716, 2015.

[44] S. H. Chen, W. M. Lien, W. W. Wang, G. D. Lee, L. C. Hsu, K. W. Lee, S. Y. Lin, C. H. Lin, L. Fu, J. Lai, J. Luh and W. Chen, "Assistive Control System for Upper Limb Rehabilitation Robot,"

IEEE Trans Neural Syst Rehabil Eng, vol 24, pp. 1199-1209, 2016.
[45] H. Yan, C. Yang, Y. Zhang, and Y. Wang, "Design and Validation of a Compatible 3-Degrees of Freedom Shoulder Exoskeleton With an Adaptive Center of Rotation," *J Mech Design*, vol. 136 (7), 071006, pp. 1-9, 2014.
[46] S. J. Ball, I. E. Brown, and S. H. Scott, "MEDARM: a rehabilitation robot with 5DOF at the shoulder complex," *IEEE/ASME Int. Conf. AIM*, Zurich, Switzerland, pp. 1-6, 2007.
[47] M. A. Ergin and V. Patoglu, "ASSISTON-SE: A Self-Aligning Shoulder-Elbow Exoskeleton," *IEEE Int. Conf. Robotics and Automation*, St. Paul, Minnesota, USA, pp. 2479-2485, 2012.
[48] J. Hunt, H. Lee, and P. Artemiadis, "A Novel Shoulder Exoskeleton Robot Using Parallel Actuation and a Passive Slip Interface," *J. Mechanisms Robotics*, vol. 9 (1), 011002, pp. 1-7, 2016.
[49] A. Frisoli, F. Rocchi, S. Marcheschi, A. Dettory, F. Salsedo, and M. Bergamasco, "A new force-feedback arm exoskeleton for haptic interaction in Virtual Environments," *1st Joint Eurohaptics Conf. and Symp. Haptic Interf. Virt. Envir. Teleop. Sys*., Pisa, Italy, pp. 195-201, 2005.
[50] R. A. R. C. Gopura, K. Kiguchi, and Y. Li, "SUEFUL-7: A 7dof upper-limb exoskeleton robot with muscle-model-oriented emg-based control," *IEEE/RSJ Int. Conf. Intelligent Robots and Systems*, *St. Louis*, USA, pp. 1126-1131, 2009.
[51] E. Pirondini, M. Coscia, S. Marcheschi, G. Roas, F. Salsedo, A. Frisoli, et al., "Evaluation of the effects of the Arm Light Exoskeleton on movement execution and muscle activities: a pilot study on healthy subjects," *J Neuroeng Rehabil*, vol. 13 (1), pp. 1-21, 2016.
[52] S. H. Scott, "Apparatus for measuring and perturbing shoulder and elbow joint positions and torques during reaching," *J Neuroscience Methods*, vol. 89 (2), pp. 119-127, 1999.
[53] M. H. Rahman, T. Kittel-Ouimet, M. Saad, J. P. Kenne, and P. S. Archambault, "Development and control of a robotic exoskeleton for shoulder, elbow and forearm movement assistance," *Applied Bionics and Biomechanics*, vol. 9, pp. 275-292, 2012.
[54] L. Colizzi, A. Lidonnici, and L. Pignolo, "The ARAMIS project: a concept robot and technical design," *J Rehabil Med*, vol. 41 (12), pp. 1011-1015, 2009.
[55] A. Mayr, M. Kofler, and L. Saltuari, "ARMOR: an electromechanical robot for upper limb training following stroke. A prospective randomised controlled pilot study," *Handchir Mikrochir plast Chir*, vol. 40 (1), pp. 66-73, 2008.
[56] F. Martinez, A. Pujana-Arrese, I. Retolaza, I. Sacristan, J. Basurko, and J. Landaluze, "IKO: a five actuated DoF upper limb exoskeleton oriented to workplace assistance," *Applied Bionics and Biomechanics*, vol. 6, pp. 143-155, 2009.
[57] K. Kiguchi, M. H. Rahman, M. Sasaki, and K. Teramoto, "Development of a 3DOF mobile exoskeleton robot for human upper-limb motion assist," *Robotics and Autonomous Systems*, vol. 56 (8), pp. 678-691, 2008.
[58] Z. Li, Z. Huang, W. He, and C.-Y. Su, "Adaptive Impedance Control for an Upper Limb Robotic Exoskeleton Using Biological Signals," *IEEE Trans Ind Electron*, vol 64 (2), pp. 1664-1674, 2016.
[59] P. Letier, M. Avraam, S. Veillerette, M. Horodinca, M. Bartolomei, A. Schiele and A. Preumont, "SAM a 7-dof portable arm exoskeleton with local joint control," *IEEE/RSJ Int. Conf.*

Intelligent Robotics and Systems, Nice, France, pp. 3501-3506, 2008.
[60] J.-Y. Kim, U.-J. Yang, and K. Park, "Design, motion planning and control of frozen shoulder rehabilitation robot," *Int J Prec Eng Manuf*, vol. 15, pp. 1875-1881, 2014.
[61] P. Garrec, J. P. Friconneau, Y. Measson, and Y. Perrot, "ABLE, an innovative transparent exoskeleton for the upper-limb," *IEEE/RSJ Int. Conf. Intelligent Robots and Systems*, Nice, France, pp. 1483-1488, 2008.
[62] G. R. Johnson, D. A. Carus, G. Parrini, S. S. Marchese, and R. Valeggi, "The design of a 5DOF powered orthosis for the upper limb," *Institution of Mechanical Engineers*, vol. 215 (3), pp. 275-284, 2001.
[63] T. G. Sugar, J. He, E. Koeneman, J. B. Koeneman, R. Herman, H. Huang, R.S. Schultz, D. Herring, J. Wanberg, S. Balasubramanian, P. Swenson and J. Ward, "Design and Control of RUPERT: A Device for Robotic Upper Extremity Repetitive Therapy," *IEEE Trans Neural Syst Rehabil Eng*, vol. 15, pp. 336-346, 2007.
[64] J. Huang, X. Tu, and J. He, "Design and evaluation of the rupert wearable upper extremity exoskeleton robot for clinical and in-home therapies," *IEEE Trans Syst Man Cybern*, vol 46 (7), pp. 926-935, 2015.
[65] S. Balasubramanian, R. Wei, M. Perez, B. Shepard, E. Koeneman, J. Koeneman and J. He, "RUPERT: An Exoskeleton Robot for Assisting Rehabilitation of Arm Functions," *2008 Virtual Rehabilitation*, Vancouver, BC, pp. 163-167, 2008.
[66] R. Morales, F. J. Badesa, N. Garcia-Aracil, J. M. Sabater, and C. Perez-Vidal, "Pneumatic robotic systems for upper limb rehabilitation," *Med Biol Eng Comput*, vol. 49 (10), pp. 1145-1156, 2011.
[67] R. J. Sanchez, E. T. Wolbrecht, R. Smith, J. Liu, S. Rao, S. C. Cramer, T. Rahman, J. E. Bobrow and D. J. Reinkensmeyer, "A pneumatic robot for re-training arm movement after stroke rationale and mechanical design," *IEEE 9th Int. Conf. Rehabil. Robot.*, Chicago, IL, USA, pp. 500-504, 2005.
[68] R. J. Sanchez, J. Liu, S. Rao, P. Shah, R. Smith, T. Rahman, S. C. Cramer, J. E. Bobrow and D. J. Reinkensmeyer, "Automating Arm Movement Training Following Severe Stroke Functional Exercises With Quantitative Feedback in a Gravity-Reduced Environment," *IEEE Trans Neural Syst Rehabil Eng*, vol. 14 (3), pp. 378-389, 2006.
[69] E. T. Wolbrecht, V. Chan, D. J. Reinkensmeyer, and J. E. Bobrow, "Optimizing compliant, model-based robotic assistance to promote neurorehabilitation," *IEEE Trans Neural Syst Rehabil Eng*, vol. 16 (3), pp. 286-297, 2008.
[70] J. Klein, S. Spencer, J. Allington, J. E. Bobrow, and D. J. Reinkensmeyer, "Optimization of a parallel shoulder mechanism to achieve a high-force, low-mass, robotic-arm exoskeleton," *IEEE Trans Robotics*, vol. 26 (4), pp. 710-715, 2010.
[71] S. Ikemoto, Y. Kimoto, and K. Hosoda, "Shoulder complex linkage mechanism for humanlike musculoskeletal robot arms," *Bioinspir Biomim*, vol. 10 (6), 066009, pp. 1-13, 2015.
[72] N. G. Tsagarakis and D. G. Caldwell, "Development and Control of a 'Soft-Actuated' Exoskeleton for Use in Physiotherapy and Training," *Autonomous Robots*, vol. 15, pp. 21-33, 2003.
[73] H. Kobayashi and K. Hiramatsu, "Development of Muscle Suit for Upper Limb," *IEEE Int.*

Conf. Robotics and Automation, New Orleans, LA, USA, pp. 2480-2485, 2004.

[74] J. Zhang, H. Fu, Y. Dong, Y. Zhang, C. Yang and Y. Chen, "Novel 6-Dof wearable exoskeleton arm with pneumatic force-feedback for bilateral teleoperation," *Chinese J Mech Eng (English Edition)*, vol. 21 (3), 58, pp. 1-10, 2008.

[75] Y. S. Kim, J. Lee, S. Lee, and M. Kim, "A force reflected exoskeleton-type masterarm for human-robot interaction," *IEEE Trans Syst Man Cybern*, vol. 35 (2), pp. 198-212, 2005.

[76] Y. Jeong, Y. Lee, K. Kim, Y.-S. Hong, and J.-O. Park, "A 7 DOF Wearable Robotic Arm Using Pneumatic Actuators," *32nd Int. Symp. Robotics*, Seoul, Korea, pp. 388-393, 2001.

[77] T. Noda and J. Morimoto, "Development of Upper-extremity Exoskeleton driven by Pneumatic Cylinder toward Robotic Rehabilitation Platform for Shoulder Elevation," *IEEE Int. Conf. Rehabil. Robot.*, Singapore, pp. 496-501, 2015.

[78] A. Stienen, E. Hekman, H. Braak, A. M. M. Aalsma, F. C. van der Helm and H. van der Kooij, "Design of a rotational hydroelastic actuator for a powered exoskeleton for upper limb rehabilitation," *IEEE Trans Biomed Eng*, vol. 57 (3), pp. 728-735, 2010.

[79] A. H. A. Stienen, E. E. G. Hekman, G. B. Prange, M. J. A. Jannink, A. M. M. Aalsma, F. C. T. van der Helm and H. van der Kooij, "Dampace: Design of an Exoskeleton for Force-Coordination Training in Upper-Extremity Rehabilitation," *J Medical Devices*, vol. 3 (3), 031003, pp. 1-10, 2009.

[80] A. Otten, C. Voort, A. Stienen, R. Aarts, E. Asseldonk, and H. Kooij, "LIMPACT: A hydraulically powered self-aligning upper limb exoskeleton," *IEEE/ASME Trans Mechatronics*, vol. 20 (5), pp. 2285-2298, 2015.

[81] M. Mistry, P. Mohajerian, and S. Schaal, "Arm movement experiments with joint space force fields using an Exoskeleton Robot," *IEEE 9th Int. Conf. Rehabil. Robot.*, Chicago, IL, USA, pp.408-413, 2005.

[82] B. Kim and A. D. Deshpande, "Controls for the Shoulder Mechanism of an Upper-Body Exoskeleton for Promoting Scapulohumeral Rhythm," *IEEE Int. Conf. Rehabil. Robot. (ICORR)*, Singapore, pp. 538-542, 2015.

[83] I. Galiana, F. L. Hammond, R. D. Howe, and M. B. Popovic, "Wearable Soft Robotics Device for Post-Stroke Shoulder Rehabilitation: Identifying Misalignments," *IEEE/RSJ Int. Conf. Intelligent Robotics and Systems*, Vilamoura, Algarva, Portugal, pp. 317-322, 2012.

[84] K. Xu, Y. Wang, and Z. Yang, "Design and Preliminary Experimentation of a Continuum Exoskeleton for Self-Provided Bilateral Rehabilitation," *IEEE Int. Conf. Inform. Autom. (ICIA)*, Hailar, China, pp. 327-332, 2014.

[85] H.-C. Hsieh, L. Chien, and C.-C. Lan, "Mechanical Design of a Gravity-Balancing Wearable Exoskeleton for the Motion Enhancement of Human Upper Limb," *IEEE Int. Conf. Robotics and Automation (ICRA)*, Seattle, Washington, USA, pp. 4992-4997, 2015.

[86] A. Pedrocchi, S. Ferrante, E. Ambrosini, M. Gandolla, C. Casellato, T. Schauer, C. Klauer, J. Pascual, C. Vidaurre, M. Gföhler, W. Reichenfelser, J. Karner, S. Micera, A. Crema, F. Molteni, M. Rossini, G. Palumbo, E. Guanziroli, A. Jedlitschka … G. Ferrign, "MUNDUS project MUltimodal Neuroprosthesis for daily Upper limb Support," *J Neuroeng and Rehabil*, vol. 10 (66), pp. 1-20, 2013.

[87] L. Marchal-Crespo and D. J. Reinkensmeyer, "Review of control strategies for robotic movement training after neurologic injury," *J Neuroeng Rehabil*, vol. 6 (20), pp. 1-15, 2009.

[88] H. B. Kang and J. H. Wang, "Adaptive control of 5 DOF upper-limb exoskeleton robot with improved safety," *ISA Trans*, vol. 52 (6), pp. 844-52, Nov 2013.

[89] S. Oh, K. Kong, and Y. Hori, "Design and Analysis of Force-Sensor-Less Power-Assist Control," *IEEE Trans Ind Electron*, vol. 61 (2), pp. 985-993, 2014.

[90] Z. Tang, K. Zhang, S. Sun, Z. Gao, L. Zhang, and Z. Yang, "An upper-limb power-assist exoskeleton using proportional myoelectric control," *Sensors (Basel, Switzerland)*, vol. 14 (4), pp. 6677-6694, 2014.

[91] K. Anam and A. A. Al-Jumaily, "Active exoskeleton control systems: State of the art," *Procedia Engineering*, vol. 41, pp. 988-994, 2012.

[92] A. U. Pehlivan, "Design and Control of an Exoskeletal Rehabilitation Device for Stroke and Spinal Cord Injury Patients," M. S. Thesis, Rice University, 2012.

[93] W. Yu, J. Rosen, and X. Li, "PID Admittance Control for an Upper Limb Exoskeleton," *2011 American Control Conference*, San Francisco, CA, USA, pp. 1124-1129, 2011.

[94] T. Kashima and K. Hori, "Control of biomimetic robots based on analysis of human arm trajectories in 3D movements," *Artificial Life and Robotics*, vol. 21, pp. 24-30, 2015.

[95] M. Babaiasl, A. Ghanbari, and S. Noorani, "Anthropomorphic mechanical design and Lyapunov-based control of a new shoulder rehabilitation system," *Eng Solid Mech*, vol. 2 (3), pp. 151-162, 2014.

[96] S. Balasubramanian and J. He, "Adaptive Control of a Wearable Exoskeleton for Upper-Extremity Neurorehabilitation," *Applied Bionics and Biomechanics*, vol. 9 (1), pp. 99-115, 2012.

[97] M. H. Rahman, C. Ochoa-Luna, and M. Saad, "EMG Based Control of a Robotic Exoskeleton for Shoulder and Elbow Motion Assist," *J Autom Control Eng*, vol 3 (4), pp. 270-276, 2015.

[98] P. Staubli, T. Nef, V. Klamroth-Marganska, and R. Riener, "Effects of intensive arm training with the rehabilitation robot ARMin II in chronic stroke patients: four single-cases," *J Neuroeng Rehabil*, vol. 6 (46), pp. 1-10, 2009.

[99] V. Klamroth-Marganska, J. Blanco, K. Campen, A. Curt, V. Dietz, T. Ettlin, M. Felder, B. Fellinghauer, M. Guidali, A. Kollmar, A. Luft, T. Nef, C. Schuster-Amft, W. Stahel and R. Riener, "Three-dimensional, task-specific robot therapy of the arm after stroke: a multicentre, parallel-group randomised trial," *The Lancet Neurology*, vol. 13 (2), pp. 159-166, 2014.

[100] R. S. Calabro, M. Russo, A. Naro, D. Milardi, T. Balletta, A. Leo, S. Filoni and P. Bramanti, "Who may benefit from armeo power treatment? A neurophysiological approach to predict neurorehabilitation outcomes," *PM R: the journal of injury, function, and rehabilitation*, vol 8 (10), pp. 971-978, 2016.

[101] M.-H. Milot, S. Spencer, V. Chan, J. Allington, J. Klein, C. Chou, J. E. Bobrow, S. C. Cramer and D. J. Reinkensmeyer, "A crossover pilot study evaluating the functional outcomes of two different types of robotic movement training in chronic stroke survivors using the arm exoskeleton BONES," *J Neuroeng Rehabil*, vol. 10 (112), pp. 1-12, 2013.

[102] A. Frisoli, C. Procopio, C. Chisari, I. Creatini, L. Bonfiglio, M. Bergamasco, B. Rossi and M.

C. Carboncini, "Positive effects of robotic exoskeleton training of upper limb reaching movements after stroke," *J Neuroeng Rehabil*, vol. 9 (36), pp. 1-16, 2012.

[103] L. Pignolo, G. Dolce, G. Basta, L. F. Lucca, S. Serra, and W. G. Sannita, "Upper limb rehabilitation after stroke: ARAMIS a "robomechatronic" innovative approach and prototype," *4th RAS/EMBS Int. Conf. Biomed. Robotics and Biomechatronics*, Roma, Italy, pp. 1410-1414, 2012.

[104] H. Zhang, H. Austin, S. Buchanan, R. Herman, J. Koeneman, and J. He, "Feasibility Studies of Robot-Assisted Stroke Rehabilitation at Clinic and Home Settings Using RUPERT," *IEEE Int. Conf. Rehabil. Robot.*, Zurich, Switzerland, pp. 1-6, 2011.

[105] D. J. Reinkensmeyer, E. T. Wolbrecht, V. Chan, C. Chou, S. C. Cramer, and J. E. Bobrow, "Comparison of 3D, assist-as-needed robotic arm/hand movement training provided with pneu-wrex to conventional table top therapy following chronic stroke," *Am J Phys Med Rehabil*, vol. 91, pp. 232-241, 2012.

[106] V. Crocher, A. Sahbani, J. Robertson, A. Roby-Brami, and G. Morel, "Constraining upper limb synergies of hemiparetic patients using a robotic exoskeleton in the perspective of nuero-rehabilitation," *IEEE Trans Neural Syst Rehabil Eng*, vol. 20, pp. 247-257, 2012.

[107] M. Simkins, H. Kim, G. Abrams, N. Byl, and J. Rosen, "Robotic unilateral and bilateral upper-limb movement training for stroke survivors afflicted by chronic hemiparesis," *IEEE Int. Conf. Rehab. Robot. (ICORR)*, Seattle, Washington, USA, pp. 1-6, 2013.

[108] Y. Jung and J. Bae, "Kinematic analysis of a 5-dof upper-limb exoskeleton with a tilted and vertically translating shoulder joint," *IEEE/ASME Trans Mechatronics*, vol. 20 (3), pp. 1428-1439, 2015.

[109] R. Vertechy, A. Frisoli, A. Dettori, M. Solazzi, and M. Bergamasco, "Development of a new exoskeleton for upper limb rehabilitation," *IEEE 11th Int. Conf. Rehabil. Robot*. *(ICORR)*, Kyoto, Japan, pp. 188-193, 2009.

[110] B. Bolsterlee, D. H. Veeger, and E. K. Chadwick, "Clinical applications of musculoskeletal modelling for the shoulder and upper limb," *Med Biol Eng Comput*, vol. 51 (9), pp. 953-963, 2013.

[111] C. Hogfors, G. Sigholm, and P. Herrerts, "Biomechanical model of the human shoulder - i. Elements," *J Biomech*, vol. 20 (2), pp. 157-166, 1987.

[112] C. Hogfors, B. Peterson, G. Sigholm, and P. Herberts, "Biomechanical model of the human shoulder joint - II. The shoulder rhythm," *J Biomech*, vol. 24 (8), pp. 699-709, 1991.

[113] A. A. Nikooyan, H. E. Veeger, E. K. Chadwick, M. Praagman, and F. C. Helm, "Development of a comprehensive musculoskeletal model of the shoulder and elbow," *Med Biol Eng Comput*, vol. 49 (12), pp. 1425-1435, 2011.

[114] F. C. Van der Helm, "Analysis Of The Kinematic And Dynamic Behavior Of The Shoulder Mechanism," *J Biomech*, vol. 27 (5), pp. 527-550, 1994.

[115] G. R. Johnson and I. W. Charlton, "A model for the prediction of the forces at the glenohumeral joint," *Proceedings of the Institution of Mechanical Engineers, Part H: Journal of Engineering in Medicine*, vol. 220 (8), pp. 801-812, 2006.

[116] K. R. S. Holzbaur, W. M. Murray, and S. L. Delp, "A Model of the Upper Extremity for Simulating Musculoskeletal Surgery and Analyzing Neuromuscular Control," *Annals of Biomedical*

Engineering, vol. 33 (6), pp. 829-840, 2005.

[117] M. Damsgaard, J. Rasmussen, S. T. Christensen, E. Surma, and M. de Zee, "Analysis of musculoskeletal systems in the AnyBody Modeling System," *Simulation Modelling Practice and Theory*, vol. 14, pp. 1100-1111, 2006.

[118] B. A. Garner and M. G. Pandy, "Musculoskeletal model of the upper limb based on the visible human male dataset," *Comput Methods Biomech Biomed Engin*, vol. 4 (2), pp. 93-126, 2001.

[119] C. R. Dickerson, D. B. Chaffin, and R. E. Hughes, "A mathematical musculoskeletal shoulder model for proactive ergonomic analysis," *Comput Methods Biomech Biomed Engin*, vol. 10 (6), pp. 389-400, 2007.

[120] J. Lenarcic and A. Umek, "Simple Model of Human Arm Reachable Workspace," *IEEE Transactions on Systems, Man, and Cybernetics*, vol. 24 (8), pp. 1239-1246, 1994.

[121] J. Yang, K. Abdel-Malek, and K. Nebel, "Reach envelope of a 9-degree-of-freedom model of the upper extremity," *Int. J. Robotics. Autom.*, vol. 20 (4), pp. 240-258, 2005.

[122] N. Klopcar, M. Tomsic, and J. Lenarcic, "A kinematic model of the shoulder complex to evaluate the arm-reachable workspace," *J Biomech*, vol. 40 (1), pp. 86-91, 2007.

[123] J. Lenarcic and M. Stanisic, "A humanoid shoulder complex and the humeral pointing kinematics," *IEEE Trans Robot Autom*, vol. 19, pp. 499-506, 2003.

[124] A. E. Engin and S. T. Tumer, "Three-dimensional kinematic modelling of the human shoulder complex - part I: physical model and determination of joint sinus cones," *J Biomech Eng*, vol. 111(2), pp.107-112, 1989.

[125] B. Tondu, "Modelling of the Shoulder Complex and Application to the Design of Upper Extremities for Humanoid Robots," 5th IEEE-RAS Int. Conf. on Human Robots, Tsukuba, Japan, pp. 313-320, 2005.

[126] E. Berthonnaud, G. Herzberg, K. D. Zhao, K. N. An, and J. Dimnet, "Three-dimensional in vivo displacements of the shoulder complex from biplanar radiography," *Surg Radiol Anat*, vol. 27, pp. 214-222, 2005.

[127] J. Lenarcic, M. Stanisic, and V. Parenti-Castelli, "Kinematic design of a humanoid robotic shoulder complex," *IEEE Int. Conf. Robotics Autom. (ICRA)*, San Francisco, CA, USA, vol 1, pp. 27-32, 2000.

[128] D. Ingram, C. Engelhardt, A. Farron, A. Terrier, and P. Müllhaupt, "Modelling of the human shoulder as a parallel mechanism without constraints," *Mechanism and Machine Theory*, vol. 100, pp. 120-137, 2016.

[129] W. Maurel and D. Thalmann, "Human shoulder modeling including scapulo-thoracic constraint and joint sinus cones," *Computers & Graphics*, vol. 24, pp. 203-218, 2000.

[130] Y. Kitano and K. Yokota, "Method for Measuring Position and Posture of the Shoulder Skeleton Using Parallel Links," *Trans. of the Japan Society of Mechanical Engineers*, Series C 79 (802), pp. 2004-2012, 2013.

[131] A. El Habachi, S. Duprey, L. Cheze, and R. Dumas, "A parallel mechanism of the shoulder—application to multi-body optimisation," *Multibody System Dynamics*, vol. 33, pp. 439-451, 2014.

[132] C. Charbonnier, S. Chague, F. C. Kolo, J. C. Chow, and A. Ladermann, "A patient-specific

measurement technique to model shoulder joint kinematics," *Orthop Traumatol Surg Res*, vol. 100, pp. 715-9, 2014.
[133] W. Maurel, "3D modeling of the human upper limb including the biomechanics of joints, muscles and soft tissues," Ph.D. Thesis, Laboratoire d'Infographie—Ecole Polytechnique Federale de Lausanne, 1999.
[134] B. A. Garner and M. G. Pandy, "A Kinematic Model of the Upper Limb Based on the Visible Human Project (VHP) Image Dataset," *Comput Methods Biomech Biomed Engin*, vol. 2 (2), pp. 107-124, 1999.
[135] S. Sah and X. Wang, "Determination of geometric constraints between the ribcage and scapula in the shoulder complex: a cadaver study," *Comput Methods Biomech Biomed Engin*, vol. 12, pp. 223-224, 2009.
[136] D. Blana, J. G. Hincapie, E. K. Chadwick, and R. F. Kirsch, "A musculoskeletal model of the upper extremity for use in the development of neuroprosthetic systems," *J Biomech*, vol. 41 (8), pp. 1714-21, 2008.
[137] A. Seth, R. Matias, A. P. Veloso, and S. L. Delp, "A Biomechanical Model of the Scapulothoracic Joint to Accurately Capture Scapular Kinematics during Shoulder Movements," *PloS one*, vol. 11 (1), e0141028, pp. 1-18, 2016.
[138] A. Naaim, F. Moissenet, S. Duprey, M. Begon, and L. Cheze, "Effect of various upper limb multibody models on soft tissue artefact correction: A case study," *J Biomech*, vol 62, pp. 102-109, 2017.
[139] J. H. de Groot and R. Brand, "A Three-Dimensional regression model of the scapulo-humeral rhythm," *Clinical biomechanics (Bristol, Avon)*, vol 16 (9), pp. 735-743, 2001.
[140] X. Xu, J. H. Lin, and R. W. McGorry, "A regression-based 3-D shoulder rhythm," *J Biomech*, vol. 47 (5), pp. 1206-1210, 2014.
[141] K. R. Saul, X. Hu, C. M. Goehler, M. E. Vidt, M. Daly, A. Velisar and W. M. Murray, "Benchmarking of dynamic simulation predictions in two software platforms using an upper limb musculoskeletal model," *Comput Methods Biomech Biomed Engin*, vol. 18 (13), pp. 1445-1458, 2015.
[142] D. Karlsson and B. Peterson, "Towards a model for force predictions in the human shoulder," *J Biomech*, vol. 25 (2), pp. 189-199, 1992.
[143] V. Sholukha, B. Bonnechere, P. Salvia, F. Moiseev, M. Rooze, and S. Van Sint Jan, "Model-based approach for human kinematics reconstruction from markerless and marker-based motion analysis systems," *J Biomech*, vol. 46 (14), pp. 2363-2371, 2013.
[144] G. Wu, F. C. T. van der Helm, H. E. J. Veeger, M. Makhsous, P. Van Roy, C. Anglin, J. Nagels, A. R. Karduna, K. McQuade, X. Wang, F. W. Werner and B. Buchholz, "ISB recommendation on definitions of joint coordinate systems of various joints for the reporting of human joint motion—Part II: shoulder, elbow, wrist and hand," *J Biomech*, vol. 38 (5), pp. 981-992, 2005.
[145] S. L. Delp, F. C. Anderson, A. S. Arnold, P. Loan, A. Habib, C. T. John, E. Guendelman and D. G. Thelen, "OpenSim Open Source Software to Create and analyze dynamic simulations of

movement," *IEEE Trans Biomed Eng*, vol. 54 (11), pp. 1940-1950, 2007.

[146] F. C. van der Helm, "A finite element musculoskeletal model of the shoulder mechanism," *J Biomech*, vol. 27 (5), pp. 551-569, 1994.

[147] L.-W. Tsai, "Robot Analysis: The Mechanics of Serial and Parallel Manipulators", 1999.

[148] L. Gao and W. Wu, "Forward kinematics modeling of spatial parallel linkage mechanisms based on constraint equations and the numerical solving method," *Robotica*, vol. 35 (2), pp. 293-309, 2015.

[149] A. Niyetkaliyev and A. Shintemirov, "An Approach for Obtaining Unique Kinematic Solutions of a Spherical Parallel Manipulator," *Proc. IEEE/ASME Int. Conf. Adv. Int. Mechatronics (AIM)*, Besancon, France, pp. 1355-1360, 2014.

[150] D. Ingram, "Musculoskeletal model of the human shoulder for joint force estimation," PhD dissertation, EPFL, Switzerland, 2015.

[151] B. Bolsterlee, H. E. Veeger, and F. C. van der Helm, "Modelling clavicular and scapular kinematics: from measurement to simulation," *Med Biol Eng Comput*, vol. 52 (3), pp. 283-91, 2014.

[152] A. Cereatti, T. Bonci, M. Akbarshahi, K. Aminian, A. Barre, M. Begon, D. L. Benoit, C. Charbonnier, F. D. Maso, S. Fantozzi, C.-C. Lin, T.-W. Lu, M. G. Pandy, R. Stagni, A. J. van den Bogert and V. Camomilla, "Standardization proposal of soft tissue artefact description for data sharing in human motion measurements," *J Biomech*, vol 62, pp. 5-13, 2017.

[153] P. W. McClure, L. A. Michener, B. J. Sennett, and A. R. Karduna, "Direct 3-dimensional measurement of scapular kinematics during dynamic movements in vivo," *J Shoulder Elbow Surg*, vol. 10, pp. 269-77, 2001.

[154] A. R. Karduna, P. W. McClure, and L. Michener, "Scapular kinematics: e!ects of altering the Euler angle sequence of rotations," *J Biomech*, vol. 33 (9), pp. 1063-1068, 2000.

[155] K. F. MacLean, J. N. Chopp, T. J. Grewal, B. R. Picco, and C. R. Dickerson, "Three-dimensional comparison of static and dynamic scapular motion tracking techniques," *J Electromyogr Kinesiol*, vol. 24 (1), pp. 65-71, 2014.

[156] G. Alici and B. Shirinzadeh, "Topology Optimisation and Singularity Analysis of a 3-SPS Parallel Manipulator With a Passive Constraining Spherical Joint," *Mech. Mach. Theory*, vol 39 (2), pp. 215–235, 2004.

[157] Y. Lu, B. Hu and P. -L. Liu, "Kinematics and Dynamics Analyses of a Parallel Manipulator with Three Active Legs and One Passive Leg by a Virtual Serial Mechanism," *Multibody System Dyn.*, vol 17 (4), pp. 229–241, 2007.

[158] H. Sadjadian and H. D. Taghirad, "Kinematic and Singularity Analysis of the Hydraulic Shoulder: A 3-DOF Redundant Parallel Manipulator," *Adv. Robot.*, vol 20 (7), pp. 763–781, 2005.

[159] S. Joshi and L. -W. Tsai, "A Comparison Study of Two 3-DOF Parallel Manipulators One WIth Three and the Other With Four Supporting Legs," *IEEE Trans. Robot Autom.*, vol 19 (2), pp. 200–209, 2003.

[160] R. Silva, M. Nunes, J. Bento and V. Costa, "Modelling an Inverted Slider Crank Mechanism Considering Kinematic Analysis and Multibody Aspects," *Proceedings of the XV International Symposium on Dynamic Problems of Mechanics*, Buzios, RJ, Brazil, pp. 1-10, 2013.

[161] A. Nayak, S. Caro and P. Wenger, "Kinematic Analysis of the 3-RPS-3-SPR Series-Parallel Manipulator," *Robotica*, vol 37 (7), pp. 1240–1266, 2019.

[162] B. Hu, "Formulation of Unified Jacobian for Serial-Parallel Manipulators," *Robot. Computer Int. Manuf.*, vol 30 (5), pp. 460–467, 2014.

[163] Z.-F. Shao, X. Tang and W. Yi, "Optimal Design of a 3-DOF Cable-Driven Upper Arm Exoskeleton," *Adv. Mech. Eng*., vol 6, 157096, pp. 1–8, 2015.

[164] J. Hamill and K. M. Knutzen, "Biomechanical Basis of Human Movement", *Lippincott Williams & Wilkins*, Philadelphia, PA, pp. 139–186, 2007.

[165] J.-P. Merlet, "Jacobian, Manipulability, Condition Number and Accuracy of Parallel Robots," *ASME J. Mech. Des*., vol 128 (1), pp. 199–206, 2005.

[166] X. Diao and O. Ma, "Force-Closure Analysis of 6-DOF Cable Manipulators With Seven or More Cables," *Robotica*, vol 27 (2), pp. 209–215, 2008.

[167] C. B. Pham, S. H. Yeo, G. Yang and I. M. Chen, "Workspace Analysis of Fully Restrained Cable-Driven Manipulators," *Robot. Auton. Syst*., vol 57 (9), pp. 901–912, 2009.

[168] G. Yang, S. K. Mustafa, S. H. Yeo, W. Lin and W. B. Lim, "Kinematic Design of an Anthropomimetic 7-DOF Cable-Driven Robotic Arm," *Front. Mech. Eng. China*, vol 6, pp. 45–60, 2010.

[169] T. Rasheed, P. Long, D. Marquez-Gamez and S. Caro, "Tension Distribution Algorithm for Planar Mobile Cable-Driven Parallel Robots," *3rd Int. Conf. Cable-Driven Parallel Robots (CableCon 2017)*, Québec, Canada, pp. 268–279, 2017.

[170] T. Bruckmann, L. Mikelsons, T. Brandt, M. Hiller and D. Schramm, "Wire Robots Part II: Dynamics, Control and Application," *Parallel Manipulators, New Developments, J.-H. Ryu, ed., I-Tech Education and Publishing*, Vienna, Austria, p. 498, 2008.

[171] G. Yang, W. Lin, S. K. Mustafa, C. B. Pham and S. H. Yeo, "Kinematic Design of a 7-DOF Cable-Driven Humanoid Arm: a Solution-in-nature Approach," *IEEE/ASME Int Conf on Advanced Intelligent Mechatronics (AIM)*, Monterey, USA, pp. 444 -449, 2005.

[172] S. Fang, D. Franitza, M. Torlo, F. Bekes, and M. Hiller, "Motion control of a tendon-based parallel manipulator using optimal tension distribution," *IEEE/ASME Transactions on Mechatronics*, vol. 9 (3), pp. 561–567, 2004.

[173] P. H. Borgstrom, N. P. Borgstrom, M. J. Stealey, B. Jordan, and G. S. Sukhatme, "Design and implementation of NIMS3D, a 3-d cabled robot for actuated sensing applications," *IEEE Transactions on Robotics*, vol. 25 (2), pp. 325–339, 2009.

[174] T. Bruckmann, A. Pott, and M. Hiller, "Calculating force distributions for redundantly actuated tendon-based stewart platforms," *Advances in Robot Kinematics*, Springer Netherlands, Dordrecht, pp. 403–412, 2006.

[175] S. Behzadipour and A. Khajepour, "Design of reduced dof parallel cable-based robots," *Mechanism and Machine Theory*, vol. 39, pp. 1051–1065, 2004.

[176] M. Hassan and A. Khajepour, "Minimization of bounded cable tensions in cable-based parallel manipulators," *Proceedings of the ASME IDETC/CIE Mech. and Robotics Conference*, Las Vegas, USA, pp. 991-999, 2007.

[177] L. Mikelsons, T. Bruckmann, M. Hiller, and D. Schramm, “A real-time capable force calculation algorithm for redundant tendon-based parallel manipulators,” *IEEE International Conference on Robotics and Automation (ICRA 2008)*, pp. 3869–3874, 2008.

[178] A. Pott, “An improved force distribution algorithm for over-constrained cable-driven parallel robots,” *6th International Workshop on Computational Kinematics*, Barcelona, Spain, pp. 139–146, 2013.

[179] J. Lamaury and M. Gouttefarde, “A tension distribution method with improved computational efficiency,” Cable-Driven Parallel Robots, Mechanisms and Machine Science, vol 12, Springer, Berlin, pp. 71–85, 2013.

[180] D. Lau, ‘Modelling and Analysis of Anthropomorphic Cable-Driven Robots,” PhD dissertation, The University of Melbourne, Australia, 2014.

[181] Mathworks.com, “linprog. Solve linear programming problems,” 2020 [Online]. Available: https://www.mathworks.com/help/optim/ug/linprog.html. [Accessed: 09-12-2020].

[182] D. Lau, D. Oetomo and S. K. Halgamuge, "Generalized Modeling of Multilink Cable-Driven Manipulators With Arbitrary Routing Using the Cable-Routing Matrix," *IEEE Transactions on Robotics*, vol. 29 (5), pp. 1102-1113, 2013.

[183] Xsens.com, “Motion Capture. Discover Xsens full body motion capture solutions,” 2020 [Online]. Available: https://www.xsens.com/motion-capture. [Accessed: 09-12-2020].

[184] M. Gouttefarde, J. Lamaury, C. Reichert and T. Bruckmann, "A Versatile Tension Distribution Algorithm for n -DOF Parallel Robots Driven by n+2 Cables," *IEEE Transactions on Robotics*, vol. 31 (6), pp. 1444-1457, 2015.

[185] C. Reichert and T. Bruckmann, “Unified contact force control approach for cable-driven parallel robots using an impedance/admittance control strategy,” *Proceedings of the 14th IFToMM World Congress*, Taipei, Taiwan, pp. 645-654, 2015.

[186] J. Back, L. Lindenroth, K. Rhode and H. Liu, “Model-Free Position Control for Cardiac Ablation Catheter Steering Using Electromagnetic Position Tracking and Tension Feedback”. *Frontiers in Robotics and AI*, vol. 4 (17), pp. 1-12, 2017.

Appendices

A.1 MATLAB scripts (kinematics and dynamics)

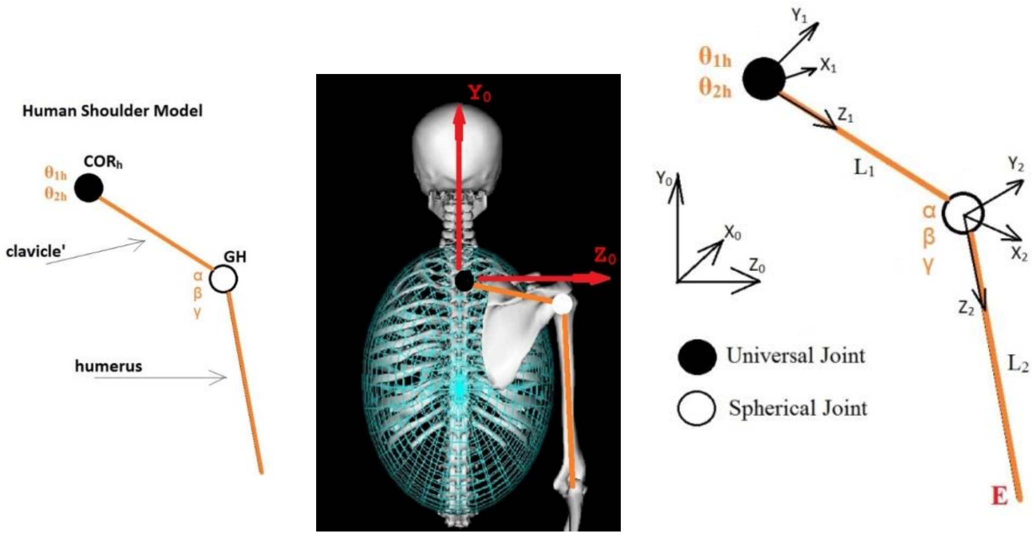

The generalised coordinates $\boldsymbol{q} = (\theta_1, \theta_2, \alpha, \beta, \gamma)^T$ (that correspond to **5-DOFs**) are defined by human **joint angles**.

```
L1 (m) - % Link 1 - Clavicle length
L2 (m) - % Link 2 - Humerus length
Rx = [1 0 0; 0 cos(θ1) -sin(θ1); 0 sin(θ1) cos(θ1)];
Ry = [cos(θ2) 0 sin(θ2); 0 1 0; -sin(θ2) 0 cos(θ2)];
R1_0 = Rx*Ry; % Rotation matrix of frame 1 w.r.t frame 0
P1_0 = 0; % frame 1 w.r.t frame 0 (universal joint)
P2_1 = [0 0 L1]'; % frame 2 (spherical joint) w.r.t frame 1
P2_0 = P1_0 + R1_0*P2_1; % frame 2 w.r.t frame 0
Ry = [cos(α) 0 sin(α); 0 1 0; -sin(α) 0 cos(α)];
Rx = [1 0 0; 0 cos(β) -sin(β); 0 sin(β) cos(β)];
Ry2 = [cos(γ) 0 sin(γ); 0 1 0; -sin(γ) 0 cos(γ)];
R2_1 = Ry*Rx*Ry2; % Rot. Matrix of frame 2 w.r.t frame 1
R2_0 = R1_0*R2_1; % Rot. Matrix of frame 2 w.r.t frame 0
E2 = [0 0 L2]'; % end-effector (E) w.r.t frame 2
E1 = P2_1 + R2_1*E2; % end-effector (E) w.r.t frame 1
E0 = P2_0 + R2_0*E2; % end-effector (E) w.r.t frame 0
% CDPM module. Shoulder cuff base points:
B11 = [-0.17; 0.19; L1+0.19];% B1 location w.r.t frame 1(m)
B21 = [-0.09; 0.21; L1];     % B2 location w.r.t frame 1(m)
B31 = [0.17; 0.14; L1];      % B3 location w.r.t frame 1(m)
u = 0.10;  % radius of the upper arm cuff (m)
U12 = [-u; 0; L2];        % U1 location w.r.t frame 2 (m)
U22 = [0; u; L2];         % U2 location w.r.t frame 2 (m)
U32 = [u;0;L2];           % U3 location w.r.t frame 2 (m)
% upper arm connection points w.r.t frame 1
U11 = P2_1 + R2_1*U12;    % U1 location w.r.t frame 1 (m)
U21 = P2_1 + R2_1*U22;    % U2 location w.r.t frame 1 (m)
U31 = P2_1 + R2_1*U32;    % U3 location w.r.t frame 1 (m)
% cable vectors (between connection points) w.r.t frame 1:
l11 = P2_1+R2_1*U12-B11;  % vector of cable 1 w.r.t frame 1
```

```
l21 = P2_1+R2_1*U22-B21;  % vector of cable 2 w.r.t frame 1
l31 = P2_1+R2_1*U22-B31;  % vector of cable 3 w.r.t frame 1
l41 = P2_1+R2_1*U32-B31;  % vector of cable 4 w.r.t frame 1
% cable (1-4) lengths -
l1 = sqrt((P2_1+R2_1*U12-B11)'*(P2_1+R2_1*U12-B11));
l2 = sqrt((P2_1+R2_1*U22-B21)'*(P2_1+R2_1*U22-B21));
l3 = sqrt((P2_1+R2_1*U22-B31)'*(P2_1+R2_1*U22-B31));
l4 = sqrt((P2_1+R2_1*U32-B31)'*(P2_1+R2_1*U32-B31));
% cross products of vectors U and cable vectors (frame 1)
U11_l11 = cross(U11,l11);
U21_l21 = cross(U21,l21);
U21_l31 = cross(U21,l31);
U31_l41 = cross(U31,l41);
% [4x4] forward Jacobian of CDPM:
Jp1 = [l1 0 0 0; 0 l2 0 0; 0 0 l3 0; 0 0 0 l4];
Jp2 = [U11_l11(1) U11_l11(2) U11_l11(3);
U21_l21(1) U21_l21(2) U21_l21(3);
U21_l31(1) U21_l31(2) U21_l31(3);
U31_l41(1) U31_l41(2) U31_l41(3)]; % [4x3] inv. J of CDPM
Jp = inv(Jp1)*Jp2;   % [4x3] geometrical Jacobian of CDPM
A = Jp.'; % [3x4] structure matrix of CDPM
Jnew = (A'*A)^(-1)*A'; % Pseudoinverse of Structure Matrix
m = 5;                  % mass of the arm (kg)
g = [0 -9.8 0]';        % gravity (Y axis is upwards)
r = 0.05;               % radius of the upper arm
Iox = 1/12*m*L2^2+1/4*m*r^2; % moment of inertia about X
Ioy = 1/12*m*L2^2+1/4*m*r^2; % moment of inertia about Y
Ioz = 1/2*m*r^2;             % moment of inertia about Z
I = [Iox 0 0; 0 Ioy 0; 0 0 Ioz]; % Inertia matrix
rog = R2_1*E2; % along the arm (to the center of mass)
rmg = m*g;     % gravity vector
S = [0 cosd(α) sind(α)*sind(β); 1 0 cosd(β); 0 -sind(α)
cosd(α)*sind(β)]; % a square matrix S
% Mass matrix:
M = S'*[Iox*cosd(β)*cosd(γ) Iox*sind(γ) 0; -
Ioy*cosd(β)*sind(γ) Ioy*cosd(γ) 0; -Ioz*sind(β) 0 Ioz];
G = cross(Rog, Rmg); % Gravity matrix
Tau = G;  % Torque due to only gravity force
T = Jnew*Tau; % Tensions due to the applied torque
% the linprog command is used to find optimal tensions
x = linprog([T(1) T(2) T(3) T(4)], % non-optimized tensions
[],
[],
[A(1,1) A(1,2) A(1,3) A(1,4);A(2,1) A(2,2) A(2,3)
A(2,4);A(3,1) A(3,2) A(3,3) A(3,4);],            %
structure matrix components
[Tau(1); Tau(2); Tau(3)],          % applied torque
[2, 2, 2, 2],                      % lower tension bounds
[20, 20, 20, 20],                  % upper tension bounds
options);
```

A. 2 Main CAD assembly of HYBRID-SRE and its hardware specifications.

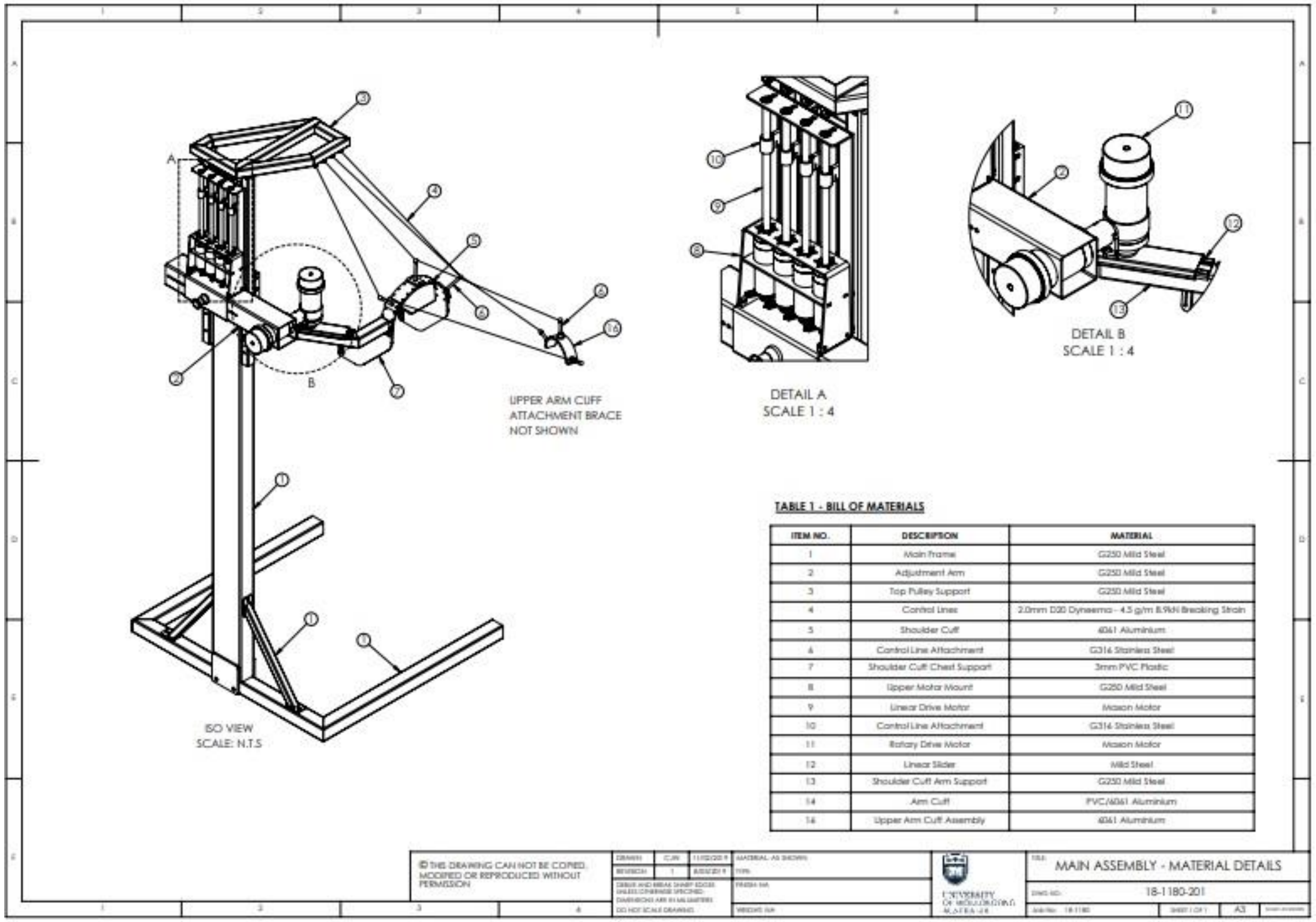

TABLE 1 - BILL OF MATERIALS

ITEM NO.	DESCRIPTION	MATERIAL
1	Main Frame	G250 Mild Steel
2	Adjustment Arm	G250 Mild Steel
3	Top Pulley Support	G250 Mild Steel
4	Control Lines	2.0mm D20 Dyneema - 4.5 g/m 8.9kN Breaking Strain
5	Shoulder Cuff	6061 Aluminium
6	Control Line Attachment	G316 Stainless Steel
7	Shoulder Cuff Chest Support	3mm PVC Plastic
8	Upper Motor Mount	G250 Mild Steel
9	Linear Drive Motor	Maxon Motor
10	Control Line Attachment	G316 Stainless Steel
11	Rotary Drive Motor	Maxon Motor
12	Linear Slider	Mild Steel
13	Shoulder Cuff Arm Support	G250 Mild Steel
14	Arm Cuff	PVC/6061 Aluminium
16	Upper Arm Cuff Assembly	6061 Aluminium

HYBRID-SRE hardware specifications.

Name	Image	Tech Spec.
EC 60 flat Ø60 mm, brushless, 100 Watt, without cover		Diameter: 60 mm Type performance: 100 W Nominal voltage: 48 V Idle speed: 3970 rpm Maximum torque: 319 mNm Weight 470g
Planetary Gearhead GP 52 C Ø52 mm, 4 - 30 Nm, Ceramic Version		Diameter: 52 mm Reduction Ratio: 126 : 1 Torque: 30 Nm Weight 770g
Encoder MILE, 1024 CPT, 2 Channels, with Line Driver		Counts per turn: 1024 channels: 2 line driver: Yes Weight 10g
EC-i 30 Ø30 mm, brushless, 30 W, with Hall sensors		Diameter: 30 mm Type performance: 30 W Nominal voltage: 12 V Idle speed: 9190 rpm Maximum torque: 37.3 mNm Weight 150g
Screw Drive GP 32 S Ø32 mm, Ball Srew, Ø10 x 2		Diameter: 32 mm Reduction 4.8:1 Max. feed velocity 56mm/s Max. feed force: 517 N Max. efficiency 75% Weight 300g
Encoder ENC 16 EASY, 1000 pulses		Counts per turn: 1000 channels: 3 line driver: RS422
ESCON 50/5, 4-Q Servocontroller for DC/EC motors, 5/15 A, 10 - 50 VDC		Max. speed (DC) 150000 rpm Hall sensor signals H1, H2, H3 Encoder signals A, A, B, B\ Digital/Analog I/O 2-2/2-2 Weight 204 g
MLS66: Miniature S-Type Force Sensor – 20 kg		Capacity: 20kg Thread Size: M8 Accuracy: 0.05%FS Output: 2.0 ± 10% mV Cable Length: 3m
FC2231-0000-0010-L. - PRESSURE SENSOR		10 – 100 lbf Ranges Supply Voltage: 5.0V, Ambient Temperature: 25°C Span (Amplified) 3.88-4.0-4.12 V Weight 18.41 grams
QPIDe – PCI Express-based Data Acquisition Board		QPIDe - Data Acquisition Board - 8 channel - PCI Express-based Data Acquisition Board - Quick-connect terminal board and cabling included - User Manual and Quick Start Guide included

A.3 Video Demos

Video links:

1) https://drive.google.com/file/d/1-d_l-rHy_NH-Qz3VBO6BgjF8C29xTdXC/view?usp=sharing

2) https://drive.google.com/file/d/1VRnv3lnjzZvS9C0TBUlVG731zy6ve4m1/view?usp=sharing